Influence of large-scale structure on momentum and scalar transfer process in spatially-developing shear mixing layer

Kotaro TAKAMURE

Department of Mechanical Science and Engineering,
Nagoya University

in partial fulfillment of the requirements
for the degree of
Doctor of Philosophy

January 2019

DEDICATION

I would like to dedicate this thesis to my father, Satoshi Takamure, my mother, Tizu Takamure, and my sister, Aki Takamure. They have continuously encouraged me to reach my dream.

Contents

Nomenclature

Symbol	Explanation
C	Instantaneous scalar concentration
c'	Instantaneous scalar concentration fluctuation
C_ϵ	Dissipation coefficient of the turbulent kinetic energy
$Cs_{-u'v'}$	Co-spectra for the Reynolds stress
$Cs_{-v'c'}$	Co-spectra for the scalar flux
f	Frequency
$F(x, Mode)$	Cumulative distribution function
F_th	Cumulative energy rate (over 60 %)
K	Local average of turbulent kinetic energy
K_1-K_6	Ratio of the mean-squared velocity derivatives
k	wavenumber ($= 2\pi f/\overline{U}$)
L	Height of the computational domain
L_b	bulk length
L_{cycle}	Length of the large-scale energy-containing structure
L_{cycle}^{max}	Maximum value of L_{cycle}
L_u	Integral length scale (streamwise integral length scale)
$\mathbf{L}(U_i)$	Discretization approximations for the viscous term
L_x, L_y, L_z	Computational domain of the streamwise, vertical, and spanwise direction
$\mathbf{N}(U_i)$	Discretization approximations for the convection term
N_x, N_y, N_z	Grid points of the streamwise, vertical, and spanwise direction
P	Instantaneous pressure
p'	Instantaneous pressure fluctuation
Pr_T	Turbulent Prandtl number
Pr_Tcs	Conditional turbulent Prandtl number
Re_λ	Turbulent Reynolds number ($= (2K/3)^{\frac{1}{2}}\lambda/\nu$)
Sc	Schmidt number ($Sc = 1$)
S_u	Power spectrum for the streamwise velocity fluctuation
S_p	Power spectrum for the pressure fluctuation
$\overline{U}$	Local mean streamwise velocity
U_0	Inlet mean streamwise velocity ($(= U_1 + U_2)/2$)
U_1, U_2	Upper and Lower inlet streamwise velocity ($U_1 = 2.0$ and $U_2 = 1.0$)

U_i	Instantaneous velocity component in the i (= x, y, and z) direction
u', v', w'	Streamwise, vertical, and spanwise velocity fluctuation
x, y, z	Streamwise, vertical, and spanwise directions
x_0	Virtial origin
y_{max}	Vertical location where the maximum of each variable exists
α_T	Turbulent scalar diffusivity coefficient
$\alpha_T cs$	Conditional turbulent scalar diffusivity coefficient
ΔU	Difference in the inlet streamwise velocity between U_1 and U_2 $(= U_1 - U_2)$
δ_U	Normalized momentum thickness
δ_{U0}	Initial momentum thickness
Δt	Time step span
η	Kolmogorov length scale $(= (\nu^3 \eta^{-1})^{1/4})$
ϵ	Dissipation rate of the turbulent kinetic energy
λ	Taylor's microscale
ν	Kinematic viscosity
ν_T	Eddy diffusivity coefficient
$\nu_T cs$	Conditional eddy diffusivity coefficient
ω_{nor}	Vorticity magnitude normalized by $\Delta U/\delta_U$
ω_T	Threshold value determined from the volume fraction of the turbulent region in the specific area
τ	time lag
$\overline{\mathcal{C}}_{u'v'}$	Convection term in the momentum transport equation
$\overline{\mathcal{C}}_{v'c'}$	Convection term in the scalar transport equation
$\overline{\mathcal{P}}_{u'v'}$	Production term in the momentum transport equation
$\overline{\mathcal{P}}_{v'c'}$	Production term in the scalar transport equation
$\overline{\epsilon}_{u'v'}$	Dissipation term in the momentum transport equation
$\overline{\epsilon}_{v'c'}$	Dissipation term in the scalar transport equation
$\overline{\mathit{\Pi}}_{u'v'}$	Pressure-strain correlation term in the momentum transport equation
$\overline{\mathit{\Pi}}_{v'c'}$	Pressure-strain correlation term in the scalar transport equation
$\overline{\mathcal{D}}_{u'v'}$	Diffusion term in the momentum transport equation $(= \overline{\mathcal{D}^{\mathcal{T}}}_{u'v'} + \overline{\mathcal{D}^{\nu}}_{u'v'} + \overline{\mathcal{D}^{\mathcal{P}}}_{u'v'})$

$\overline{\mathcal{D}}_{v'c'}$	Diffusion term in the scalar transport equation ($= \overline{\mathcal{D}^{\mathcal{T}}}_{v'c'} + \overline{\mathcal{D}^{\nu}}_{v'c'} + \overline{\mathcal{D}^{\mathcal{P}}}_{v'c'}$)
$\overline{\mathcal{D}^{\mathcal{T}}}_{u'v'}$	Turbulent diffusion term in the momentum transport equation
$\overline{\mathcal{D}^{\mathcal{T}}}_{v'c'}$	Turbulent diffusion term in the scalar transport equation
$\overline{\mathcal{D}^{\nu}}_{u'v'}$	Viscous diffusion term in the momentum transport equation
$\overline{\mathcal{D}^{\nu}}_{v'c'}$	Viscous diffusion term in the scalar transport equation
$\overline{\mathcal{D}^{\mathcal{P}}}_{u'v'}$	Pressure diffusion term in the momentum transport equation
$\overline{\mathcal{D}^{\mathcal{P}}}_{v'c'}$	Pressure diffusion term in the scalar transport equation
$\overline{\square}$	Averaged value of each statistic (e.g., $\overline{u}$ and $\overline{uv}$)
$(\square)_{max}$	Maximum value of the vertical distribution of each statistic at a certain streamwise location x (e.g., $(\overline{uv})_{max}$ and $(\overline{u^2})_{max}$)

Acronyms

CGMT	Counter gradient momentum transport
CG method	Conjugate gradient method
DNS	Direct numerical simulation
GMT	Gradient momentum transport
JPDF	Joint probability density function
LES	Large eddy simulation
MPI	Message passing interface
POD	Proper orthogonal decomposition

Chapter 1

Introduction

1.1 Background

This thesis is about a free shear layer formed by the merging of two streams with different flow velocities. These two streams repeatedly mix and diffuse complicatedly as it proceeds toward the downstream direction. Such a flow field is often called a "turbulent mixing layer." The turbulent mixing layer has been used for various research because its geometric shape is very simple.

One of the significance of these studies is to clarify the quasi-deterministic development mechanism of the large-scale structure (coherent structure) which is the main constituent element of the turbulent mixing layer [1, 2, 3, 4, 5, 6, 7, 8]. Various shear flows including the mixing layer are known to contain large-scale structures and it is known that this structure persists permanently. The discovery of the deterministic mechanism in this organizational large-scale structure is expected to greatly contribute to the elucidation of the elementary process of turbulent development. Hence, numerous studies on mixing layers have been focused on the vortex dynamics of the large-scale structure and its inner structure and their statistical properties. In the following sections of this chapter, the research background related to the large-scale structure is introduced and the open questions which are still related to this research are explained.

1.1.1 Large-scale structure in the shear mixing layer

After the discovery of a large-scale (coherent vortex) structure in the shear mixing layer (Fig. 1.1) by Brown and Roshko [9], various experimental and numerical studies have carried out in order to find the origin and universality

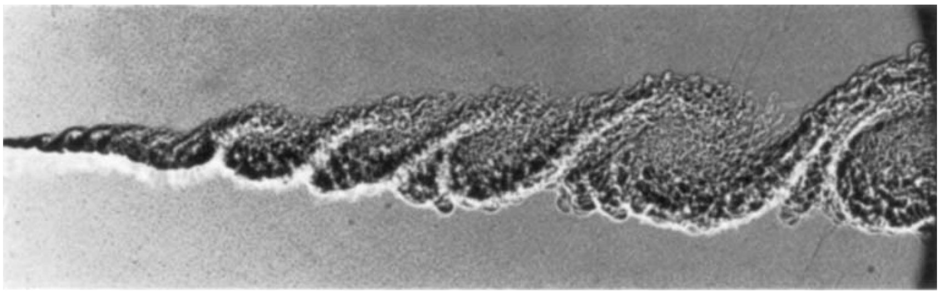

Figure 1.1: Large-scale coherent vortex structure in shear mixing layer (from Brown and Roshko [9]).

related to the large-scale structure. These many studies on the large-scale structure focused on the dynamical behavior of the vortex and have revealed their developmental mechanism by tracking and observing the large-scale vortices. For instance, numerical simulation of Corcos and Sherman [10] shows the details of the two-dimensional behavior of the mixing layer, later extended to three-dimensional behaviors [11,12]. Lasheras et al. [13] pointed out that the position of the transition to the three-dimensionalization of the mixing layer depends on the initial conditions. Furthermore, it was clarified that the generation of the spanwise vortex contributes to the entrainment process in the initial stage of mixing layer development. In the follow-up to Lasheras and Choi [14], they described the detailed process until the shear mixing layer has a three-dimensional structure. In an experimental study by using the dye films of Winlant and Browand [15], it was claimed that a continuous merger is responsible for the main process of diffusion of the mixing layer. This suggests that the turbulent transition process depends on large-scale structure.

Characteristics of turbulence statistics in the coexisting field of a large-scale structure were shown by Brown and Troutt [16]. They examined the correlation between streamwise and spanwise velocities and clarified the relation between the irregularity of the vortex structure and the vortex scale. Moser and Rogers [17] observed the development of the large-scale structure focusing on vortex pairing and made a connection with statistical properties. Researches related to Moser and Roger's point of view [17] can be found in various papers [18,19,20,21,22,23,24,25]. Ovidio and Coats [26] showed statistical evidence that the merging characteristic of large-scale vortices is changed even in the region where the average and fluctuation velocity distributions have already reached self-similar state. Same results were obtained in large eddy simulation (LES) by Mcmullan et al. [27], which means that the structure of the large-scale vortex structure is still changing even if some statistics reached self-similar state. Here, it is worth noting that the state of development of the shear mixing layer can be classified into the three regions, "developing region," "semi-developed region," and "fully-developed region," which are defined as follows:

- The developing region means the upstream region where all the statistics are non-similar states. In this region, large-scale vortex structure is induced by Kelvin-Helmholtz instability, and the development of three-dimensional structure such as longitudinal vortex structure is prominent. This region does not have much small-scale structure yet, that is, it is not turbulent.

- The semi-developed region shows an energy spectrum as seen in turbulence, which has an inertial subrange and a self-similarity. Thus, the flow in this region seems to have reached the steady state in the energy distribution but the transition of the dynamic structure is still continuing. In addition, basic statistics such as first-order statistics in this area are self-similar, but higher-order statistics such as the Reynolds shear stress, dissipation rate of the turbulent kinetic energy, and derivative skewness are non-similar.

- The fully-developed region indicates that most statistics including above reached the self-similar and steady states.

The details of the spatial characteristics in the semi- and fully-developed turbulent regions have been investigated by using numerical simulation. Roger and Moser [28] conducted a direct numerical simulation (DNS) of the time-evolving free shear mixing layer and got the turbulence characteristics in the fully-developed turbulent region. This simulation got the turbulence characteristics when the spectrum reached a steady state (i.e., semi-developed turbulent region) by using the periodic boundary condition of the streamwise direction. Later, Balaras et al. [29] got similar results to Roger and Moser by LES. However, we should note that the time-evolving field is fundamentally different from the spatial evolving field because the time evolution of vortices and the entrainment in shear mixing layer is bound by assuming uniformity of periodic boundary conditions of the streamwise direction. As a result, this fact may inhibit the development of large-scale structures and change the characteristics of this shear mixing layer. Attili and Bisetti [30] conducted a DNS with a large computational domain of the spatially developing free shear mixing layer using message passing interface (MPI) technology. This simulation succeeded in developing turbulence up to the fully-developed turbulent region. The basic turbulence characteristics obtained by Attili et al. quantitatively agreed with the results of Roger and Moser et al.

On the other hand, turbulence characteristics of small-scale vortex structure are known to be dependent on characteristics of large-scale structure, and these relationships were also investigated. Fiscaletti et al. [31] investigated the interaction between large-scale and small-scale vortices in a mixing layer. They revealed that the small-scale activity appears to be closely related to large-scale gradients, i.e., the correlation between the small-scale activity and the large-scale velocity fluctuations is shown to reflect a property of the large-scales. This result provided the evidence of the so-called "scale invariance" by Meneveau and Katz [32] that some of the large-scale characteristics are not lost at the small-scale. This fact suggests that the characteristics of the large-scale vortex induced by Kelvin-Helmholtz instability affect the characteristics of the turbulence that reached a self-similar state. In fact, it is observed in many studies that small-scale statistics also change depending on the inflow conditions when the characteristics of the large-scale structure depend on the inflow condition. Furthermore, according to recent reports [33, 34, 35, 36], it has been reported that large-scale structures cause various peculiar phenomena in momentum and scalar transfer in the well-developed turbulent mixing layer.

In the next section, we present several research examples (e.g., counter-gradient transfer of momentum and scalar transfer, characteristics of turbulent Prandtl number in large-scale structure coexisting field (dissimilarity of momentum and scalar flux), and non-equilibrium turbulence) where large-scale structures cause unique turbulence characteristics.

1.1.2 Counter-gradient momentum and scalar transfer

The counter-gradient transfer means that the momentum and scalar are transferred against the mean velocity and scalar gradient. This phenomenon is often observed in the ocean and atmosphere. This phenomenon was reported in the experiments on a liquid shear mixing layer by Huang and Ho [37] and the numerical simulation by Moser and Rogers [17]. Hussain and Zaman [38] and Hussain [39] pointed out that the counter-gradient transfer of scalar and momentum in shear flows is governed by coherent large-scale structure. Furthermore, Ito et al. [33] experimentally investigated the momentum and mass transfer from developing to well-developed region in thef shear mixing layers by modifying the initial condition using trip wires. They found that in the developing mixing layer, even though the total momentum transfer obeys the gradient momentum transfer, the counter-gradient momentum transfer takes place in specific frequency bands. As shown above, it can be seen that the counter-gradient transfer was observed under various conditions in large-scale structure coexisting field. However, their research did not refer to its details of the driving factor of the counter-gradient transfer, due to the limited measurable data.

1.1.3 Turbulent Prandtl number in large-scale structure coexisting field

Since the governing equations of velocity and scalar fields are similar in shape, it is well known that there is a strong relationship between momentum and scalar transfer [40, 41]. Focusing on the turbulent Prandlt number, Pr_T, defined by the ratio of the eddy diffusivity coefficient to the turbulent scalar diffusivity coefficient, it has been pointed out that Pr_T is smaller than 1 (approximately $Pr_T = 0.5 \sim 1.0$) in various turbulence fields [42, 43, 44]. This means that the dissimilarity exists inherently even when the global gradient of the scalar and velocity field are the same. On the other hand, there are reports that Pr_T decreases when large-scale structures coexist in the turbulent flow. This phenomenon is also thought to be due to the pressure. Actually there is a correlation between negative pressure and large-scale vortex. However, since the physical interpretation on this is not clear, the investigation is still necessary.

1.1.4 Non-equilibrium turbulence characteristics

The term "equilibrium" is usually applied to the steady state of the energy spectrum with the inertial range in the Kolmogorov theory [45]. This theory is called "universal equilibrium theory." Kolmogorov's inertial subrange is a constant flux state to which energy is inputed and lost at the same rate. That is, the word "equilibrium" can be understood to mean a "balance," even if it is applied to a balance of fluxes, not of static quantities.

Usually, the turbulence energy is transported from larger to smaller scales of motion [46, 47, 48], and if this downward cascade occurs without a time lag, $C_\epsilon = \frac{\epsilon L_u}{(2K/3)^{\frac{3}{2}}} \sim \frac{L_u/\lambda}{Re_\lambda}$ takes a constant value (ϵ is the dissipation rate of the turbulent kinetic energy for the unit mass, L_u is the integral length scale, K is the local average of turbulent kinetic energy, and Re_λ ($= (2K/3)^{\frac{1}{2}}\lambda/\nu$) is the turbulent Reynolds number based on $(2K/3)$, Taylor's microscale, λ, and the kinematic viscosity, ν).

On the other hand, turbulent flows in which C_ϵ is not constant have been found in various type flows, for example, grid turbulence, turbulent boundary layers, axisymmetric turbulent wakes, uniformly shear flow, and box turbulence with unsteady energy input and so on. Recent research has found that this phenomenon in which C_ϵ is not constant is related to the large-scale structure. Goto and Vassilicos [34] suggested that the existence of a low-frequency conspicuous peak in the power spectrum for the velocity fluctuation causes the scaling of $C_\epsilon \sim Re_\lambda^{-1}$ (i.e., C_ϵ does not take a constant value). This cause is also explained by the work of Goto and Vassilicos [34, 49, 50]; the instantaneous values of energy flux and dissipation are never equal in the case of an unsteady turbulence (with a peak on the low-wavenumber side of the spectrum). It is believed that this is caused by the cascade time-lag occurring between energy flux and dissipation. In recent years, this idea began to be supported by researches of several type grid turbulence and wake. If this interpretation is correct, it is expected that the same tendency is also seen in the shear mixing layer where the large-scale structure is dominant.

1.2 Research purpose and theme of this thesis

In this thesis, I performed a direct numerical simulation of a spatially developing shear mixing layer covering from developing to fully-developed regions. The aim of this study is to investigate the influence of large-scale structure on various phenomena and characteristics (e.g., counter-gradient momentum transport phenomenon, Pr_T, and non-equilibrium turbulence).

Chapter 1 gave the introduction and purpose. Chapter 2 describes the numerical details of the DNS. In Chapter 3, the basic flow characteristics for the velocity field are briefly given and the counter-gradient momentum transport phenomenon is discussed. Chapter 4 describes the scalar transport mechanisms and characteristics of Pr_T. Chapter 5 describes the spatial transition of the dissipation coefficient of the turbulent kinetic energy. Finally, in Chapter 6, the conclusion of this study is summarized.

Chapter 2

Numerical Method

2.1 Overview of direct numerical simulation

A conventional staggered grid arrangement is used in which the velocity components are located on cell faces and the pressure and other scalar variables are located at cell centers (See Fig. 2.1). The governing equations are the normalized continuity and Navier–Stokes equations for incompressible flows, and the scalar transport equation,

$$\frac{\partial U_i}{\partial x_i} = 0, \tag{2.1}$$

$$\frac{\partial U_i}{\partial t} + U_j \frac{\partial U_i}{\partial x_j} = -\frac{\partial P}{\partial x_i} + \frac{1}{Re}\frac{\partial^2 U_i}{\partial x_j \partial x_j}, \tag{2.2}$$

$$\frac{\partial C}{\partial t} + U_j \frac{\partial C}{\partial x_j} = \frac{1}{ReSc}\frac{\partial^2 C}{\partial x_j \partial x_j}, \tag{2.3}$$

where U_i ($i = x$, y, and z) is the instantaneous velocity component in the i direction and P is the instantaneous pressure, C is the instantaneous scalar concentration, and Sc is the Schmidt number. The flow and scalar fields are solved using a finite difference method with the fractional step method [51, 52, 53]. The Poisson equation is solved by the conjugate gradient (CG) method [52, 53]. The mass conservation is ensured up to the machine accuracy ($\sim 10^{-14}$). The explicit/implicit hybrid scheme based on the Crank–Nicolson method and the third-order Runge–Kutta method are used for time integration [54]. The schematic of the present computational

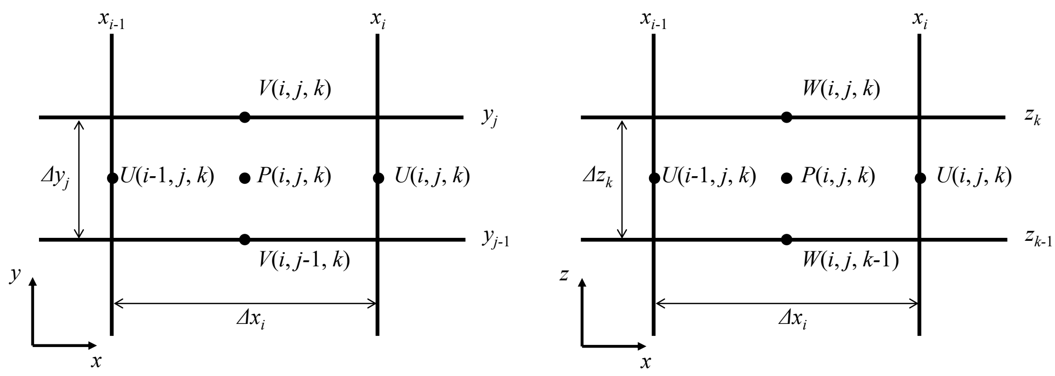

Figure 2.1: Schematic of staggered grid.

domain is shown in Fig. 2.2 (a). Here, the origin of the coordinate system is the center of the fluid inflow and x, y, and z represent the streamwise, vertical, and spanwise directions, respectively. The flow is slip condition in the vertical (y) direction and the periodic condition in the spanwise (z) direction. The scalar is Neumann condition in the vertical (y) direction and the periodic condition in the spanwise (z) direction. The outflow condition for the flow and scalar fields that includes the influence of viscosity is adopted, and it is as follows [55]:

$$\frac{\partial U_i}{\partial t} + U_0 \frac{\partial U_i}{\partial x} = \frac{1}{\mathrm{Re}} \left(\frac{\partial^2 U_i}{\partial y^2} + \frac{\partial^2 U_i}{\partial z^2} \right), \tag{2.4}$$

$$\frac{\partial C}{\partial t} + U_0 \frac{\partial C}{\partial x} = \frac{1}{\mathrm{ReSc}} \left(\frac{\partial^2 C}{\partial y^2} + \frac{\partial^2 C}{\partial z^2} \right), \tag{2.5}$$

where U_0 ($= (U_1 + U_2)/2$; $U_1 = 2.0$ and $U_2 = 1.0$) is the inlet mean streamwise velocity.

The inlet streamwise velocity is given by the following equations:

$$U = U_1 \quad (y/L > 0.16), \tag{I}$$

$$U = U_1 (\frac{y/L}{0.16})^{1/7} \quad (0 < y/L \leq 0.16), \tag{II}$$

$$U = -U_2 (\frac{y/L}{0.26})^{1/7} \quad (-0.26 < y/L \leq 0), \tag{III}$$

$$U = U_2 \quad (y/L \leq -0.26), \tag{IV}$$

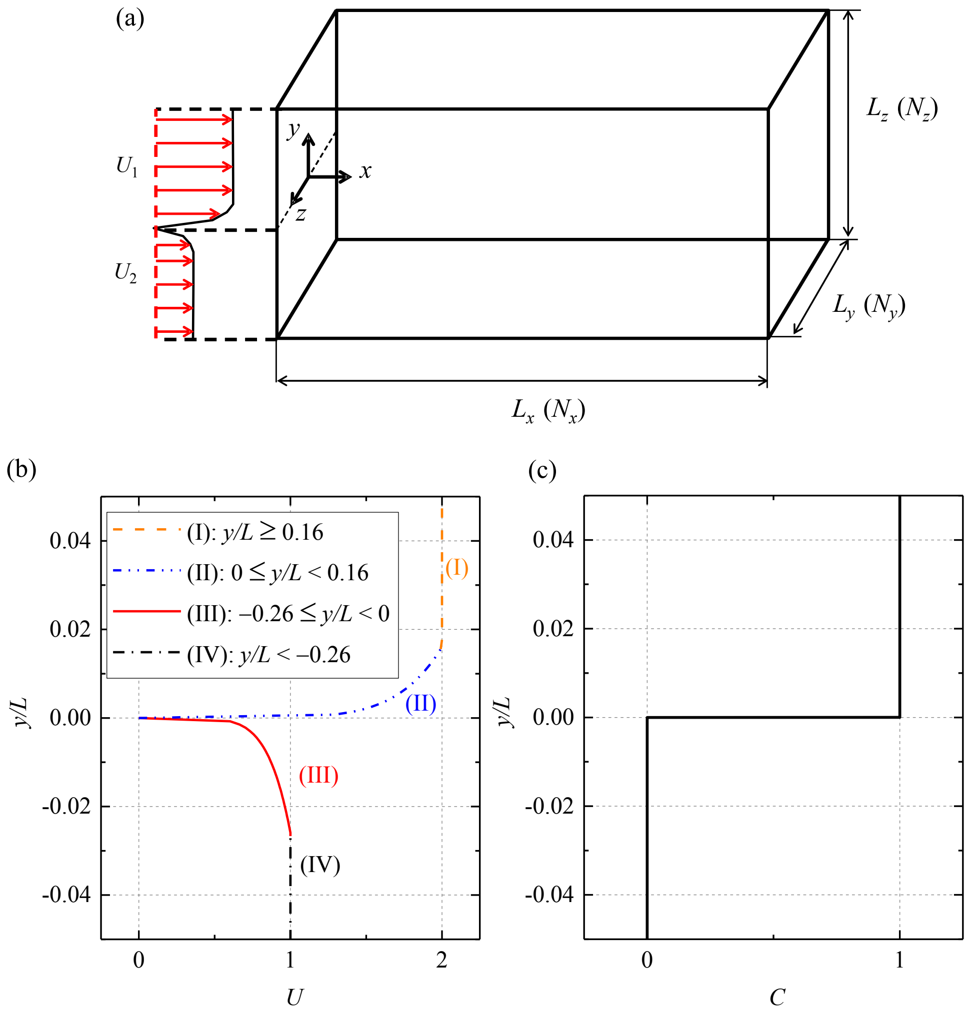

Figure 2.2: Schematics of the (a) cordinate system, (b) inlet streamwise velocity, and (c) inlet scalar concentration. L_x, L_y, and L_z are the computational domain of the streamwise, vertical, and spanwise directions, respectively. N_x, N_y, and N_z are the grid points of the streamwise, vertical, and spanwise directions, respectively.

Figures 2.2 (b) and (c) show the schematic of the inlet streamwise velocity and inlet scalar concentration, respectively. The velocity defect was estimated from the experimental study by Ito et al. [33]. In addition, a uniform random noise with an amplitude of $0.02\Delta U$ ($\Delta U = U_1 - U_2 = 1.0$) was added to the streamwise velocity. A passive scalar is introduced in the upper layer ($y/L > 0$) at a concentration of $C = 1.0$. The Reynolds number, based on U_0 and L, and the Schmidt number are set to $Re = 10,000$ and $Sc = 1$, respectively. Moreover, the Reynolds number based on the 99 % mixing layer thickness and U_2 is $Re_\delta = 130$ [56, 35].

2.2 Algorithms of the combined Runge-Kutta method and fractional step method [57]

The time advancement scheme for Eqs. (2.1) and (2.2) can be written as

$$\frac{\partial U_i^k}{\partial x_i} = 0, \tag{2.6}$$

and

$$\begin{aligned} \frac{U_i^k - U_i^{k-1}}{\Delta t} = \alpha_k \mathbf{L}(U_i^{k-1}) \quad &+ \quad \beta_k \mathbf{L}(U_i^k) - \gamma_k \mathbf{N}(U_i^{k-1}) \\ &- \quad \zeta_k \mathbf{N}(U_i^{k-2}) - (\alpha_k + \beta_k)\frac{\partial P^k}{\partial X_i}, \end{aligned} \tag{2.7}$$

where $\mathbf{L}(U_i)$ and $\mathbf{N}(U_i)$ are the discretization approximations for the viscous term and the convection term, and $\mathbf{L}(U_i)$ and $\mathbf{N}(U_i)$ are as follows:

$$\mathbf{L}(U_i) = \frac{1}{Re}\frac{\partial^2 U_i}{\partial X_j \partial X_j}, \tag{2.8}$$

$$\mathbf{N}(U_i) = \frac{\partial}{\partial X_j} U_i U_j. \tag{2.9}$$

In addition, $k = 1, 2, 3$ means number of the subsep, U_i^0 and U_i^3 denote the instantaneous velocities at step n and $n+1$. In this thesis, $\partial/\partial X_i$ is the finite-difference operator. It can be seen that the viscous and convection terms of Eq. (2.7) are all treated explicitly to avoid repetitive operation. Table 2.1 shows the list of the coefficients α_k, β_k, γ_k, and ζ_k in Eq. (2.7) [58]. Furthermore, Eq. (2.7) is solved as follows in the fractional step method:

Table 2.1: Value of coefficients α_k, β_k, γ_k, and ζ_k [58].

sub-step k	α_k	β_k	γ_k	ζ_k
1	8/15	0	8/15	0
2	5/12	-17/60	5/12	-17/60
3	3/4	-5/12	3/4	-5/12

$$\frac{\hat{U}_i^k - U_i^{k-1}}{\Delta t} = (\alpha_k + \beta_k)\mathbf{L}(U_i^{k-1}) + \beta_k\mathbf{L}(\hat{U}_i^k - U_i^{k-1}) - \gamma_k\mathbf{N}(U_i^{k-1}) - \zeta_k\mathbf{N}(U_i^{k-2}), \tag{2.10}$$

$$\frac{U_i^k - \hat{U}_i^k}{\Delta t} = -\frac{\partial \phi^k}{\partial x_i}. \tag{2.11}$$

Here, ϕ^k in Eq. (2.11) is a function of P^k, U^k, and U^{k-1}, and it satisfies the following equation:

$$\frac{\partial \phi^k}{\partial x_i} = (\alpha_k + \beta_k)\frac{\partial P^k}{\partial x_i} - \beta_k\mathbf{L}(U_i^k - \hat{U}_i^{k-1}). \tag{2.12}$$

The Poisson equation for ϕ^k is derived from Eq. (2.11) and the continuity equation Eq. (2.1), and is shown in the following equation:

$$\frac{\partial^2 \phi^k}{\partial x_i \partial x_i} = \frac{1}{\Delta t}\frac{\partial \hat{U}_i^k}{\partial x_i}. \tag{2.13}$$

Figure 2.3 shows the outline of time progression combining Runge-Kutta method and the fractional step method. The vertical arrows in the figure show the process of correcting the calculation to satisfy the continuity equation at each step.

2.3 Solving the Poisson equation [59]

In this calculation, the Poisson equation for pressure in Eq. (2.13) is solved by using the conjugate gradient (CG) method. The CG method is an algorithm for solving simultaneous linear equations with a symmetric positive definite matrix as a coefficient. This is often used as an iterative method

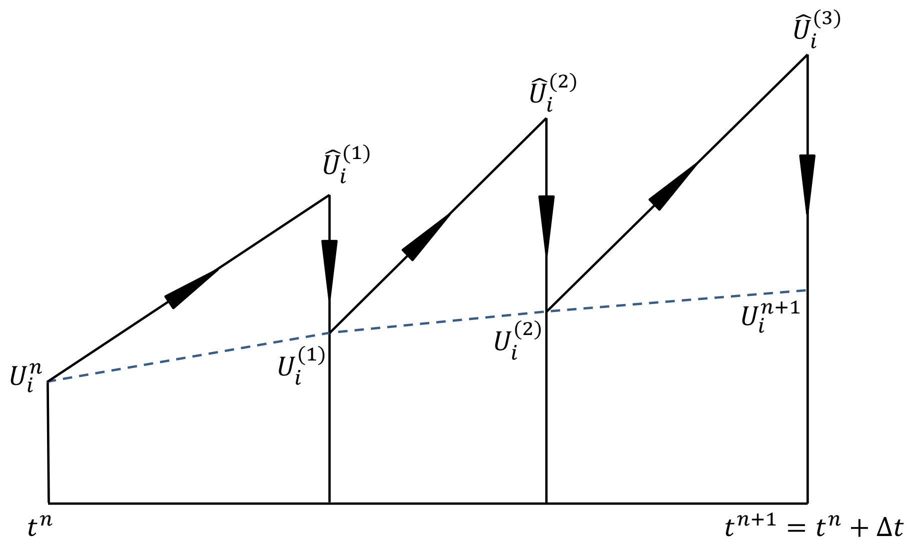

Figure 2.3: The interpolation of the instantaneous velocity.

and is used as a solution to partial differential equations. Here, a linear equation for a vector $\mathbf{x}$ is expressed by the following equation:

$$\mathbf{Ax} = \mathbf{b}. \tag{2.14}$$

Here, $\mathbf{A}$ is the $n \times n$ symmetric positive definite matrix. $\mathbf{b}$ is the one dimensioal matrix of n. First, we substitute $\mathbf{x_0}$ as the predicted value of the solution or $\mathbf{0}$ into the equation. At this time, the initial error $\mathbf{r_0}$ is expressed by the following equation:

$$\mathbf{r_0} = \mathbf{b} - \mathbf{Ax_0}. \tag{2.15}$$

$\mathbf{r_0}$ is replaced with $\mathbf{p_0}$, and initial number is set to $k = 0$. After that, repeat the following process:

$$\alpha_k = \frac{\mathbf{r_k^T r_k}}{\mathbf{p_k^T A p_k}}, \tag{2.16}$$

$$\mathbf{x_{k+1}} = \mathbf{x_k} + \alpha_k \mathbf{p_k}, \tag{2.17}$$

$$\mathbf{r_{k+1}} = \mathbf{r_k} - \alpha_k \mathbf{A p_k}, \tag{2.18}$$

$$\beta_k = \frac{\mathbf{r_{k+1}^T r_{k+1}}}{\mathbf{r_k^T r_k}}, \tag{2.19}$$

$$\mathbf{p_{k+1}} = \mathbf{r_{k+1}} + \beta_k \mathbf{p_k}, \tag{2.20}$$

$$k = k + 1. \tag{2.21}$$

This process is completed when the error $\mathbf{r_{k+1}}$ reaches a sufficiently small value.

Chapter 3

Momentum transport process

3.1 Introduction

Elucidation of the momentum transport process, in free shear flows, is often required in fluid engineering for the modeling and prediction of flows. The shear mixing layer is one of the canonical free shear flows, and since the discovery of large-scale structure by Brown & Roshko [9], numerous studies on both developing laminar shear mixing layers [60, 61, 62] and developed turbulent mixing layers with self-similarity [28, 29, 63] have been carried out over the decades. Moreover, attention has been recently paid to the transition of coherent large structures between the pre- and post-transition mixing layer [26, 27].

Another interesting feature appearing in mixing layers during the transition state is the counter-gradient momentum transport (CGMT), where the momentum is transported against the mean velocity gradient. This phenomenon was observed in the experiments on a liquid shear mixing layer by Huang & Ho [37] and the numerical simulation by Moser and Rogers [17]. Hussain & Zaman [38] and Hussain [39] indicated that the counter-gradient transport of heat and momentum in shear flows is governed by coherent large eddies. Ito *et al.* [33] experimentally investigated the momentum and mass transport in developing and developed shear mixing layers by modifying the initial condition using trip wires. They found that in the developing mixing layer, even though the total momentum transport is positive gradient momentum transport (GMT), negative momentum transport (CGMT) takes place in specific frequency bands. However, the forcibly developed mixing layer by the trip wires can be different from a spatially (naturally) developed turbulent mixing layer. Moreover, the characteristics of the mixing layer in experimental studies highly depend on the experimental system and the initial conditions. For instance, numerical simulations by McMullan and Garrett [64] show that the variation in the initial inflow conditions has a significant influence on the spatial development of turbulence. Laizet *et al.* [35] pointed out that the wake effects of the splitter plate remain even in the self-similar region. Furthermore, Ito *et al.* [33] do not refer to the driving factor of the negative contribution, due to the limited measurable data. In order to clarify that, it is required to conduct numerical simulations, which can provide much more data in comparison with experiments. In this context, the recent development of supercomputers enables us to conduct direct numerical simulations (DNS) in high Reynolds-number flows and large computational domain [30, 31, 65, 66, 67, 68].

In this study, we performed a DNS for a spatially developing shear mixing layer with an emphasis on momentum transport. The computational domain is set relatively large to include from the developing to fully-developed regions. The simulation is aimed at clarifying the driving mechanism and vortical structure of the partial CGMT that appears in the quasi self-similar region, which is highly related to the transition from laminar to turbulence in the mixing layer.

3.2 Numerical setup

In this section, the domain is a rectangular box with a size of $L_x \times L_y \times L_z = 2.1L \times 1.0L \times 0.8L$ resolved by $N_x \times N_y \times N_z = 2,210 \times 1,350 \times 780$ grid points. L is the height of the computational domain. A staggered grid system is employed and the grid size is uniform in the x and z directions while finer meshes are given near the center of the mixing layer ($y = 0$) in the y direction and as follows:

$$\frac{y(j)}{L} = \frac{1}{L_y}\left(1 - \tanh^{-1}\left(\tanh(1.0)\left(1.0 - 2.0\frac{j}{N_y}\right)\right)\right). \tag{3.1}$$

The spatial derivatives of the velocities and scalar are discretized by the fourth-order central difference scheme in the x and z directions and by the second-order central difference scheme in the y direction [69]. The spacing in the x and z directions is constant with a value of $0.001L$. The minimum grid spacing in the y direction is approximately $0.0004L$ at the center. The spatial resolution is smaller than 2.7η. Here, $\eta = (\nu^3\epsilon^{-1})^{1/4}$ is the

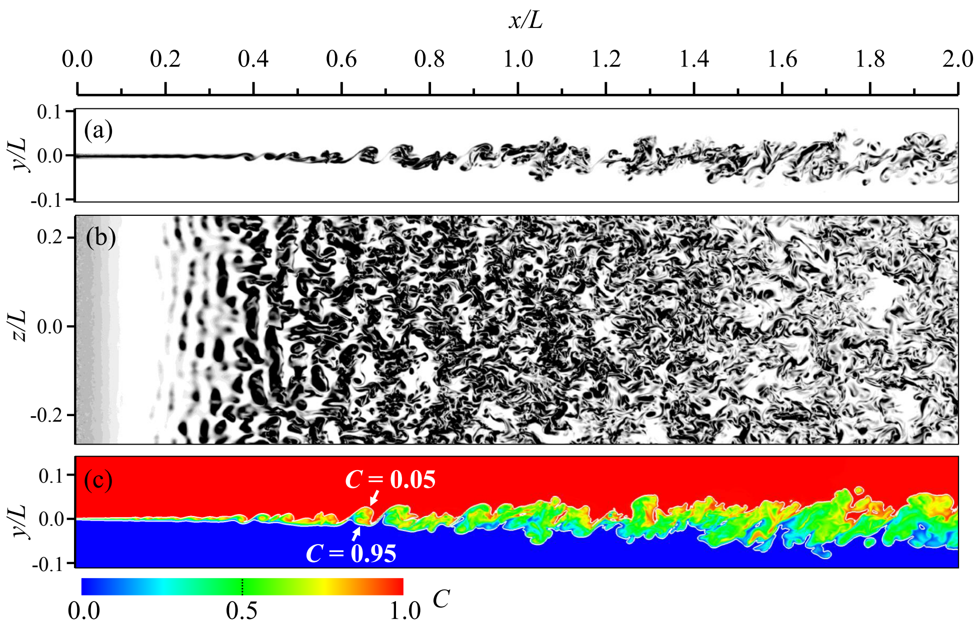

Figure 3.1: Instantaneous images of the flow. (a) Vorticity magnitude on the $x-y$ plane ($z=0$), (b) vorticity magnitude on the $x-z$ plane ($y=0$), and (c) the scalar concentration on the $x-y$ plane ($z=0$).

Kolmogorov length scale and ν and ϵ are the kinematic viscosity and turbulent kinetic energy dissipation rate, respectively. The time step is set to $\Delta t = 5.7 \times 10^{-4}$ and the maximum Courant number is 0.3. In this study, the spatial and time resolutions are comparable to those of the DNSs by Attili and Bisetti [30, 65, 66, 67] and Fiscaletti *et al.* [31, 68].

The computation has been performed for 1,300,000 time steps and 1,000,000 steps were used to obtain reliable statistical values. The statistical values in the present study are arithmetically averaged based on time and the z direction and are denoted with the over bar of the following figures.

3.3 Basic flow characteristics

Figures 3.1 (a) and (b) show instantaneous images of the vorticity magnitude $|\boldsymbol{\omega}| = |\boldsymbol{\nabla} \times \boldsymbol{u}|$ on the $x-y$ ($z=0$) and $x-z$ planes ($y=0$), respectively. In the present study, $\boldsymbol{u} = (u', v', w')$ and u', v', and w' are the instantaneous streamwise, vertical, and spanwise velocity fluctuations, respectively. Figure 3.1 (c) shows the instantaneous scalar concentration on the central plane ($z=0$) at the same time. It is confirmed that when the streamwise distance increases, the mixing layer thickness increases and small-scale disturbances appear more frequently. The scalar mixing proceeds accordingly. The lines of $C = 0.05$ and $C = 0.95$ in Fig. 3.1(c) will be used later to identify the inner region of the mixing layer. Figure 3.2 (a) shows the streamwise distributions of the normalized momentum thickness. They are defined by

$$\delta_U = \frac{1}{\Delta U^2}\int_{-L_y/2}^{L_y/2}(U_1 - \overline{U})(\overline{U} - U_2)dy, \tag{3.2}$$

where $\overline{U}$ is the local mean streamwise velocity. δ_{U0} is the initial momentum thickness obtained by extending the line that indicates the rate of the mixing layer development in $0.7 \leq x/L \leq 2.0$ to $x = 0$ by the least squares method (Fig. 3.2 (a)), and about $0.005L$. δ_U is known to increase linearly with the streamwise distance in the turbulent mixing layer [16]. In the present study, linearity appears from $x/L = 0.7$ ($x/\delta_{U0} = 140$). The spreading rate of the mixing layer, $d\delta_U/dx$, against $(U_1 - U_2)/(U_1 + U_2)$ is shown in Fig. 3.2 (b). Although it strongly depends on the initial conditions and spanwise length of the domain [70], it is basically a function of $(U_1 - U_2)/(U_1 + U_2)$ [8, 25]. Figure 3.2 (b) indicates that the present flow is typical compared with prior research [9, 16, 30, 38, 70, 71, 72, 73, 74, 75, 76, 77, 78, 79].

Figure 3.3 shows the streamwise distributions of the mean-squared velocity fluctuations and the Reynolds shear stress. It illustrates that the peak appears approximately at $x/L = 0.5$ ($x/\delta_{U0} = 100$) for all cases, which is similar to the results by Attili and Bisetti [30]. The values become constant as it proceeds toward the downstream direction [46]. The vertical location where U_0 appears in the slower-stream side ($y < 0$) in the downstream region but the shift reaches a maximum of 3 % with respect to the 99 % of the mixing layer thickness. Therefore, $y = 0$ can be regarded as the center of the mixing layer under discussion in the present paper.

Self-similarity for the velocity fluctuations and the Reynolds shear stress are demonstrated in Fig. 3.4. All values are normalized by the maximum value of the vertical distribution of each statistic at a certain streamwise location, $(\square)_{max}$, and y_{max} is the vertical location where the maximum of each variable exists. All statistics collapse from $x/L = 0.67$ ($x/\delta_{U0} = 137$). Thus, the present mixing layer is self-preserved downstream of $x/L = 0.67$ ($x/\delta_{U0} = 137$). In addition, to confirm the turbulent state, the power

(a)

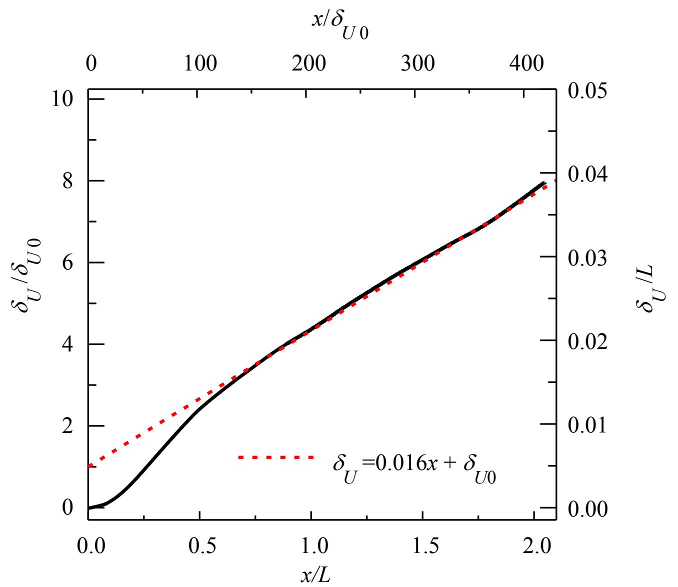

(b)

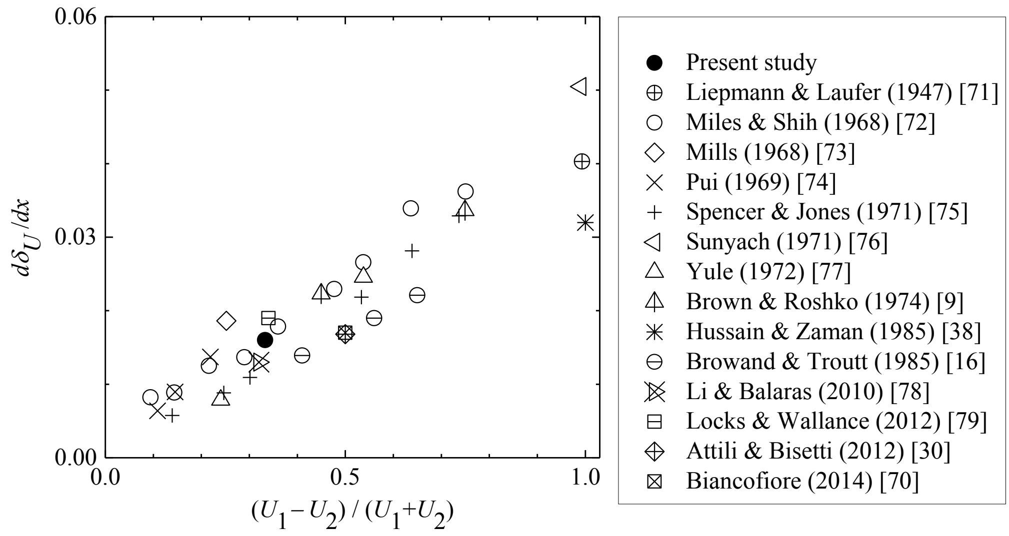

Figure 3.2: Development of the momentum thickness. (a) Streamwise distribution of the normalized momentum thickness; (b) $d\delta_U/dx$ vs. $(U_1 - U_2)/(U_1 + U_2)$. Data from prior research [9, 16, 30, 38, 70, 71, 72, 73, 74, 75, 76, 77, 78, 79] are also plotted.

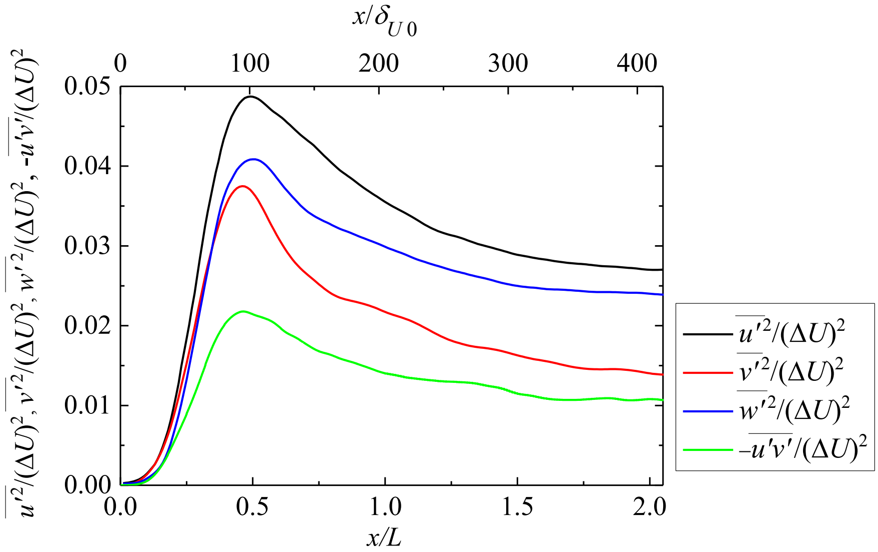

Figure 3.3: Streamwise distributions of the mean-squared velocity fluctuations and the Reynolds shear stress at the center ($y = 0$).

spectra for the streamwise velocity fluctuation were calculated. The power spectra were obtained from the time series data at a fixed point and frequency f was converted to wavenumber k by $k = 2\pi f/\overline{U}$. In the present study, the turbulence level is approximately from 10 % to 15 % at the center; therefore, one may doubt the applicability of the Taylor's frozen turbulence hypothesis. In order to confirm its validity, we reconstructed a spatial vorticity field from the time series data of the velocity obtained at $x/L = 0.78$ and compared it with that obtained from the instantaneous flow field. Here, the convective velocity is used for the local mean streamwise velocity. The result shows that the medium-to-large-scale structures, which we are interested in, are very similar in the two images, indicating that the hypothesis is valid (Figs. 3.5).

Figure 3.6 shows the instantaneous pressure distributions together with a velocity vector map of the first mode of the proper orthogonal decomposition (POD) analysis. Note that although the pressure of streamwise direction is unsteady, we treat it as stationary because the region of the streamwise direction is set to the length that can be regarded as steady state. Furthermore, Fig. 3.7 shows the normalized power spectra of the pressure fluctuations at the center ($y = 0$) and $x/L = 0.78$, 1.38, and 1.95 ($x/\delta_{U0} = 160$, 283, and 399). It is confirmed that, in the upstream region

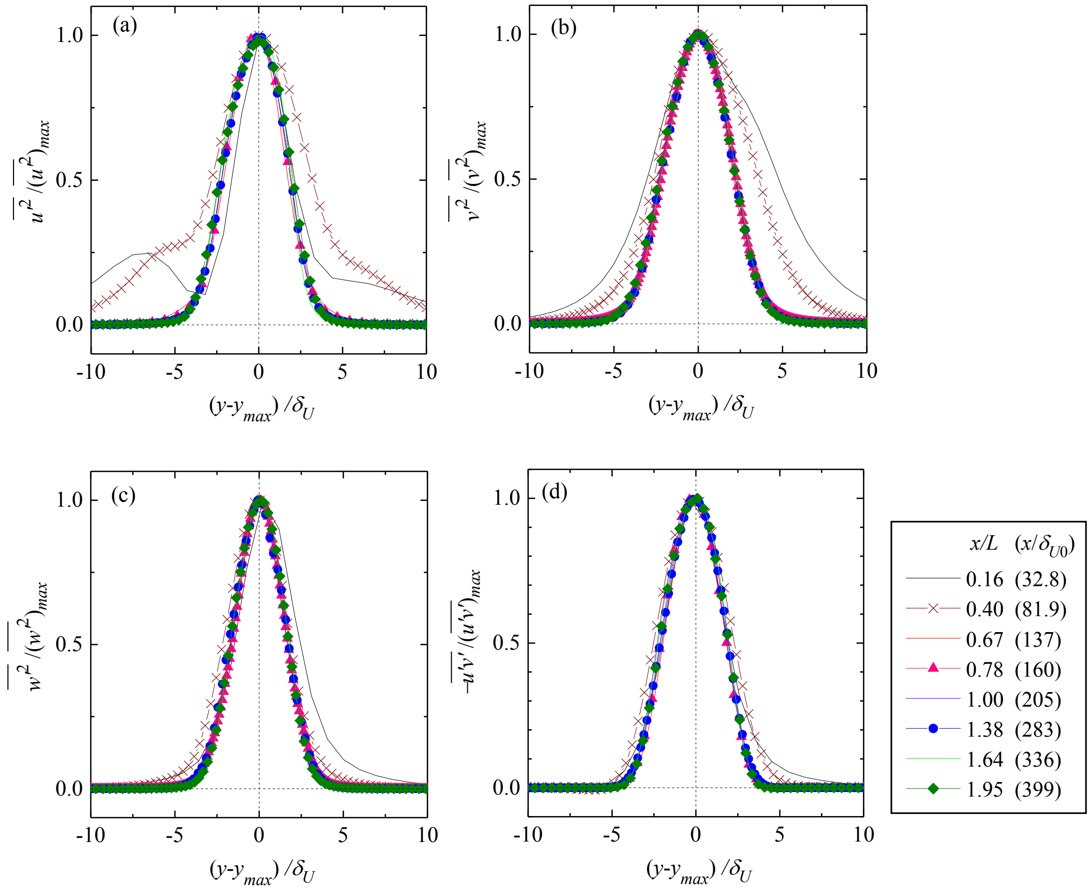

Figure 3.4: Vertical distributions of the mean-squared values of the (a) streamwise, (b) vertical, and (c) spanwise velocity fluctuations, as well as (d) the Reynolds shear stress for the streamwise and vertical velocity fluctuations.

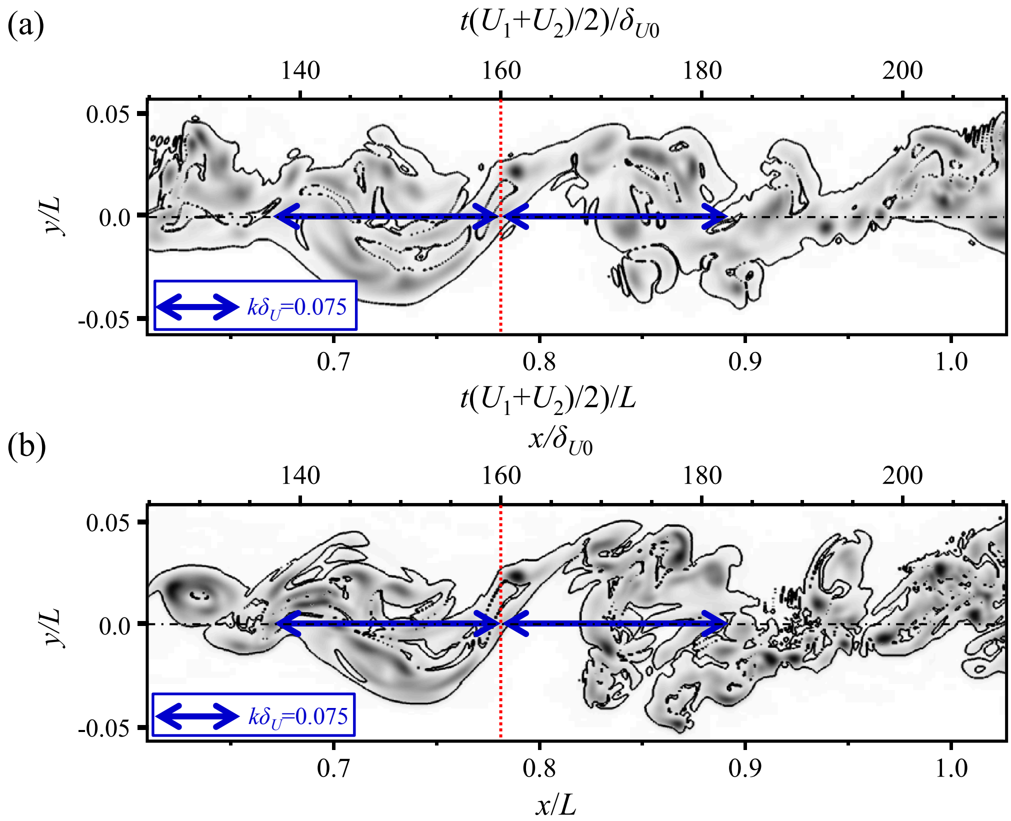

Figure 3.5: (a) Vorticity profiles reconstructed from the time-series data and (b) obtained from the real velocity field.

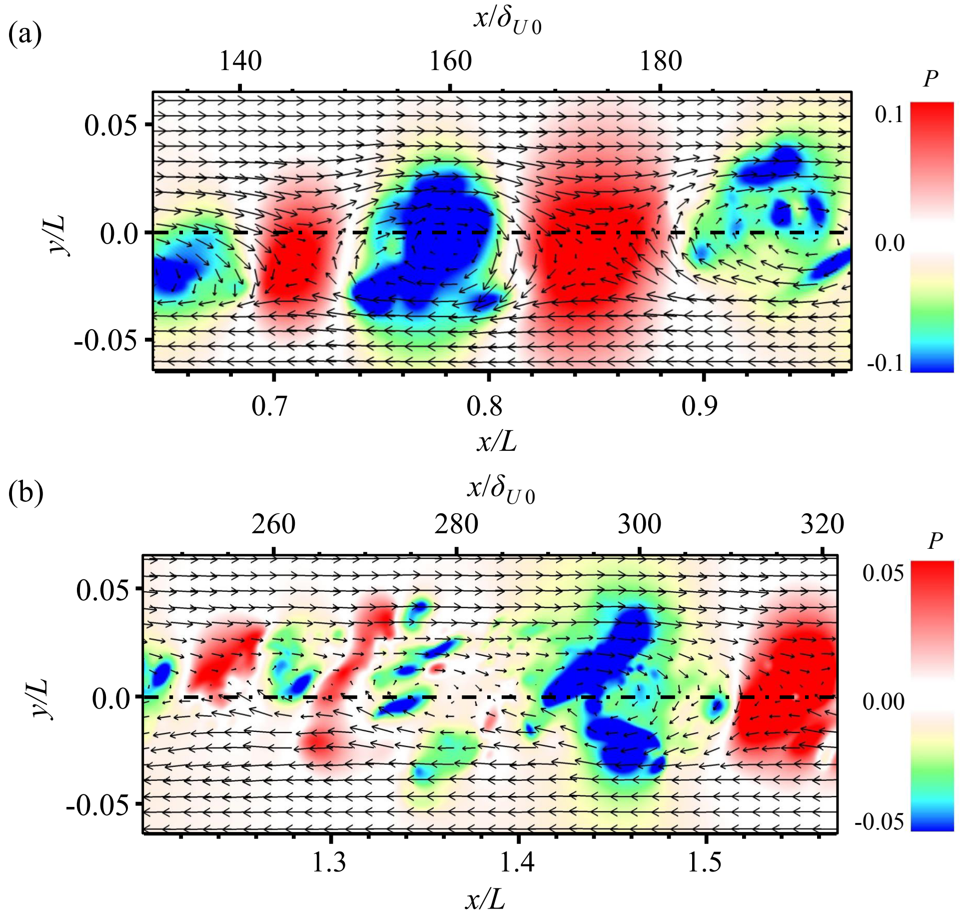

Figure 3.6: Color contour map of the instantaneous pressures in the (a) upstream ($x/L = 0.7 - 0.9$) and (b) downstream ($x/L = 1.2 - 1.6$) regions on the central plane ($z = 0$). The vectors represent the velocity of the first mode of the POD analysis.

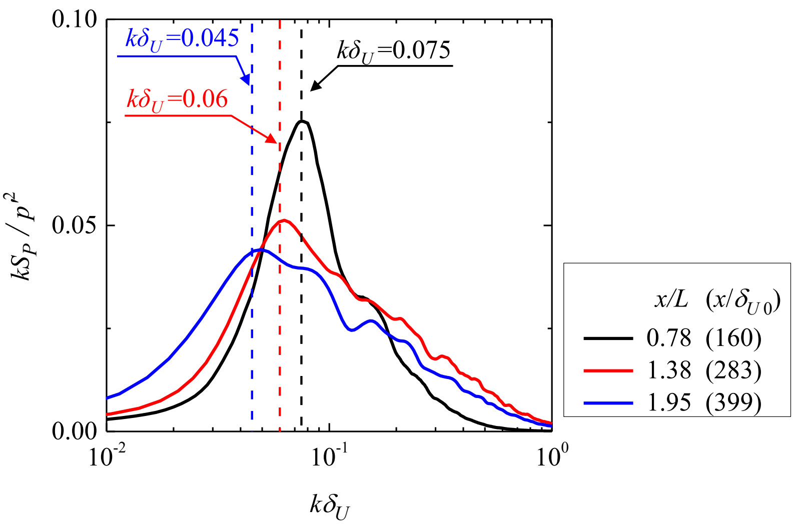

Figure 3.7: Normalized power spectra for the pressure fluctuation at the center ($y = 0$). The dashed line shows the peak frequency of each spectrum.

(Fig. 3.6 (a)), negative and positive pressures appear alternatively at regular intervals, which correspond to the coherent vortical and stretching regions, respectively. The distance between the centers of the high- or low-pressure regions is approximately $k\delta_U = 0.075$, and it links to the peak wavenumber for the pressure power spectrum at $x/L = 0.78$ ($x/\delta_{U0} = 160$) (Fig. 3.7). In the downstream region (Fig. 3.6 (b)), the vortical and stretching regions are also confirmed but with random intervals. The randomness makes the shape of the pressure power spectrum broader and less peaky.

3.4 Budget for momentum transport

As shown in Fig. 3.4 (d), $-\overline{u'v'} > 0$ at all locations. Here, $-\overline{u'v'} > 0$ represents the GMT (positive production) and $-\overline{u'v'} < 0$ represents the CGMT (negative contribution). Therefore, the overall momentum is transported positively (i.e., $-\overline{u'v'} > 0$) at all locations. The co-spectra for the Reynolds shear stress at $x/L = 0.78, 1.38$, and 1.95 ($x/\delta_{U0} = 160$, 283, and 399) are analyzed to clarify the scale dependency of the momentum transport. The results are shown in Fig. 3.8. The vertical location and wavenumber are normalized by the momentum thickness. Figure 3.8 illustrates that the co-spectra take positive values (GMT) in the entire scale at all three locations. However, at $x/L = 0.78$ ($x/\delta_{U0} = 160$), there is a clear trend of the CGMT,

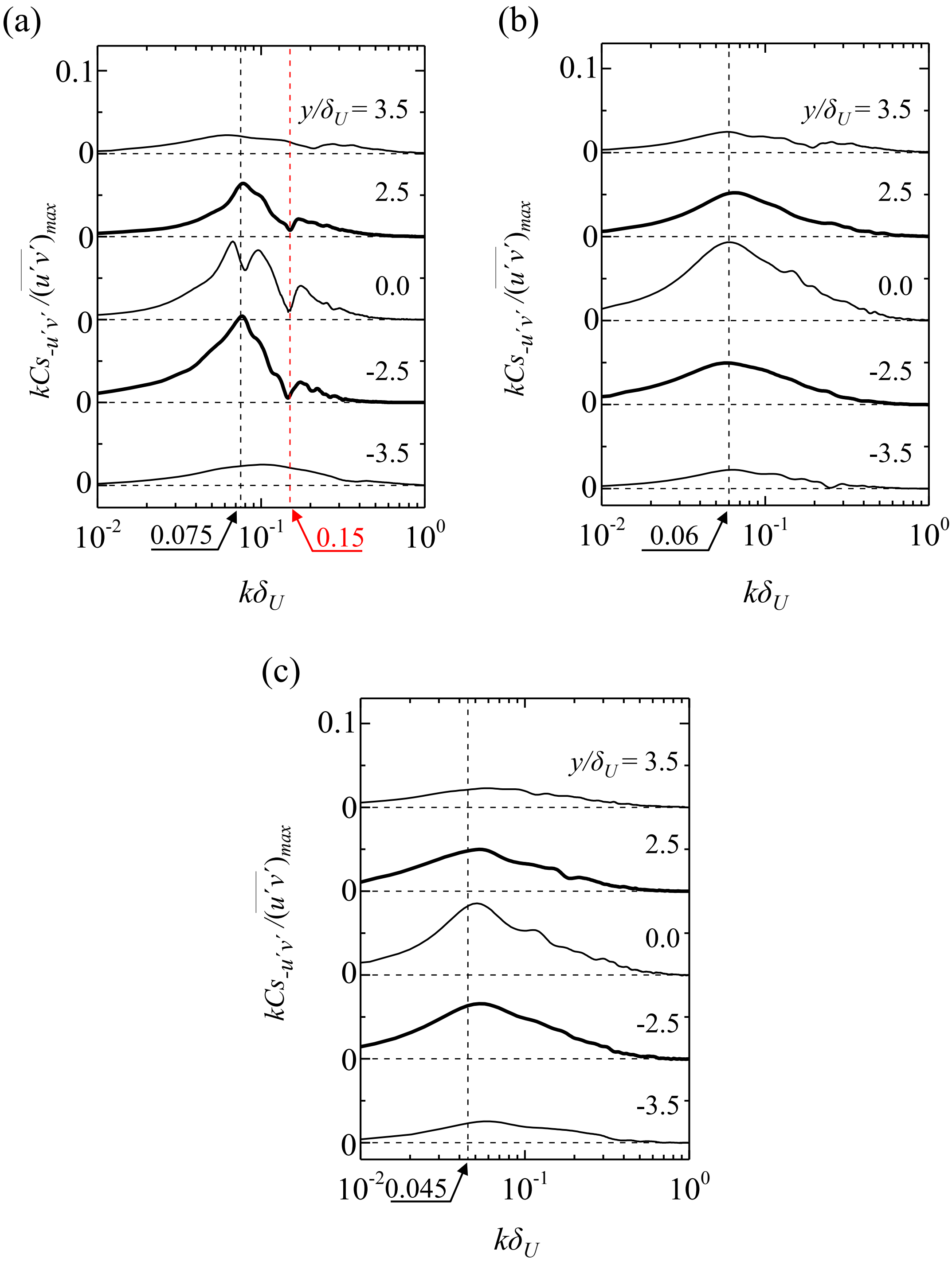

Figure 3.8: Co-spectra for the Reynolds shear stress at (a) $x/L = 0.78$ ($x/\delta_{U0} = 160$), (b) $x/L = 1.38$ ($x/\delta_{U0} = 283$), and (c) $x/L = 1.95$ ($x/\delta_{U0} = 399$).

approximately at $k\delta_U = 0.15$ at the off-central regions ($y/\delta_U = \pm 2.5$) and approximately at $k\delta_U = 0.075$ and 0.15 at the central region ($y/\delta_U = 0$). In other words, the momentum transport process varies even in the self-similar region of $x/L > 0.67$. The peak wavenumber ($k\delta_U = 0.15$) corresponds to the half distance between the coherent vortices.

To investigate the driving mechanism of this phenomenon, the budget of the momentum transport equation for the Reynolds shear stress is examined. The equation is written as follows:

$$
\begin{aligned}
0 &= \overline{\mathcal{C}}_{u'v'} + \overline{\mathcal{P}}_{u'v'} + \overline{\epsilon}_{u'v'} + \overline{\Pi}_{u'v'} + \overline{\mathcal{D}}_{u'v'}, && (3.3)\\
\overline{\mathcal{C}}_{u'v'} &= \overline{U_k}\frac{\partial}{\partial x_k}\overline{u'v'}, && (3.4)\\
\overline{\mathcal{P}}_{u'v'} &= \left[\overline{v'u'_k}\frac{\partial \overline{U}}{\partial x_k} + \overline{u'u'_k}\frac{\partial \overline{V}}{\partial x_k}\right], && (3.5)\\
\overline{\epsilon}_{u'v'} &= 2\nu\left[\overline{\left(\frac{\partial u'}{\partial x_k}\right)\left(\frac{\partial v'}{\partial x_k}\right)}\right], && (3.6)\\
\overline{\Pi}_{u'v'} &= -\overline{p'\left(\frac{\partial u'}{\partial y} + \frac{\partial v'}{\partial x}\right)}, && (3.7)\\
\overline{\mathcal{D}}_{u'v'} &= \overline{\mathcal{D}^{\mathcal{T}}}_{u'v'} + \overline{\mathcal{D}^{\nu}}_{u'v'} + \overline{\mathcal{D}^{\mathcal{P}}}_{u'v'} \\
&= \left[-\frac{\partial}{\partial x_k}\overline{u'v'u'_k}\right] + \left[\nu\frac{\partial}{\partial x_k}\left(\frac{\partial \overline{u'v'}}{\partial x_k}\right)\right] \\
&\quad + \left[-\frac{\partial(\overline{p'u'})}{\partial y} - \frac{\partial(\overline{p'v'})}{\partial x}\right]. && (3.8)
\end{aligned}
$$

The right-hand terms in Eq. (3.3) are called convection term, $\overline{\mathcal{C}}_{u'v'}$, production term, $\overline{\mathcal{P}}_{u'v'}$, dissipation term, $\overline{\epsilon}_{u'v'}$, pressure-strain correlation term, $\overline{\Pi}_{u'v'}$, and diffusion term $\overline{\mathcal{D}}_{u'v'}$, respectively. Furthermore $\overline{\mathcal{D}}_{u'v'}$ can be divided into turbulent diffusion term, $\overline{\mathcal{D}^{\mathcal{T}}}_{u'v'}$, viscous diffusion term, $\overline{\mathcal{D}^{\nu}}_{u'v'}$, and pressure diffusion term, $\overline{\mathcal{D}^{\mathcal{P}}}_{u'v'}$ as shown in Eq. (3.8). Figures 3.9 (a)–(c) show the budget for the momentum transport at $x/L = 0.78$, 1.38, and 1.95 ($x/\delta_{U0} = 160$, 283, and 399), respectively. It is found that $\overline{\mathcal{C}}_{u'v'}$ and $\overline{\mathcal{D}^{\nu}}_{u'v'}$ are negligibly small. The contributions of the dissipation term, pressure-strain correlation term, turbulent diffusion term, and pressure diffusion term at different locations are plotted in Figs. 3.10 (a)–(d), respectively. In addition, the pressure-correlation term can be decomposed into $-\overline{p'(\partial u'/\partial y)}$ and $-\overline{p'(\partial v'/\partial x)}$ as shown in Fig. 3.11. Note that the terms

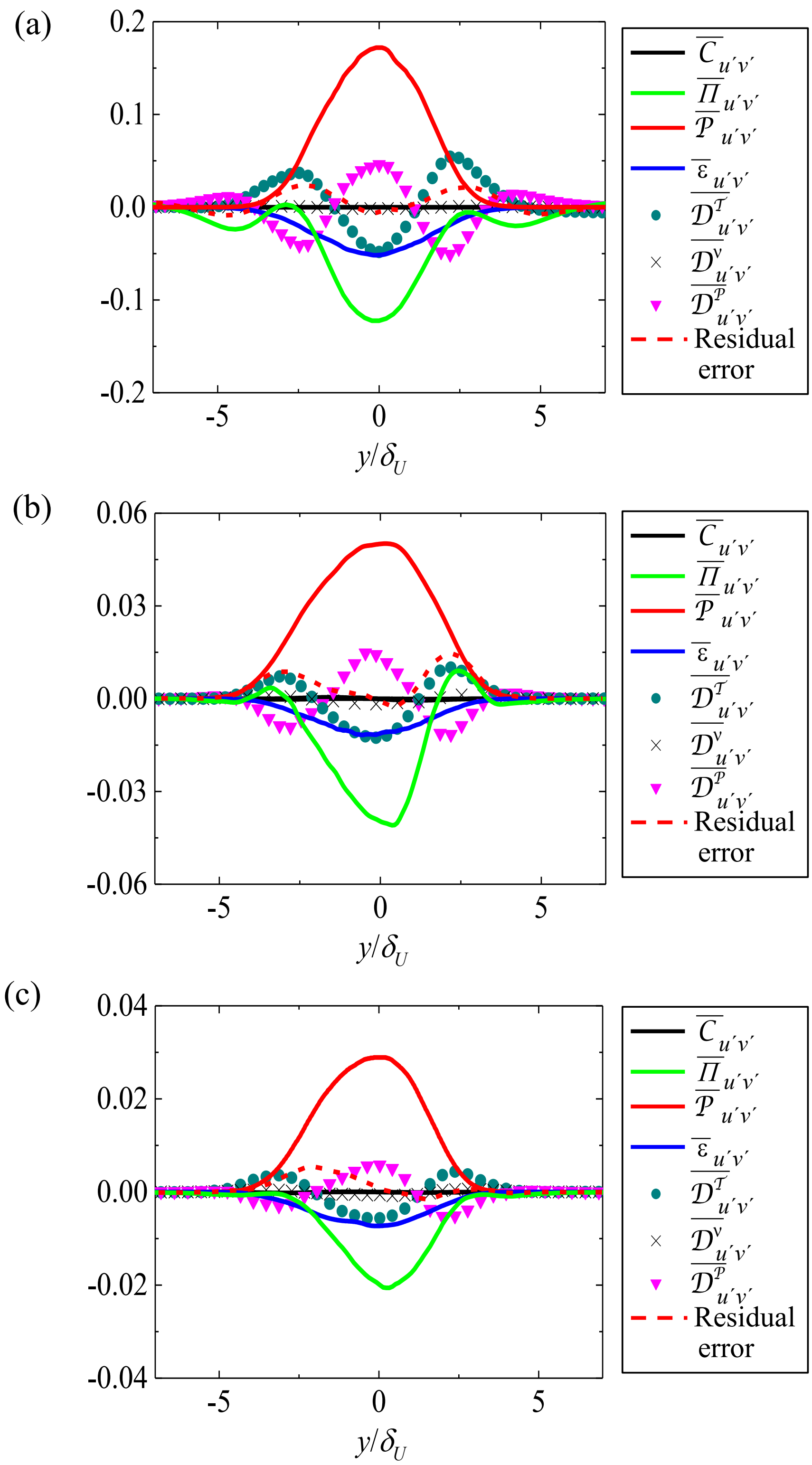

Figure 3.9: Budget for the momentum transport at (a) $x/L = 0.78$ ($x/\delta_{U0} = 160$), (b) $x/L = 1.38$ ($x/\delta_{U0} = 283$), and (c) $x/L = 1.95$ ($x/\delta_{U0} = 399$).

are normalized by the maximum value of the production term, $(\overline{\mathcal{P}}_{u'v'})_{max}$, at each streamwise location to clarify the structural differences. The figures indicate that the driving mechanism of the CGMT varies depending on the vertical location. More specifically, in the pressure diffusion term negative contribution appears only at $y/\delta_U = \pm 2.5$, while in the dissipation, pressure-strain correlation, and turbulent diffusion terms it appears around at $y/\delta_U = 0$. Moreover, the change in the pressure-strain correlation term is not monotonous and shows a bouncing motion between the negative and positive productions at the off-central region ($y/\delta_U = \pm 2.5$). Interestingly, similar behavior is observed in a stably-stratified shear flow, where the CGMT takes place [80], although the driving force is surely different. Since it is indicated that the mechanism depends on the vertical location, we will discuss the phenomenon at the central ($y/\delta_U = 0$) and off-central regions ($y/\delta_U = \pm 2.5$) separately.

First, we will focus on $y/\delta_U = \pm 2.5$. The pressure diffusion term is investigated because it is the only term that represents the loss of the Reynolds stress at this location. The power spectra for the pressure diffusion, which are normalized by the maximum value of the production term at each streamwise location, $(\overline{\mathcal{P}}_{u'v'})_{max}$, are shown in Fig. 3.12. At $x/L = 0.78$ ($x/\delta_{U0} = 160$), a peak appears at $k\delta_U \sim 0.15$ for the distribution at $y/\delta_U = \pm 2.5$, whereas such a peak does not appear at $y/\delta_U = 0$. Furthermore, this is the same wavenumber as the one appearing in the co-spectrum for the Reynolds shear stress (Fig. 3.8). In addition, the peak becomes smooth at $x/L = 1.38$ ($x/\delta_{U0} = 283$) and 1.95 ($x/\delta_{U0} = 399$), which is the same trend as in the co-spectrum for the Reynolds shear stress. Hence, the pressure diffusion term is thought to contribute to the CGMT in the off-central region.

$k\delta_U = 0.15$ at $x/L = 0.78$ ($x/\delta_{U0} = 160$) and $y/\delta_U = \pm 2.5$ corresponds to the half distance between the coherent vortices estimated by the pressure spectrum (Fig. 3.7). In order to capture the phenomenological image of the flow field, we show the instantaneous color contour map of the pressure diffusion term in Fig. 3.13. On the $y/\delta_U = \pm 2.5$ lines, the negative region of the $-u'v'$ (i.e., CGMT), indicated by the black line, appears at specific locations with an interval of $k\delta_U = 0.15$ in the upstream region (Fig. 3.13 (a)). Both the negative regions of the Reynolds shear stress and pressure diffusion term appears periodically at the same intervals; however, the negative regions overlap only partially. In the downstream region (Fig. 3.13 (b)),

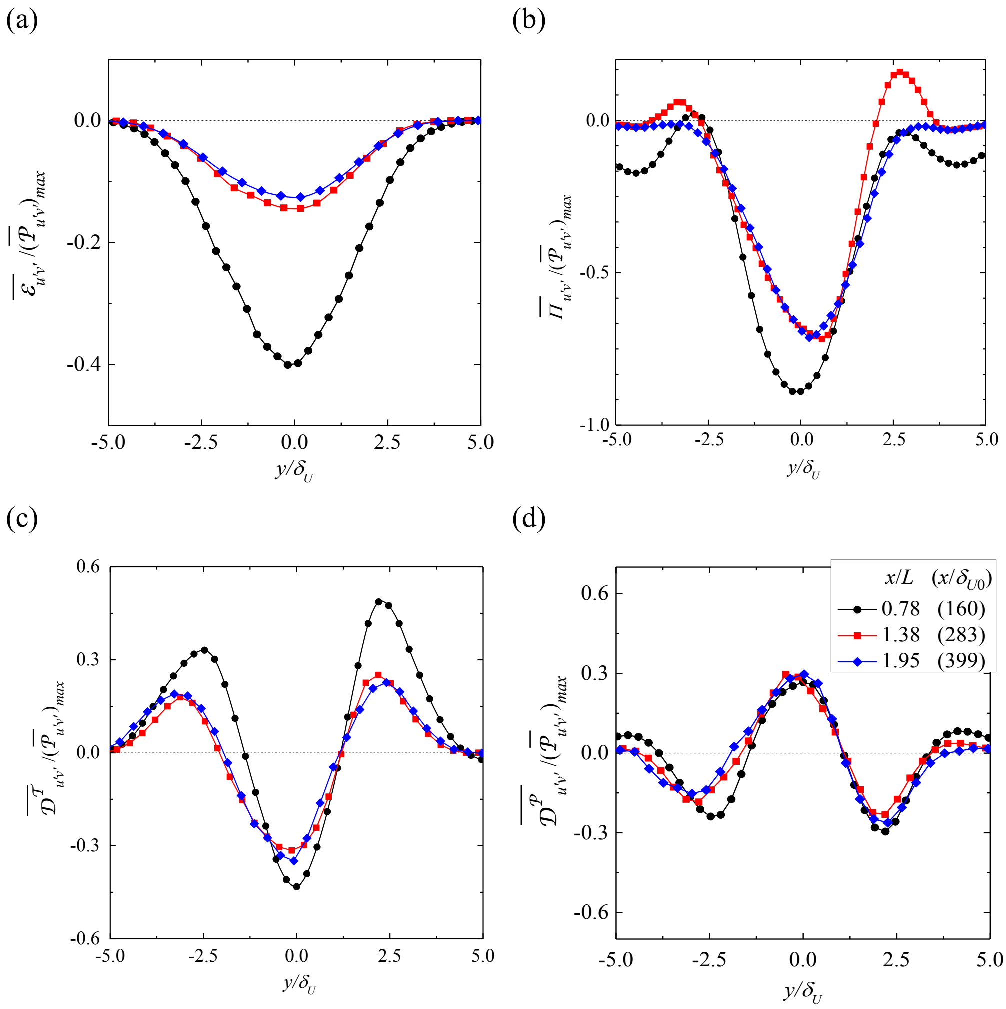

Figure 3.10: Budget terms normalized by the production term. (a) dissipation term; (b) pressure-strain correlation term; (c) turbulent diffusion term; (d) pressure diffusion term. The y-axis is normalized by the maximum value of the production term, $(\overline{\mathcal{P}}_{u'v'})_{max}$, at each streamwise location.

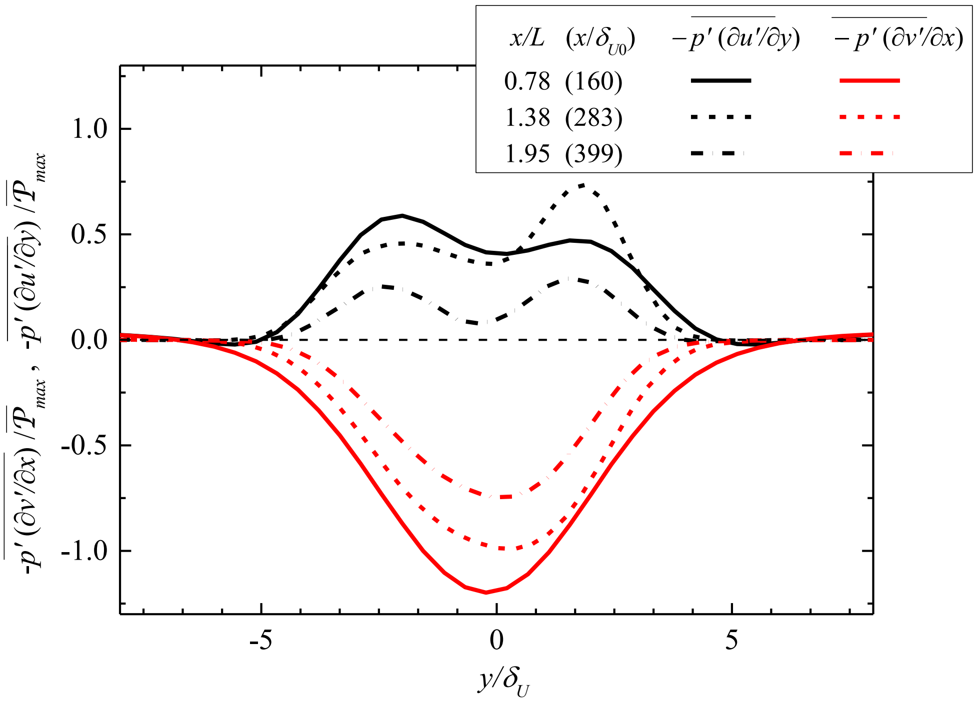

Figure 3.11: Distribution of the pressure-strain correlation term decomposed into $-p'(\overline{\partial u'/\partial y})$ and $-p'(\overline{\partial v'/\partial x})$.

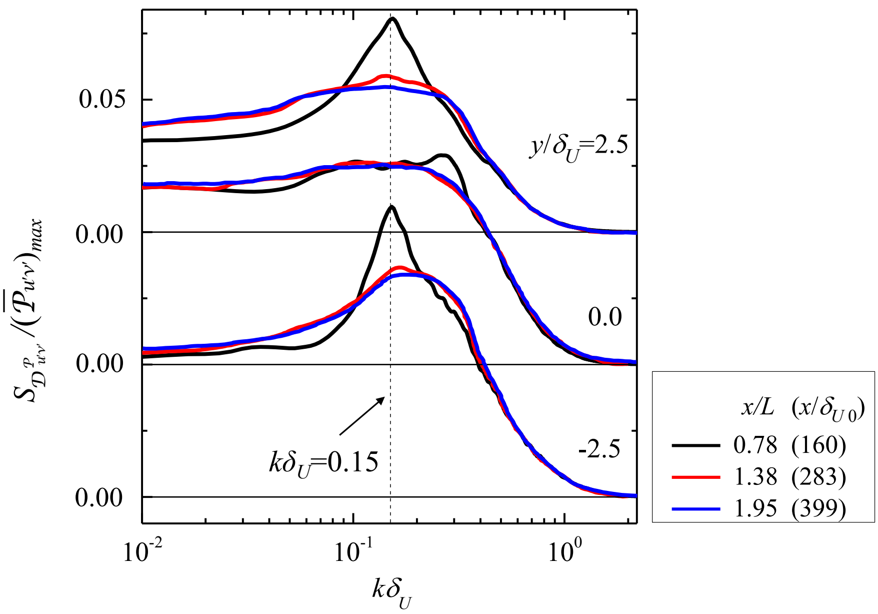

Figure 3.12: Power spectra for the pressure diffusion term normalized by the maximum value of the production term at each streamwise location.

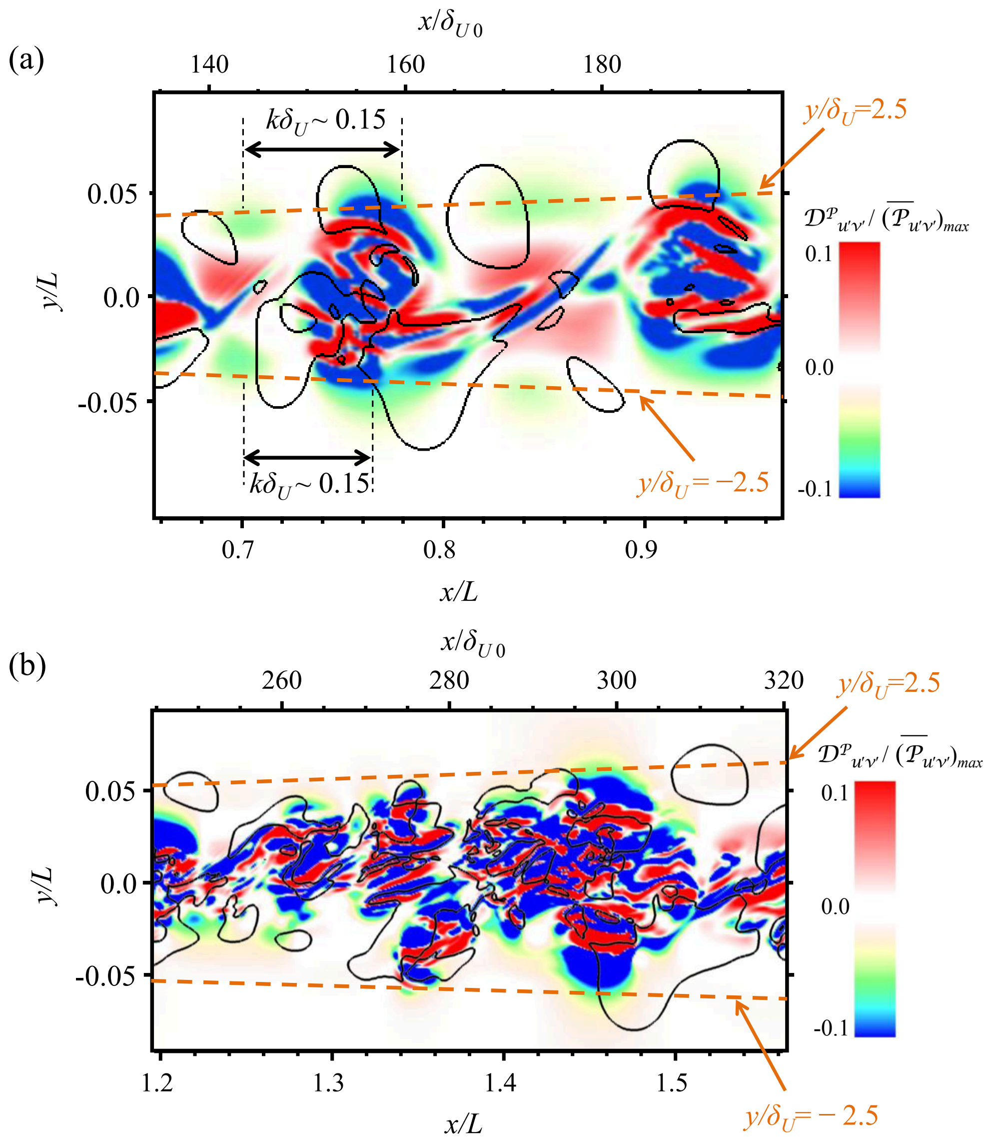

Figure 3.13: Instantaneous color contour map of the pressure diffusion term in the (a) upstream ($x/L = 0.7-0.9$) and (b) downstream ($x/L = 1.2-1.6$) regions on the center plane ($z = 0$). The area surrounded by the black line indicates the CGMT ($-u'v' < 0$).

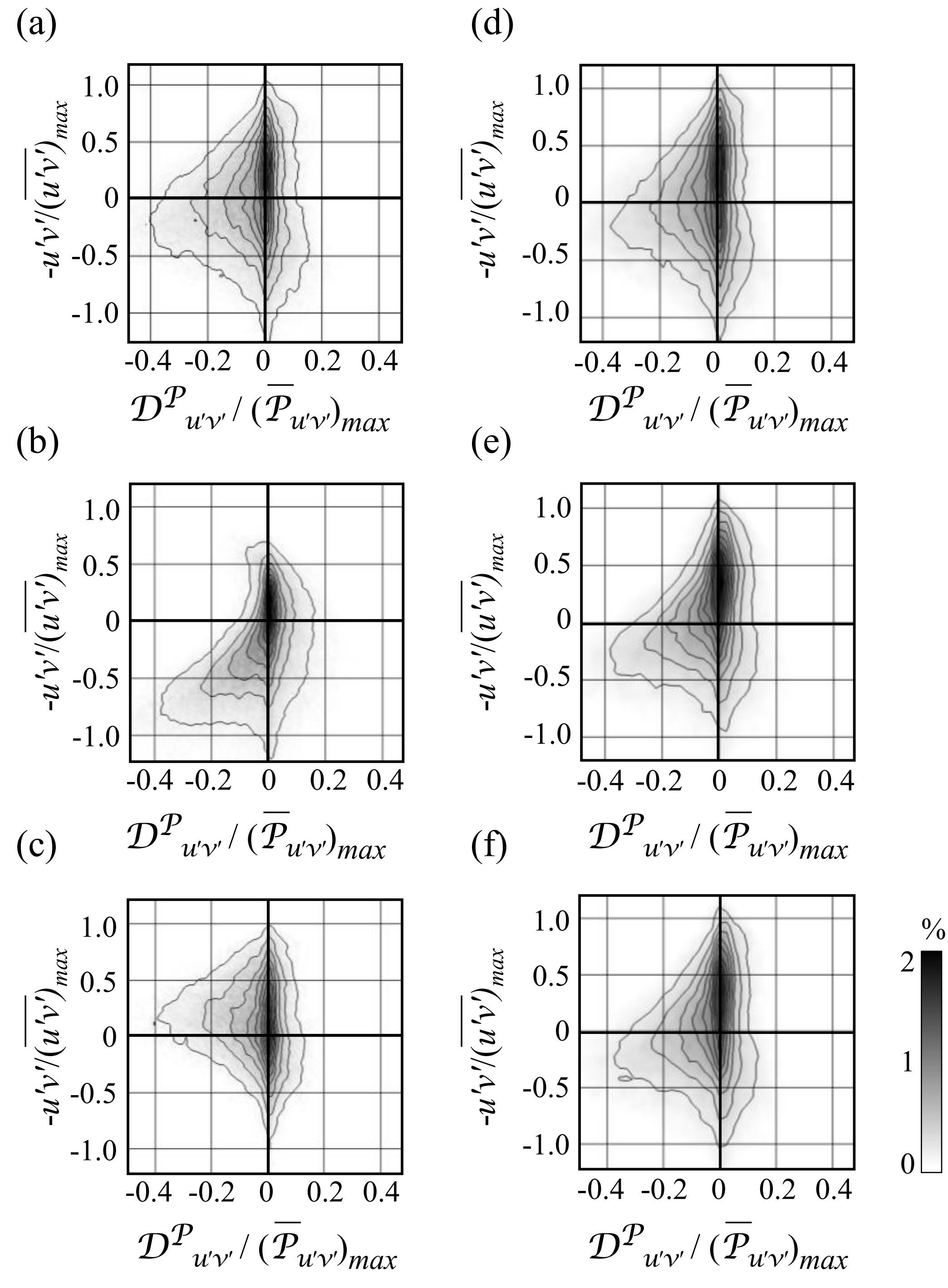

Figure 3.14: Joint PDFs for the Reynolds shear stress and pressure diffusion term in the (a–c) upstream ($x/L = 0.78$) and (d–f) downstream ($x/L = 1.38$) regions at $y/\delta_U = 2.5$, respectively. (a, d) $k\delta_U = 0.065 - 0.09$; (b, e) $k\delta_U = 0.08 - 0.30$; (c, f) $k\delta_U = 0.22 - 0.54$.

the relationship of the negative regions between the Reynolds shear stress and pressure diffusion term becomes unclear and both the negative regions appearances become more random. Consequently, it loses the signature of the CGMT at the specific wavenumber bands.

In the present simulation, the trend of CGMT at the specific wavenumber bands is observed. However, the value of the Reynolds shear stress is on the positive (GMT) side at all wavenumbers and it is not obvious if the pressure diffusion term is truly contributing to the loss of the Reynolds stress. Hence, we calculated the joint PDF for the Reynolds shear stress and pressure diffusion term in the upstream ($x/L = 0.78$) and downstream ($x/L = 1.38$) regions at $y/\delta_U = 2.5$. Note that the negative Reynolds shear stress and the negative pressure diffusion term appear alternately as shown in Fig. 3.13(a). Therefore, shift adjustments are required to visualize the negative contribution and the relationship between the two terms on the joint PDF map. Thus we performed an orthogonal wavelet decomposition [81] with 20 wavelet basis and calculated the optimal degree of the shift that maximizes the correlation between the two terms at each wavenumber bands. The resulting joint PDFs optimized for the wavenumber bands of $k\delta_U = 0.065 - 0.09$, $0.08 - 0.30$, and $0.22 - 0.54$ are shown in Figs. 3.14 (a)–(c), respectively. In Fig. 3.14 (b) a large negative momentum production prevails in the third quadrant, meaning that the CGMT does occur at this specific wavenumber band and is highly related with the pressure diffusion term in the upstream region. In contrast, such a positive relationship is not seen in Figs. 3.14 (a) and (c), meaning that the CGMT is not strongly correlated with the eddies with wavenumbers of $k\delta_U = 0.065 - 0.09$ and $0.22 - 0.54$. In the downstream region, the PDF weakly prevails in the third quadrant for all wavenumber bands (Figs. 3.14 (d)–(f)), meaning that the negative Reynolds shear stress still exists but is dispersed with streamwise distance. In other words, the event transforms from periodic to random as it moves toward the downstream region. Figure 3.13 (b) indicates that the randomness is caused by the deformation and merge of the coherent vortices. Finally, we demonstrated that similar results are obtained for $y/\delta_U = -2.5$.

On the other hand, the CGMT at the central region of the mixing layer is observed in the pressure-strain correlation and turbulent diffusion terms. We exclude the dissipation term from the driving mechanisms of the CGMT because it is passive.

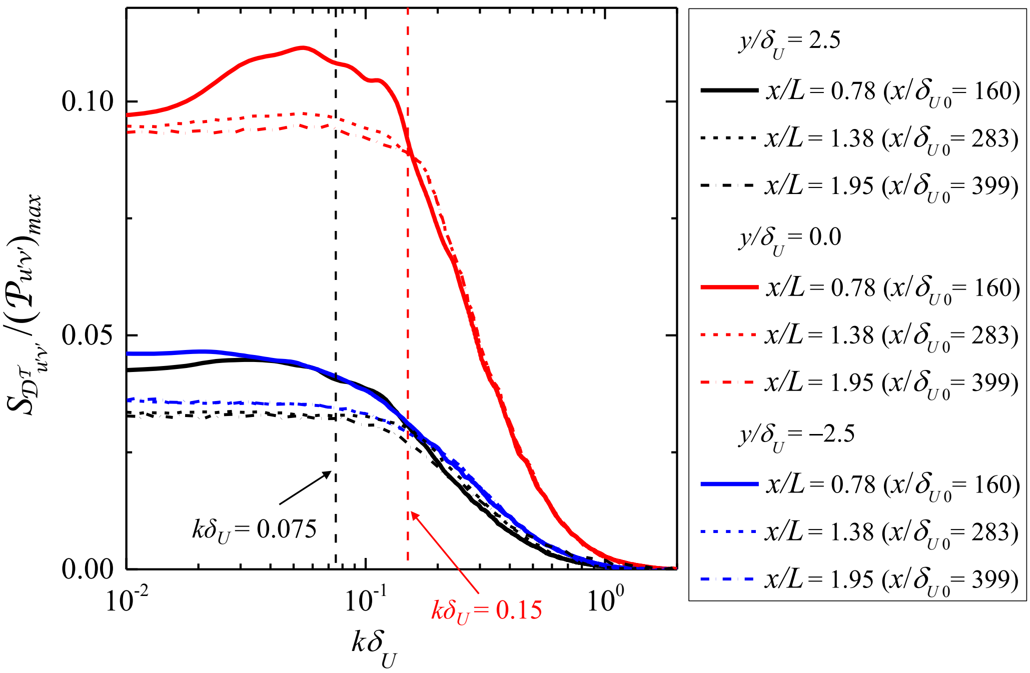

Figure 3.15: Power spectra for the turbulent diffusion term normalized by the maximum value of the production term at each streamwise location.

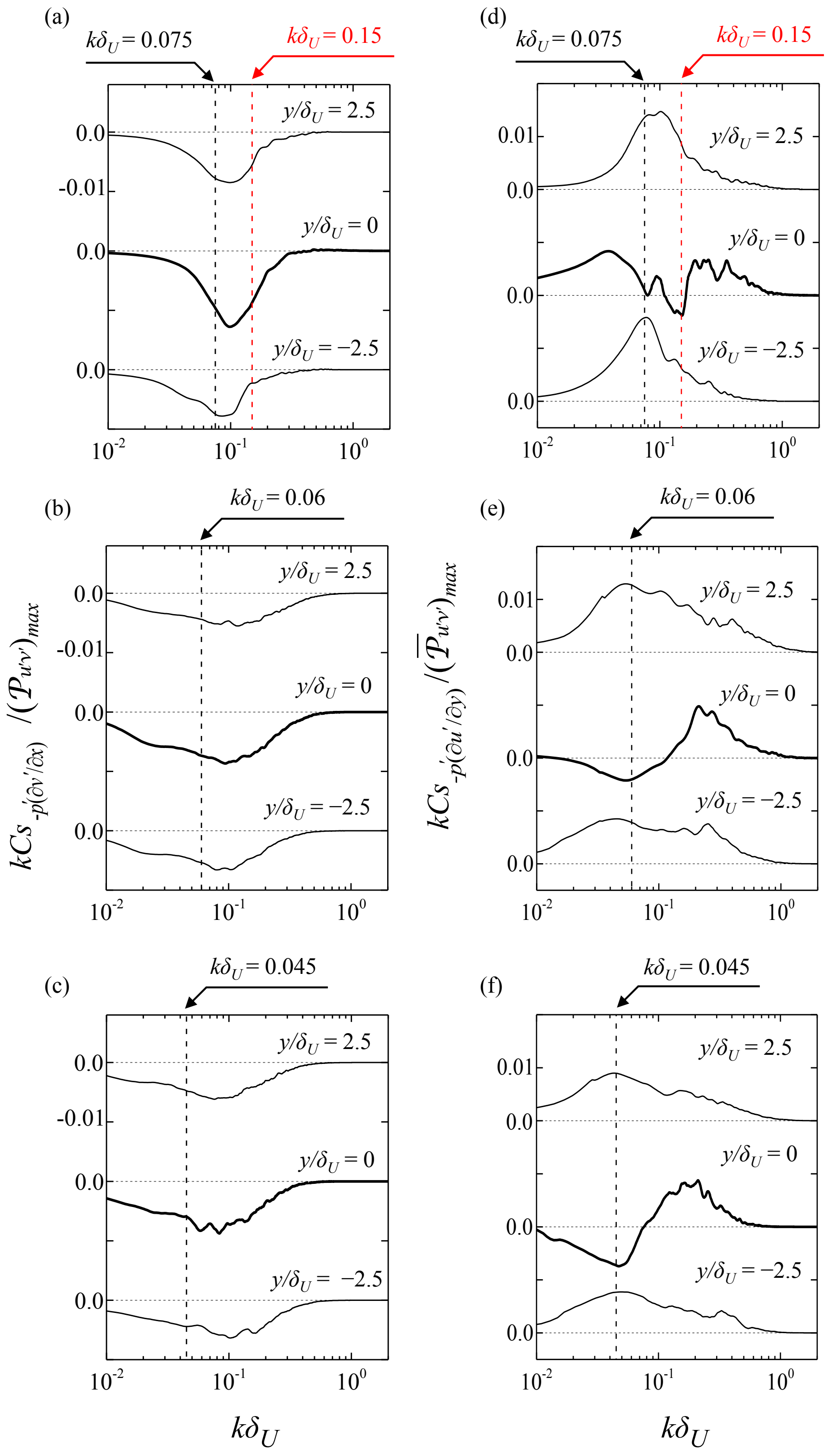

Figure 3.16: Co-spectra for (a–c) p' and $-\partial v'/\partial x$, and (d–f) p' and $-\partial u'/\partial y$ in the pressure-strain correlation term at (a,d) $x/L = 0.78$ ($x/\delta_{U0} = 160$), (b,e) $x/L = 1.38$ ($x/\delta_{U0} = 283$), and (c,f) $x/L = 1.95$ ($x/\delta_{U0} = 399$).

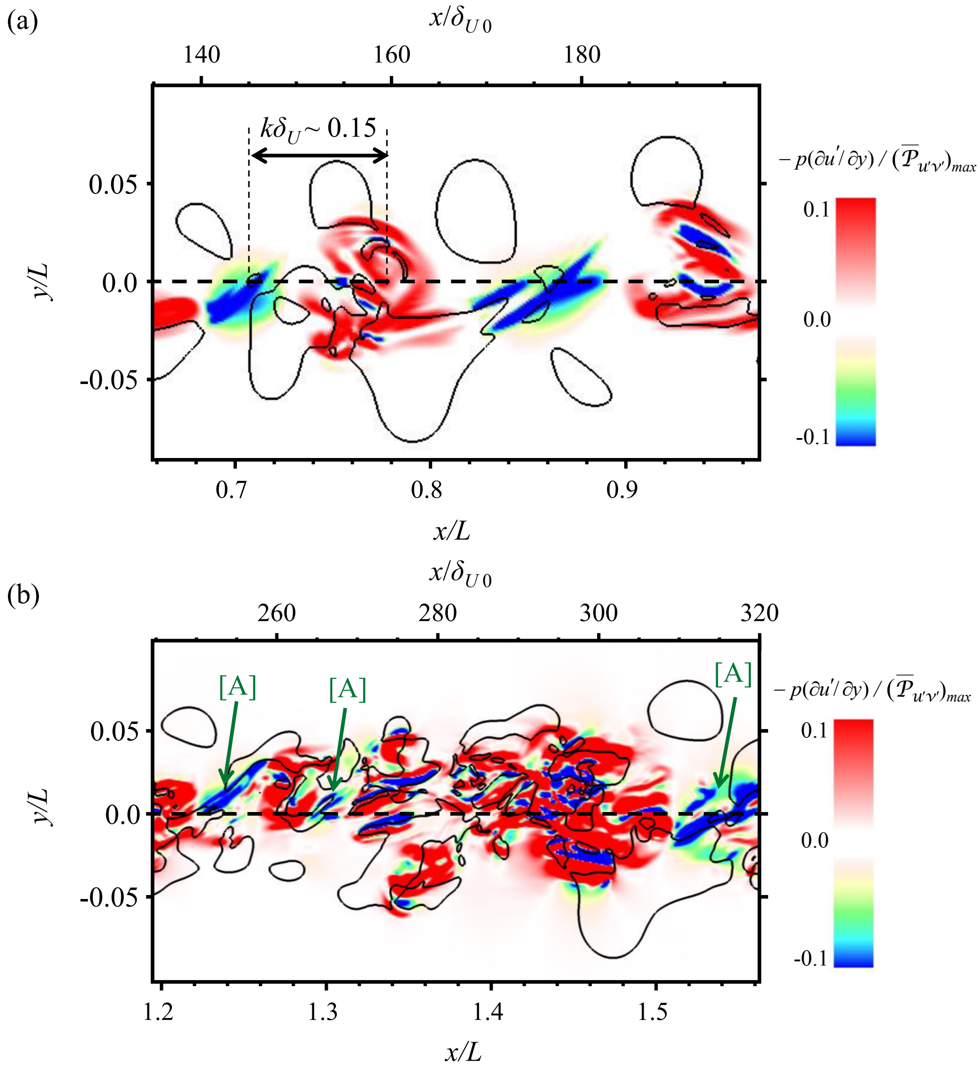

Figure 3.17: Color contour maps of $-p'(\partial u'/\partial y)/(\mathcal{P}_{u'v'})_{max}$ of the pressure-strain correlation term in the (a) upstream ($x/L = 0.7 - 0.9$) and (b) downstream ($x/L = 1.2 - 1.6$) regions. The area surrounded by the black line indicates the CGMT.

First, the turbulent diffusion term is examined. Figure 3.15 shows the normalized power spectra for the turbulent diffusion term. The power spectrum at $y/\delta_U = 0$ is larger than that at $y/\delta_U = \pm 2.5$ in the entire region. However, no peak is observed at either $k\delta_U \sim 0.075$ or 0.15. In addition, there is no significant difference in the spectral shape among the locations. Therefore, this term should not be the critical term of the CGMT at the specific wavenumbers bands. Next, we examine the pressure-strain correlation term. Since it consists of two terms, i.e., $-p'(\partial u'/\partial y)$ and $-p'(\partial v'/\partial x)$, we show their co-spectra individually. Figures 3.16 (a–c) are the co-spectra for p' and $\partial v'/\partial x$ and Figs. 3.16 (d–f) are those for p' and $\partial u'/\partial y$. The co-spectra for p' and $\partial v'/\partial x$ show the negative contribution in the entire region but no peak is observed at neither $k\delta_U = 0.15$ nor 0.075 at $x/L = 0.78$ ($x/\delta_{U0} = 160$). On the other hand, the co-spectra for p' and $\partial u'/\partial y$ show the negative contribution approximately at the wavenumbers of $k\delta_U \sim 0.075$ and 0.15 at the center ($y = 0$). This suggests that $-\overline{p'(\partial u'/\partial y)}$ is the critical parameter that characterizes the CGMT at the specific wavenumber bands. Moreover, the spectrum shapes of the co-spectra for p' and $\partial u'/\partial y$ at $x/L = 1.38$ and 1.95 ($x/\delta_{U0} = 283$ and 399) are similar to each other and different from those at $x/L = 0.78$ ($x/\delta_{U0} = 160$).

Similarly to the pressure diffusion term, we show the instantaneous color contour map of $-p'(\partial u'/\partial y)/\mathcal{P}_{max}$ in the pressure-strain correlation term in Fig. 3.17. In the upstream region (Fig. 3.17 (a)), the negative (blue) area appears not only in the stretching region but also in the vortical region where the positive area (red) dominates, and no visible relationship is found between the negative contribution of $-p'(\partial u'/\partial y)$ and CGMT. Therefore, the joint PDF for $-p'(\partial u'/\partial y)$ and the Reynolds shear stress are calculated in the same way as for the pressure diffusion term. Figure 3.18 shows the results without and with the phase shift. Note that the phase shift is done by the same method as in Fig. 3.14. Figure 3.18 (a) indicates that the two terms are dependent [46] even though it is not clear from the snapshot (Fig. 3.17 (a)). Figure 3.18 (b) shows a positive correlation between the two terms and the negative Reynolds shear stress (CGMT) appears more dominantly in the region where $-p'(\partial u'/\partial y)$ is negative. This can be the evidence of the CGMT and the relationship between the CGMT and negative $-p'(\partial u'/\partial y)$.

As the flow proceeds toward the downstream direction, the negative contribution in the coherent vortex begins to disperse while that in the stretching region remains intact (indicated by [A] in Fig. 3.17 (b)). This can

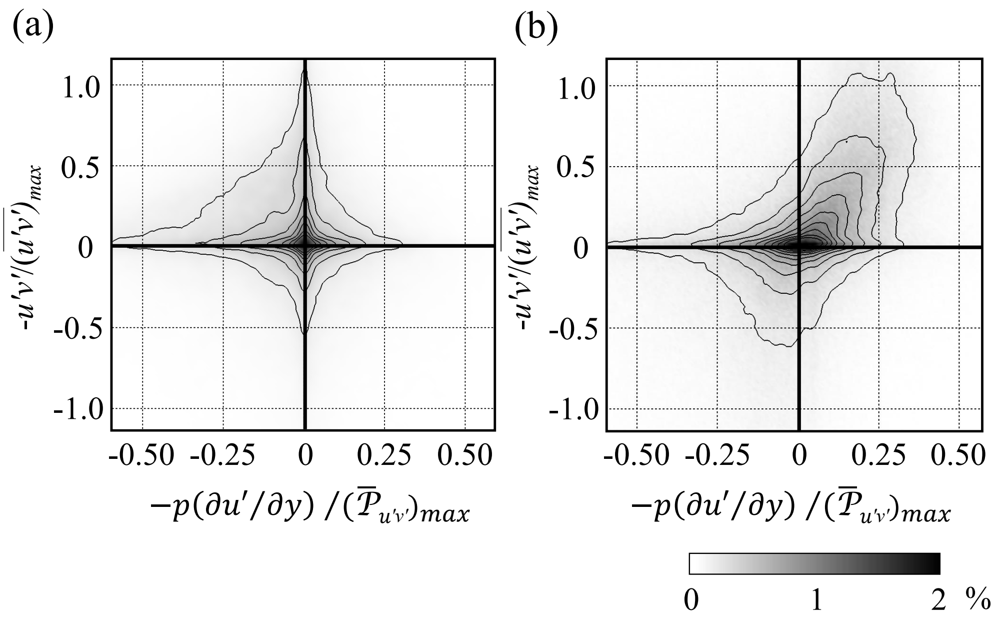

Figure 3.18: Joint PDFs of the Reynolds shear stress and $-p'(\partial u'/\partial y)$ of the pressure-strain correlation term at $x/L = 0.78$ and $y/\delta_U = 0$. (a) Without the phase shift; (b) with the phase shift.

be supported by the fact that the negative contribution in the co-spectrum for p' and $\partial u'/\partial y$ appears even in the downstream region ($x/L = 1.38$ and 1.95) as shown in Figs. 3.16(e) and (f). Moreover, the wavenumbers of $k\delta_U = 0.06$ (Fig. 3.16 (e)) and 0.045 (Fig. 3.16 (f)) correspond to the peak wavenumbers of the pressure fluctuation spectrum (Fig. 3.7). In addition, comparison of Figs. 3.6 (b) and 3.17 (b) indicates that the negative contribution of $-\overline{p'(\partial u'/\partial y)}$ ([A] in Fig. 3.17 (b)) appears at the locations where the large-scale positive pressure remains. Pressure is not necessarily synchronized with the velocity field. However, the CGMT in the present study occurs at medium-to-large scales in situations where the coherent flow structure remains. Therefore, there is a good match between them. On the contrary, since the dispersed negative contribution tends to appear continuously with an increasing streamwise distance, the negative part of the co-spectrum expands to the lower wavenumber side (Figs. 3.16 (e) and (f)).

3.5 Relationship between the CGMT and vorticity distribution

It is of great interest to clarify the relationship between the CGMT and the transition of the mixing layer from laminar to turbulence. The vorticity magnitude is known as a good indicator to distinguish the turbulent and non-turbulent regions in jets [82, 83, 84, 85, 86]. Thus, the same method can be applied in the present study.

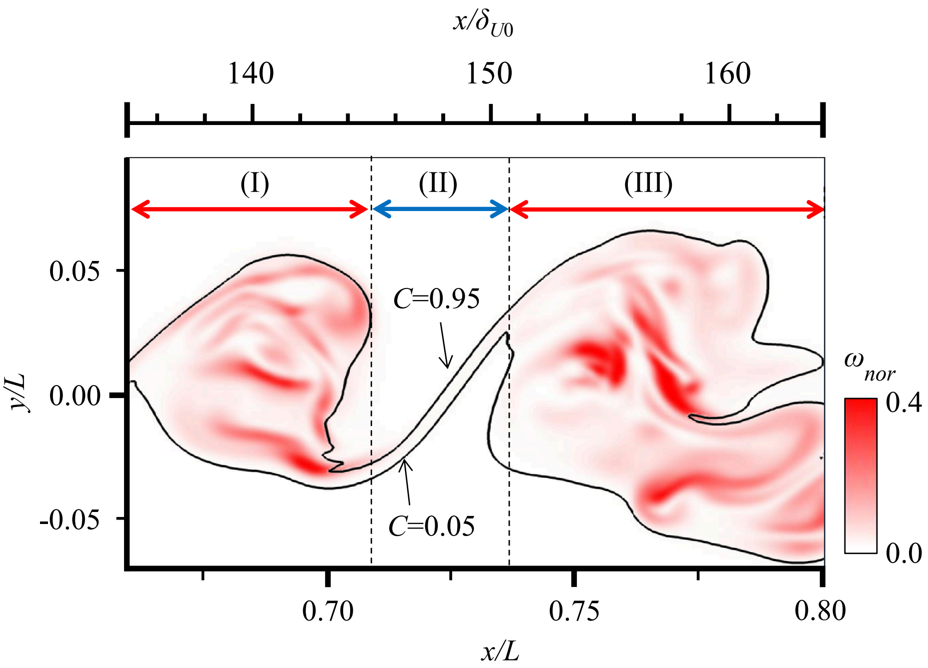

Figure 3.19: Instantaneous distribution of the vorticity magnitude for $0.66 \leq x/L \leq 0.80$. The upper and lower black lines indicate $C = 0.95$ and $C = 0.05$, respectively.

The vorticity magnitude normalized by ΔU and δ_U, $\omega_{nor} = |\boldsymbol{\omega}|/(\Delta U/\delta_U)$ has been used as the index to distinguish the turbulent and non-turbulent regions [53]. In this study, the area that satisfies $\omega_{nor} \geq \omega_T$ is regarded as the vortical region and the area that satisfies $\omega_{nor} < \omega_T$ is regarded as the non-turbulent region, where ω_T is the threshold value determined from the volume fraction of the turbulent region V in the specific area. Furthermore, Watanabe *et al.* [53] used $dV/d\omega_{nor}$ as the index function to determine ω_T; we employed this method as well. Figure 3.19 shows the instantaneous distribution of ω_{nor} in $0.66 < x/L < 0.80$, where the trend of CGMT can be observed. It is demonstrated that the vorticity magnitude is large in the coherent vortical region. Figure 3.20 shows the volume fraction of the normalized vorticity magnitude, V, and its derivative, $-dV/d\omega_{nor}$, as functions of ω_{nor} obtained from the entire domain in Fig. 3.19. It is not successful to determine the ω_T from this figure because there is no clear plateau in both lines. Thus, we divided the area into three regions (regions (I), (II), and (III)) because the flow characteristics in region (II) are different from those in regions (I) and (III). V and $dV/d\omega_{nor}$ as functions of ω_{nor},

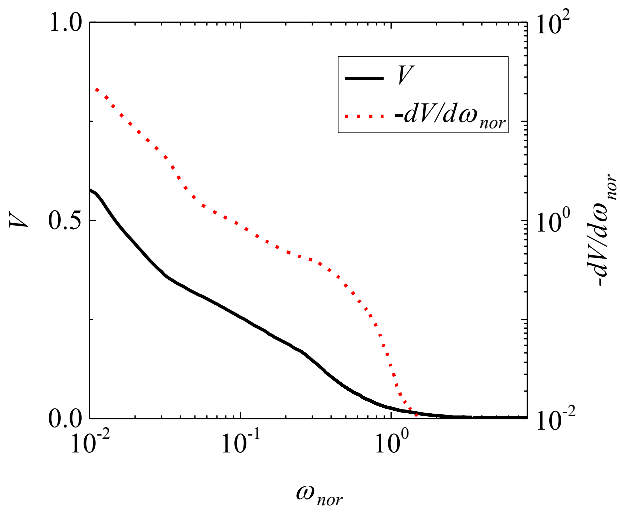

Figure 3.20: Volume fraction of the normalized vorticity magnitude, V, and $-dV/d\omega_{nor}$ as functions of the threshold ω_T examined for $0.66 \leq x/L \leq 0.80$.

in each region, are shown in Figs. 3.21 (a)–(c), respectively. Note that ω_T is determined at each location and each region. In the vortical regions ((I) and (III)), there is a nearly flat plateau for both V and $dV/d\omega_{nor}$, and 0.08 and 0.2 can be chosen as ω_T, respectively. Such a clear plateau is not seen in region (II). Thus, we will discuss only the vortical regions.

Figure 3.22 shows the instantaneous distributions of $-u'v'/\Delta U^2$ (color contour map) and the high-vorticity region for (a) $0.30 \leq x/L \leq 0.34$, (b) $0.55 \leq x/L \leq 0.61$, (c) $0.80 \leq x/L \leq 0.90$, and (d) $1.60 \leq x/L \leq 1.80$. The isopleth of $C = 0.05$ and $C = 0.95$ (gray lines) are also shown. The ω_T is set to 0.04, 0.07, 0.15, and 0.10 for Figs. 3.22 (a)–(d), respectively. Note that the same vortex is captured in a Lagrangian way in order to trace its development in these figures. The high-vorticity area is shaded in (a), (b), and (c). Since the majority of the flow is the high-vorticity region in Fig. 3.22 (d), it is not shaded and the dispersed small fragments represent the small-vorticity region. Additionally, Fig. 3.23 shows the velocity derivatives toward the streamwise direction at approximately the center of the same streamwise locations. In Fig. 3.22 (a), the overall shape of the vortex is oval and the high-vorticity region appears in the boundary between the GMT and CGMT in the upstream region. However, Fig. 3.23 (a) illustrates that the streamwise change of the velocity derivatives is mild

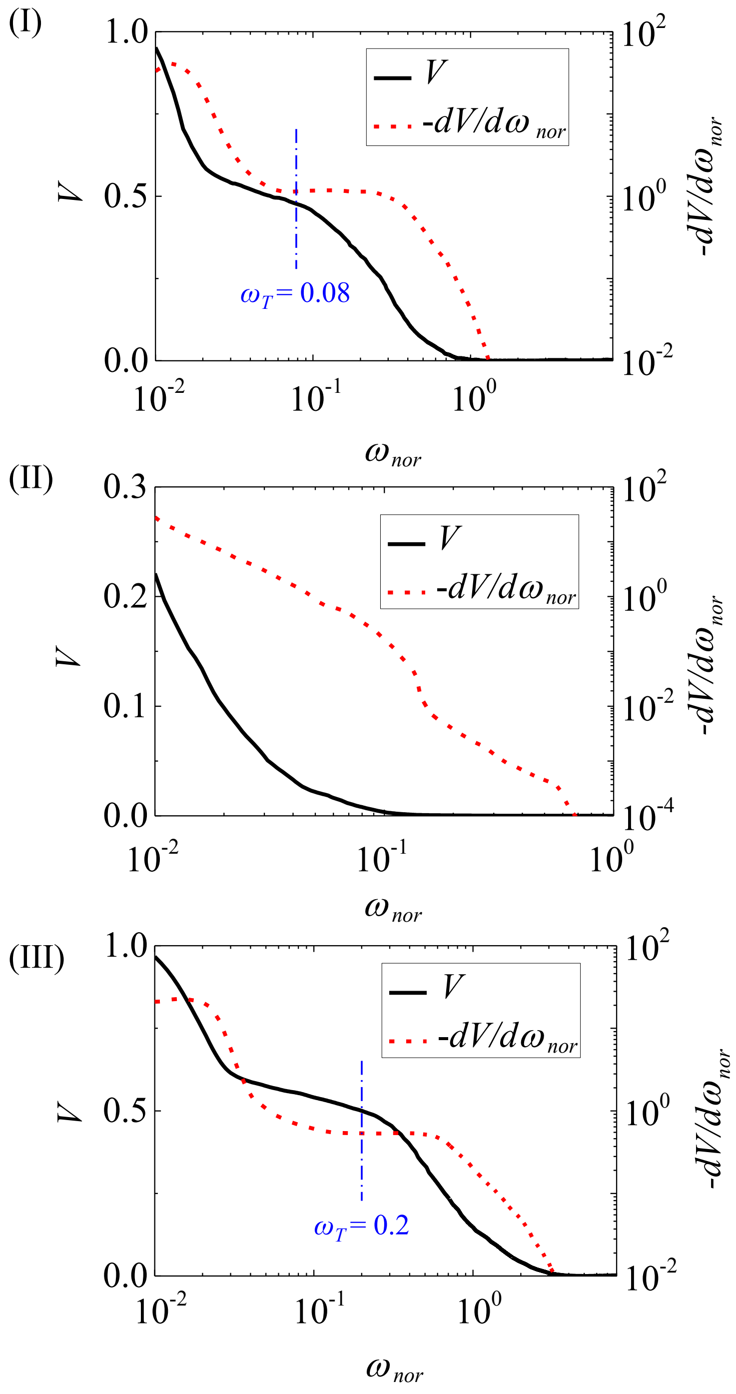

Figure 3.21: Volume fraction of the normalized vorticity magnitude, V, and $-dV/d\omega_{nor}$ as functions of ω_T. (I)–(III) correspond to those in Fig. 3.19.

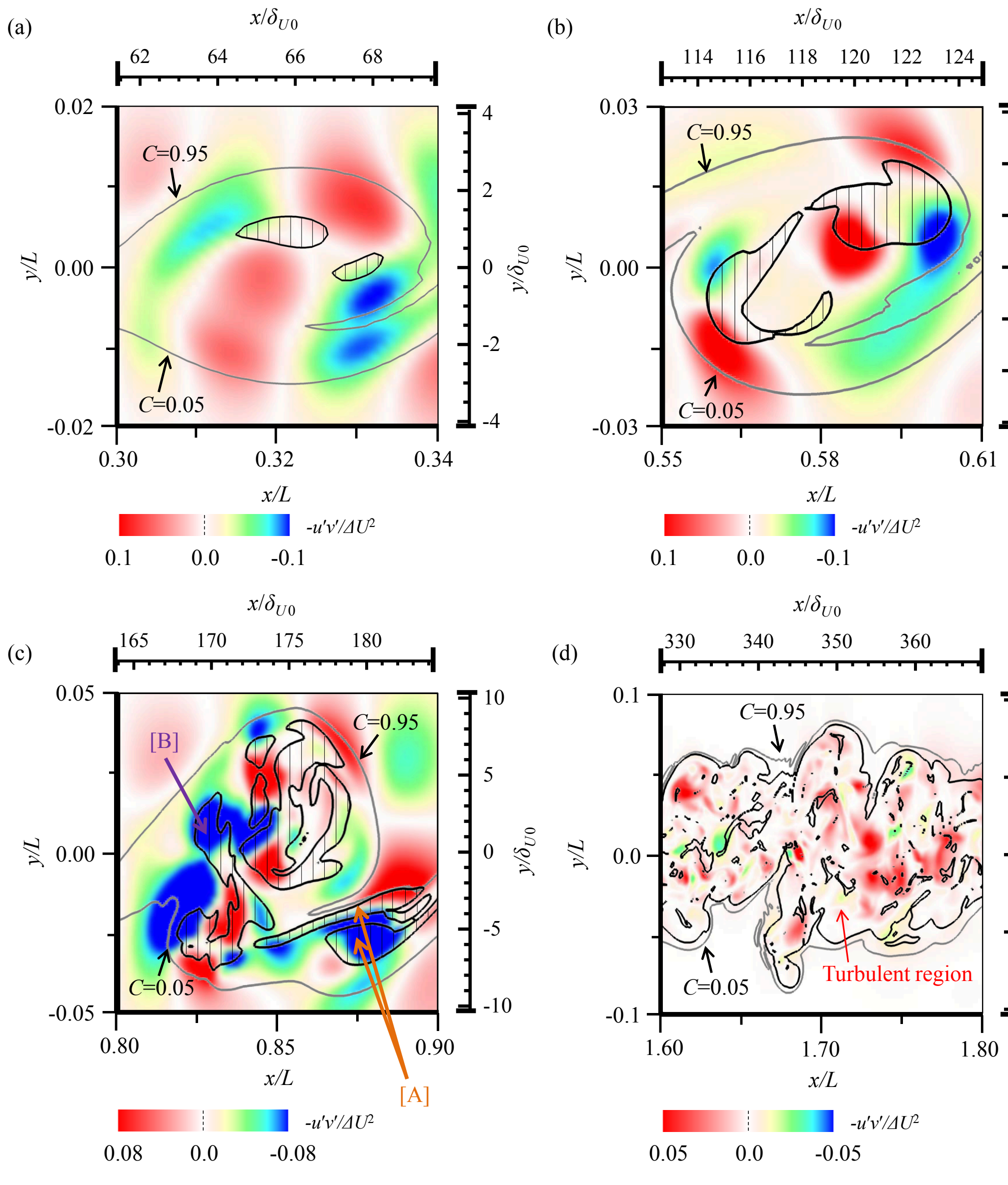

Figure 3.22: Instantaneous distributions of $-u'v'/\Delta U^2$ (color contour map) and the high-vorticity region (shaded) for (a) $0.30 \leq x/L \leq 0.34$, (b) $0.55 \leq x/L \leq 0.61$, (c) $0.80 \leq x/L \leq 0.90$, (d) $1.60 \leq x/L \leq 1.80$.

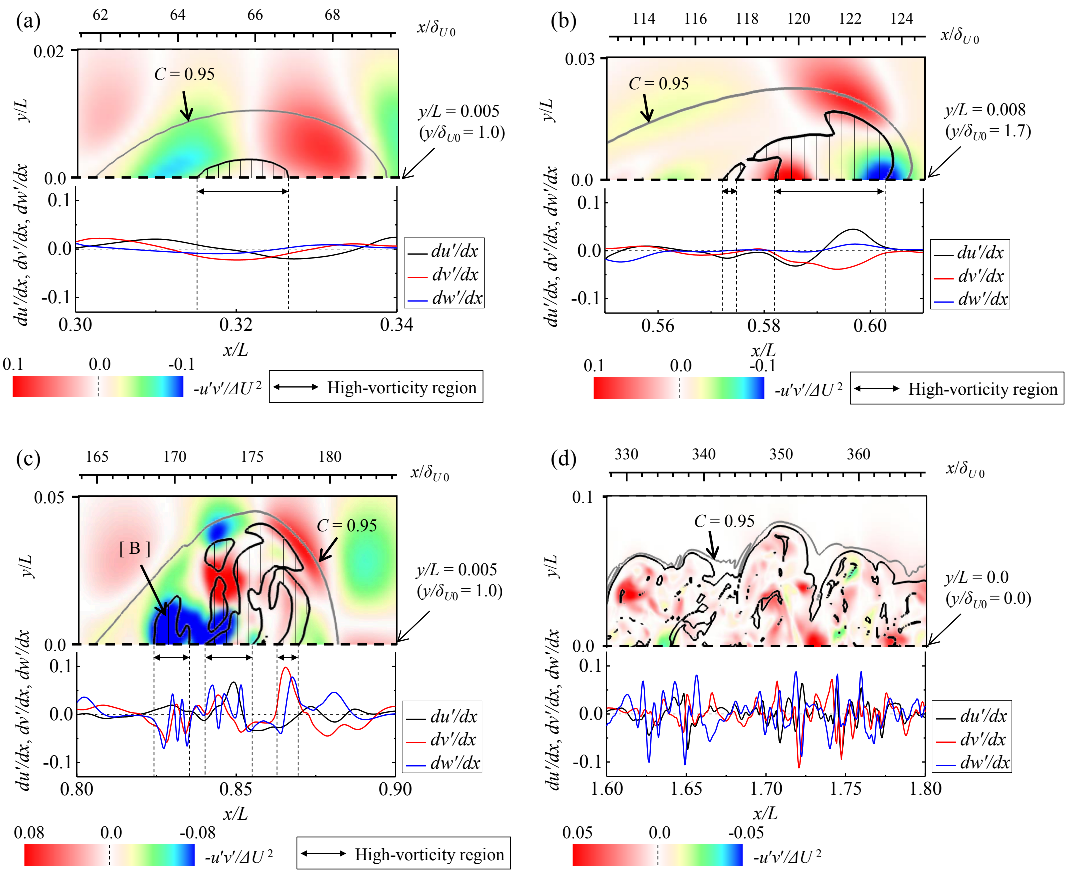

Figure 3.23: Streamwise distributions of the velocity derivatives toward the streamwise direction for (a) $0.30 \leq x/L \leq 0.34$ at $y/L = 0.005$ $(y/\delta_{U0} = 1.0)$, (b) $0.55 \leq x/L \leq 0.61$ at $y/L = 0.008$ $(y/\delta_{U0} = 1.7)$, (c) $0.80 \leq x/L \leq 0.90$ at $y/L = 0.005$ $(y/\delta_{U0} = 1.0)$, (d) $1.60 \leq x/L \leq 1.80$ at $y/L = 0.0$ $(y/\delta_{U0} = 0.0)$.

even in the high-vorticity regions, and the flow is far from turbulent. This fact coincides with the perception in prior studies [38, 39], in which only laminar (non-turbulent) flow is supposed to show the generation of the loss of the Reynolds stress. The high-vorticity region gradually spreads, flowing toward the downstream direction, although it still consists of large lumps and is limited in the boundary area (Fig. 3.22 (b)). Besides, the streamwise change of the velocity derivatives in the high-vorticity area is still relatively mild (Fig. 3.23 (b)).

At the following streamwise location (Fig. 3.22 (c)), where the trend of CGMT was observed, the overall vortical shape is deformed and the high-vorticity region is fragmented and stretched. In addition, the vortex drags and merges the high-vorticity region with the forehead stretching region (indicated by A). Even at this moment, part of the high-vorticity region is transported toward the counter-gradient direction, as indicated by B. Moreover, unlike Figs. 3.23(a) and (b), the streamwise change of the velocity derivatives (especially dw'/dx) is significant and the amplitude is large in the high-vorticity region (indicated by B) (Fig. 3.23 (c)). In view of this, we can say that the trend generating the loss of the Reynolds stress appears in the flow where the turbulent and non-turbulent regions mix. After repeating the merge, while deforming the shape, the flow becomes nearly a fully-developed mixing layer, where the non-turbulent region and CGMT scarcely appear (Figs. 3.22 (d) and 3.23 (d)). In other words, the non-turbulent region and the CGMT almost simultaneously disappear.

3.6 Conclusions

The driving mechanism and vortical structure of the partial CGMT, appearing in the quasi self-similar region in shear mixing layer, were investigated by a direct numerical simulation. The main conclusions of this chapter are summarized as follows. The self-similarity between the velocity fluctuations and the Reynolds shear stress are demonstrated in $x/L \geq 0.67$ ($x/\delta_{U0} \geq 137$). However, the trend of CGMT is observed at around $k\delta_U = 0.075$ and 0.15 at $x/L = 0.78$ ($x/\delta_{U0} = 160$), and $k\delta_U = 0.075$ corresponds to the distance between the vortical/stretching regions of the coherent structure. The budget analysis for the Reynolds shear stress revealed that it is caused by the pressure diffusion term at the off-central region and by $-\overline{p(\partial u'/\partial y)}$ in the pressure-strain correlation term at the central region. As the flow moves toward the downstream direction, the appearance of those terms becomes random and the trend of CGMT at the specific wavenumber bands disappear. Furthermore, we investigated the relationship between the CGMT and vorticity distribution in the vortex region of the mixing layer, in association with the spatial development. In the upstream region, the high-vorticity region appears in the boundary between the areas of the GMT and CGMT. The area generating the loss of the Reynolds shear stress gradually spreads by flowing toward the downstream direction, and subsequently, the fluid mass with high-vorticity is transported from the forehead stretching region toward the counter-gradient direction. In this location, the velocity fluctuation in the high-vorticity region is large and turbulence is actively produced. In view of this, the trend generating the loss of the Reynolds shear stress appears in the flow where the vortical and non-turbulent regions mix. Then, the non-turbulent region and CGMT almost simultaneously disappear in the fully-developed region.

Chapter 4

Characteristics of turbulent Prandtl number

4.1 Introduction

The knowledge for the similarity between the momentum and scalar transfer helps to construct the turbulent scalar flux model [87, 88]. Verification of the similarity between the momentum and scalar transfer in turbulent shear flow is often done using turbulence Prandtl number Pr_T defined by the ratio of the eddy diffusivity coefficient v_T and turbulent scalar diffusivity coefficient α_T (i.e., $Pt_T = v_T/\alpha_T$). Since the governing equations for the velocity and scalar are similar, it is expected that turbulent characteristics between the momentum and scalar transfer in the turbulence field are also similar. Therefore, the assumption defined as $Pr_T = const.$, assuming the similarity between the momentum and scalar transfer, have been proposed for modeling the turbulent scalar fluxes based on Reynolds stresses [87, 88, 89, 90].

On the other hand, it has the dissimilarity between the momentum and scalar transfer in various shear turbulent flows [42, 91, 92] such as axisymmetric turbulent jet [93], channel flow [94, 95, 96, 97], (perturbed) turbulent boundary layer [98, 99, 100, 101], turbulent mixing layer [44], perturbed turbulent flow [102, 103], and Couette flow [95]. In these shear flows, Pr_T takes various values between 0.5 and 1.0.

The influence of turbulence field on Pr_T has been investigated so far. Fiedler [104, 105] investigated the relationship between the momentum and heat transfer in two-dimensional turbulence mixing layer where the large-scale vortex is dominant. As the results, they showed that heat is transported more actively than momentum by a large-scale vortical motion. Chambers *et al.* [44] focused on the relationship between large-scale structure and Pr_T. They showed that when the turbulent field is dominated by the large-scale structure, Pr_T takes a smaller value than that of the general turbulence field ($Pr_T = 0.5 - 1.0$). It can be said that the results of Chambers *et al.* are reasonable because the large-scale structure greatly changes depending on the type of shear turbulence flow and the initial conditions. However, it is not sufficiently mentioned what dynamical motion of the large-scale structure is causing their dissimilarities.

In this chapter, we investigate the relationship between the large-scale structure and Pr_T. Shear mixing layer is a suitable flow to investigate the relationship between them since the clear large-scale structure induced by the Kelvin-Helmholtz instability remains until far downstream. This study aims to clarify the influence of the large-scale structure on Pr_T. Note that the calculation conditions in this chapter are the same as those in Chapter 3.

4.2 Results and discussion

To confirm the self-similarity, vertical distributions of the mean streamwise velocity and concentration are shown in Figs. 4.1(a) and 4.1(b). From $x/L = 0.78$ ($x/\delta_{U0} = 160$), both mean velocity and concentration distributions almost collapse. Vertical distributions of the Reynolds shear stress, $-\overline{u'v'}$, and vertical scalar flux, $-\overline{v'c'}$, are also shown in Figs. 4.2(a) and 4.2(b). Here, $-\overline{u'v'}$ and $-\overline{v'c'}$ are normalized by $(\Delta U)^2$ and $\Delta U \Delta C$, respectively. Both statistics collapse from $x/L = 1.38$ ($x/\delta_{U0} = 283$). Thus, the mixing layer is self-preserved downstream of $x/L = 1.38$ ($x/\delta_{U0} = 283$).

To discuss the similarity of the momentum and scalar transfer, Pr_T is calculated by the following equation:

$$Pr_T = \frac{v_T}{\alpha_T} = \frac{-\overline{u'v'}/(d\overline{U}/dy)}{-\overline{v'c'}/(d\overline{C}/dy)}. \tag{4.1}$$

Here, α_T and v_T are the turbulent scalar diffusivity coefficient and eddy diffusivity coefficient, respectively. Figure 4.3 shows the streamwise distributions of Pr_T, α_T, and v_T. Pr_T changes toward the downstream direction up to about $x/L < 1.4$, and in the further downstream region, Pr_T takes a

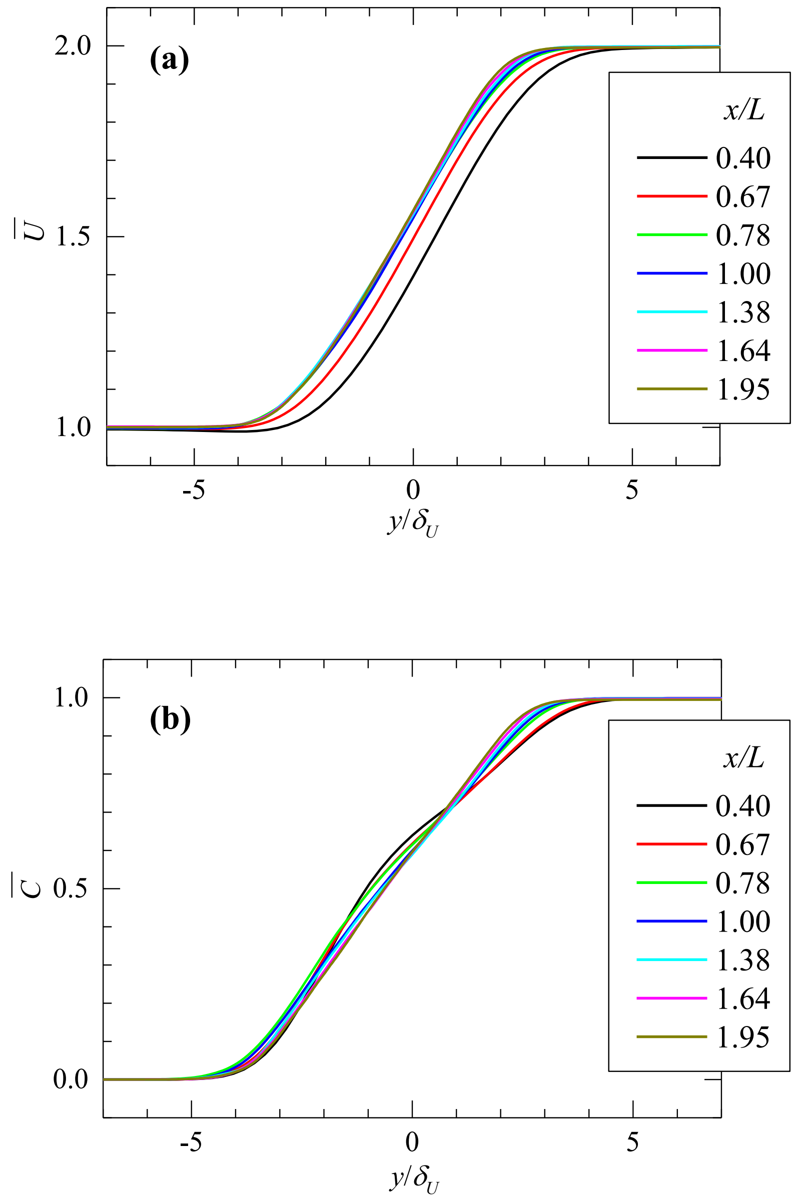

Figure 4.1: Vertical distributions of the (a) mean streamwise velocity, (b) mean concentration.

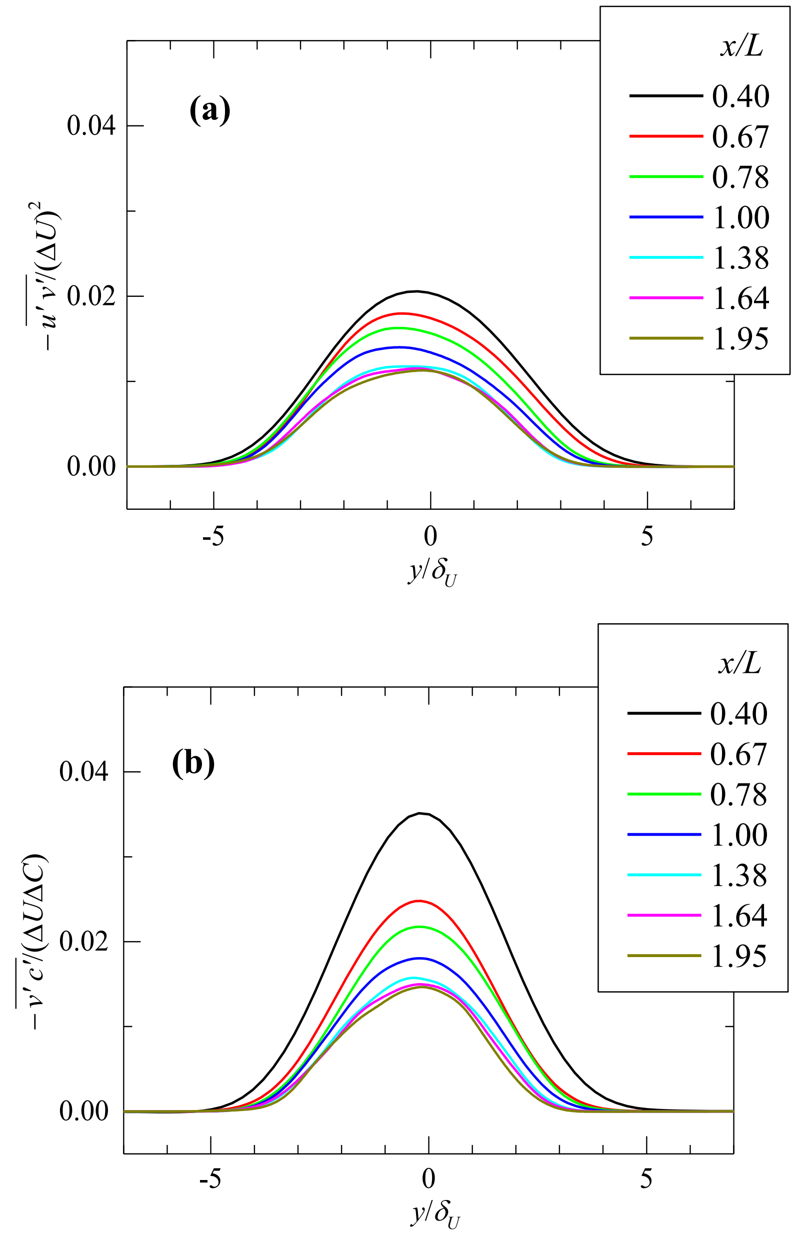

Figure 4.2: Vertical distributions of the (a) Reynolds shear stress for $-\overline{u'v'}$, and (b) vertical scalar flux for $-\overline{v'c'}$.

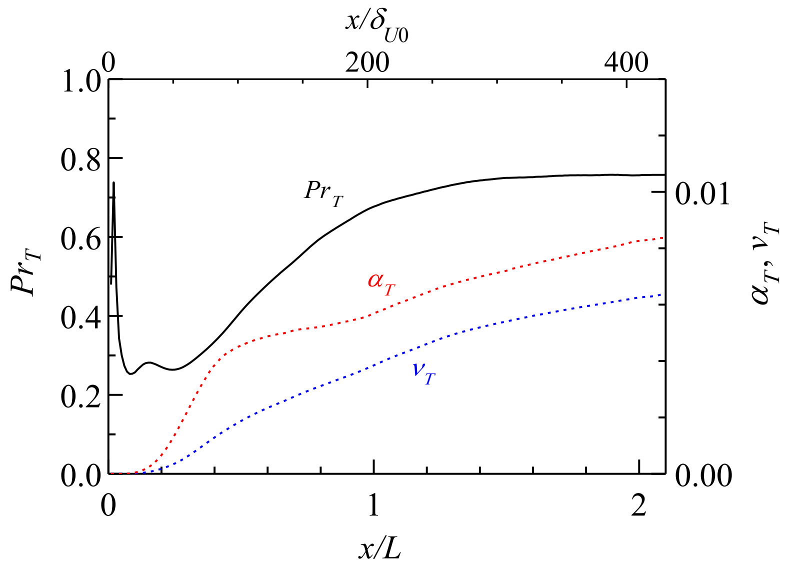

Figure 4.3: Streamwise distributions of the Pr_T, υ_T, and α_T at the center ($y = 0$).

constant value of $Pr_T = 0.78$. It is known that, Pr_T takes a value from 0.5 to 1.0 in various turbulence fields for fully-developed turbulence [42,91], so the result of this simulation is plausible. To investigate in more detail, we show υ_T and α_T. There is no big difference in the trend of υ_T and α_T. Hence, we also investigate in furthermore detail, $d\overline{U}/dy$, $d\overline{C}/dy$, and $(d\overline{U}/dy)/(d\overline{C}/dy)$ in Fig. 4.4(a) and $-\overline{u'v'}$, $-\overline{v'c'}$, and $\overline{u'v'}/\overline{v'c'}$ in Fig. 4.4(b), respectively. In Fig. 4.4(a), $d\overline{U}/dy$ and $d\overline{C}/dy$ take a peak approximately at $x/L = 0.1$ and these values decrease with increaseing the streamwise distance. At this time, the streamwise distribution of $(d\overline{U}/dy)/(d\overline{C}/dy)$ become a constant approximately at $x/L \geq 1.4$. In Fig. 4.4(b), $-\overline{u'v'}$ and $-\overline{v'c'}$ take a peak approximately at $x/L = 0.4$ and decrease with increaseing the streamwise distance. At this time, $\overline{u'v'}/\overline{v'c'}$ also become a constant approximately at $x/L \geq 1.4$. From the above, it reveals that when Pr_T is changing toward the downstream direction, both $(d\overline{U}/dy)/(d\overline{C}/dy)$ and $\overline{u'v'}/\overline{v'c'}$ also change, and when Pr_T takes a constant value, both of them also take a constant value.

Figures 4.5 and 4.6 show the joint probability density function (JPDF) of u' and v' and JPDF of c' and v', respectively. Here, u', v', and c' are normalized by the root mean square values of themselves (indicated by $\overline{u'}$,

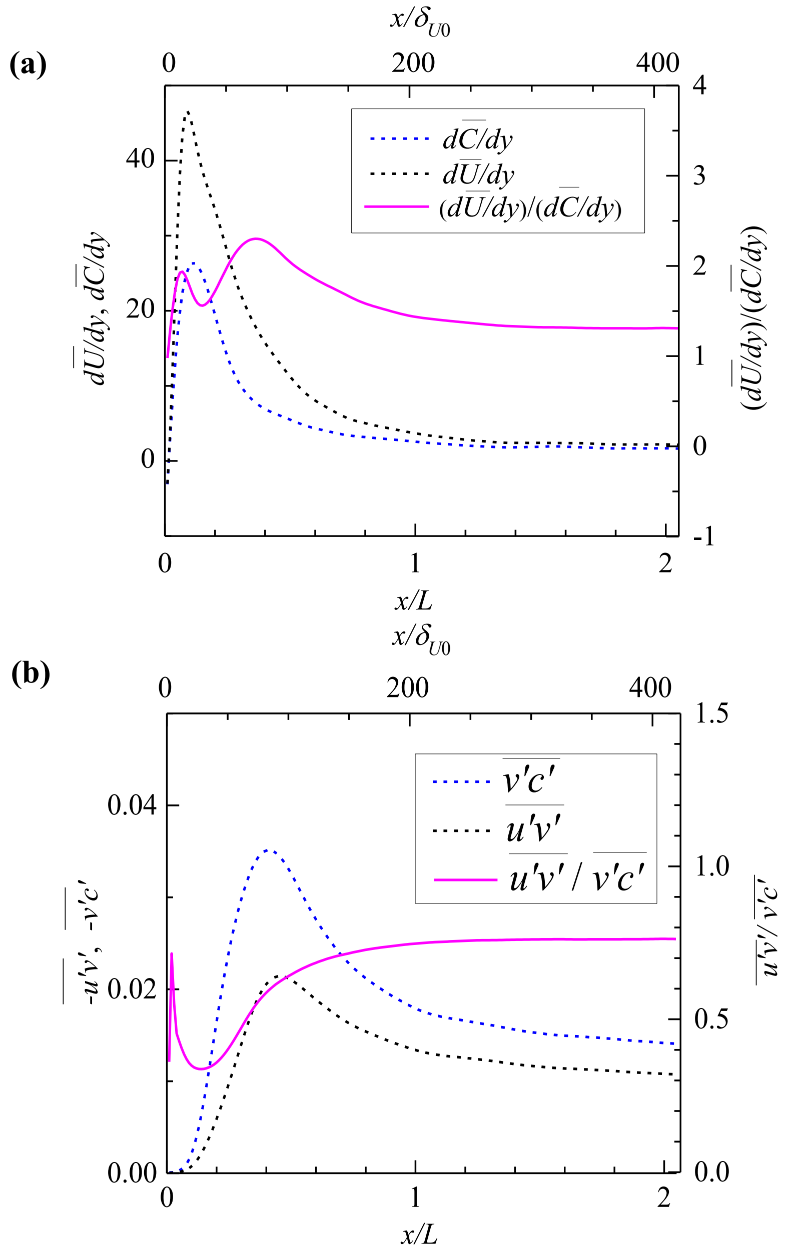

Figure 4.4: Streamwise distributions of the (a) $d\overline{U}/dy$, $d\overline{C}/dy$, and $(d\overline{U}/dy)/(d\overline{C}/dy)$, and (b) $-\overline{u'v'}$, $-\overline{v'c'}$, and $\overline{u'v'}/\overline{v'c'}$ at the center ($y = 0$).

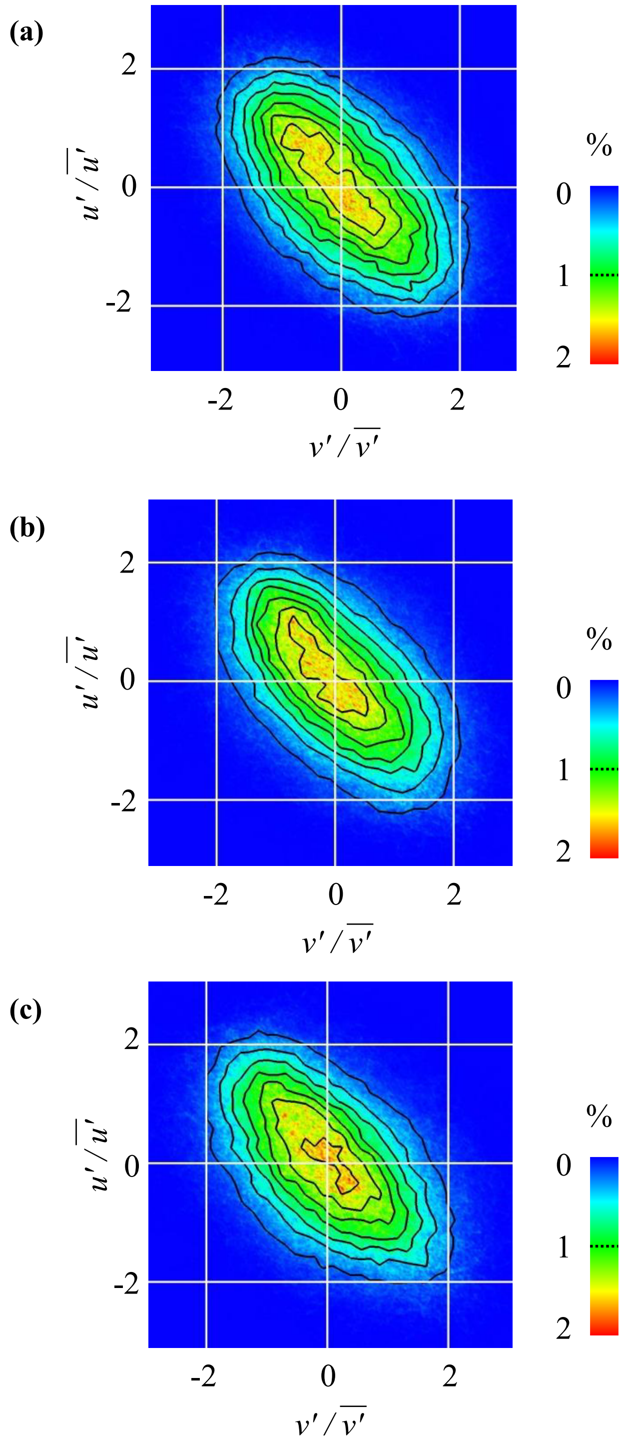

Figure 4.5: Joint probability density functions of u' and v' at (a) $x/L = 0.78$ ($x/\delta_{U0} = 160$), (b) $x/L = 1.38$ ($x/\delta_{U0} = 283$), and (c) $x/L = 1.95$ ($x/\delta_{U0} = 400$) at the center ($y = 0$).

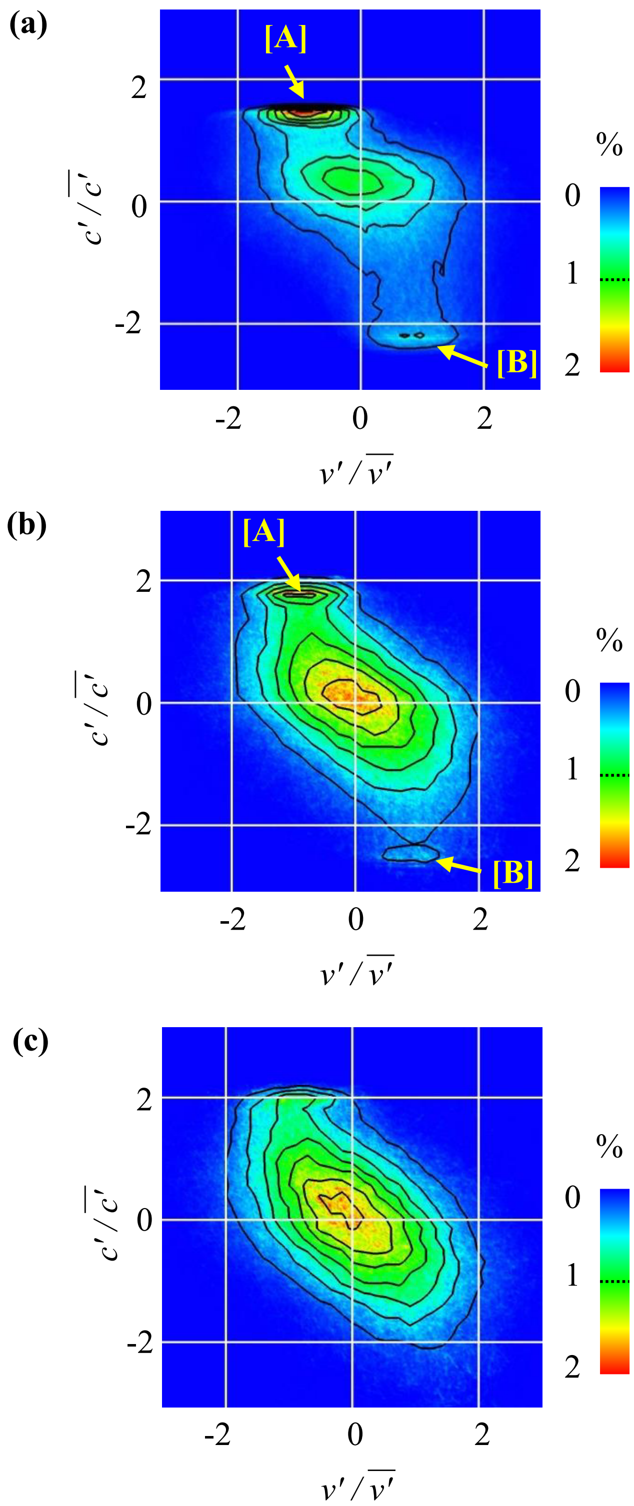

Figure 4.6: Joint probability density functions of c' and v' at (a) $x/L = 0.78$ ($x/\delta_{U0} = 160$), (b) $x/L = 1.38$ ($x/\delta_{U0} = 283$), and (c) $x/L = 1.95$ ($x/\delta_{U0} = 400$) at the center ($y = 0$).

$\overline{v'}$, and $\overline{c'}$, respectively). In Figs. 4.5(a)–(c), JPDFs of u' and v' take a negative correlation and a similar distribution at each downstream location (x/L = 0.78, 1.38, and 1.95). In Figs. 4.6(a)–(c), JPDFs of c' and v' also show a tendency of negative correlation similar to Figs. 4.5, but these JPDFs are much different from JPDFs of u' and v' on the upstream region because of existences of the scalar of $C = 0$ and 1 in the concentration field. The influence of the scalar of $C = 0$ and 1 in the concentration field appears as [A] and [B] in the Figs. 4.6(a) and 4.6(b). The difference between JPDF of u' and v' and JPDF of c' and v' becomes small at downstream region (at $x/L = 1.95$).

To support the above remarks, we show the contour maps of the instantaneous concentration and streamwise velocity in Figs. 4.7 and Figs. 4.8. Here, the blue and red areas in Figs. 4.7(a) and 4.8(a) indicate the value of $C = 0.0$ and $C = 1.0$, respectively. In the same way, the blue and red ares in Figs. 4.7(b) and 4.8(b) indicate the value of $U \leq 1.0$ and $U \geq 2.0$, respectively. In the upstream region (Figs. 4.7(a) and 4.7(b)), the scalar of $C = 0.0$ and 1.0 pass through the center of the mixing layer (on the broken line) and these events correspond to the dominated regions indicated by [A] and [B] in the Fig. 4.6(a). However, the instantaneous streamwise velocity field (Fig. 4.7(b)) is leveled according to the averaged streamwise velocity gradient. This means that the flow originally in the upper stream is deaccelerated strongly and transported to the lower region, and the flow originally in the lower stream is accelerated and transported to the upper region. In the downstream region (Figs. 4.8(a) and 4.8(b)), the scalar of $C = 1.0$ in the instantaneous concentration is still carried slightly to the center, and the instantaneous streamwise velocity of the flow (Fig. 4.8(b)) is further leveled than on the upstream region (Fig. 4.7(b)).

To clarify the scale contributing to the disagreement between the momentum and scalar transfer, the co-spectra for u' and v' and co-spectra for c' and v' are calculated. The results are shown in Figs. 4.9(a)–(c). Here, wavenumber k is normalized by the momentum thickness. In the upstream region ($x/L = 0.78$), the co-spectrum for u' and v' is a clear trend of the downward convex approximately at $k\delta_U = 0.075$ and 0.15. In chapter 3 (Fig. 3.8), it had already been clarified that the downward convex of the co-spectrum is caused by momentum transfer of the counter-gradient direction due to the dynamical motion of the large-scale structure. Furthermore, the co-spectra for c' and v' have a sharp spectral peak and the height of the

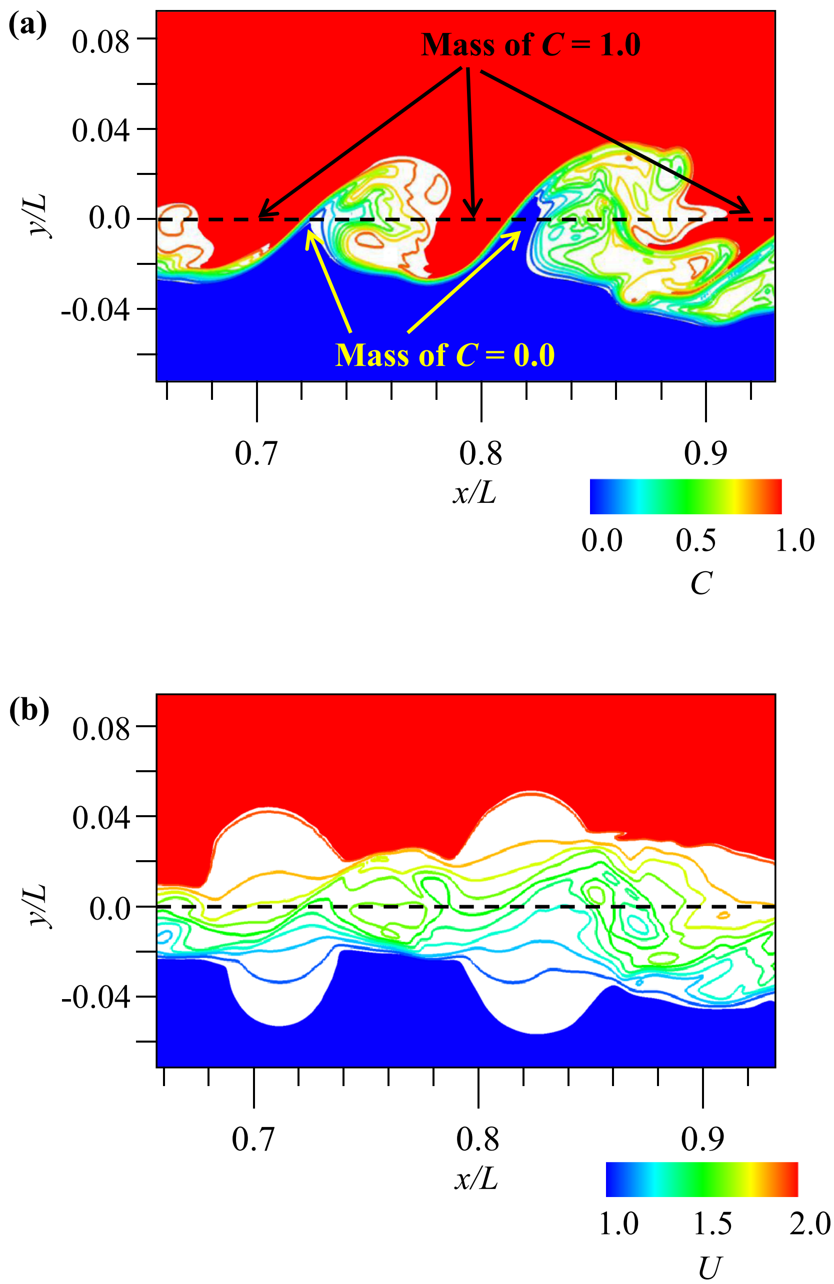

Figure 4.7: The instantaneous contour map of the (a) concentration and (b) streamwise velocity in $0.7 \leq x/L \leq 0.9$ at the same time. The blue and red regions in Fig. 4.7(a) indicate the value of $C = 0.0$ and $C = 1.0$, respectively, and the blue and red regions in Fig. 4.7(b) indicate the value of $U \leq 1.0$ and $U \geq 2.0$, respectively.

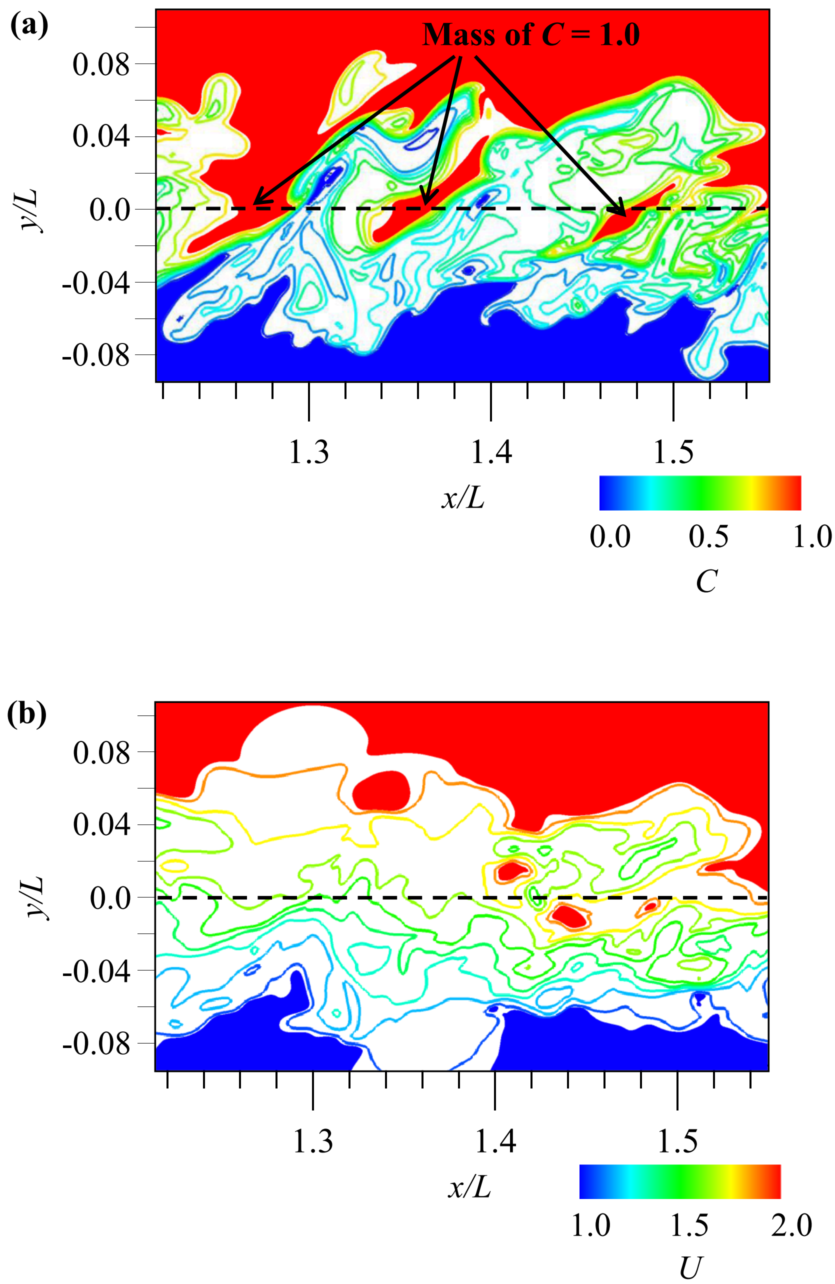

Figure 4.8: The instantaneous contour map of the (a) concentration and (b) streamwise velocity in $1.2 \leq x/L \leq 1.5$ at the same time. The blue and red regions in Fig. 4.8(a) indicate the value of $C = 0.0$ and $C = 1.0$, respectively, and the blue and red regions in Fig. 4.8(b) indicate the value of $U \leq 1.0$ and $U \geq 2.0$, respectively.

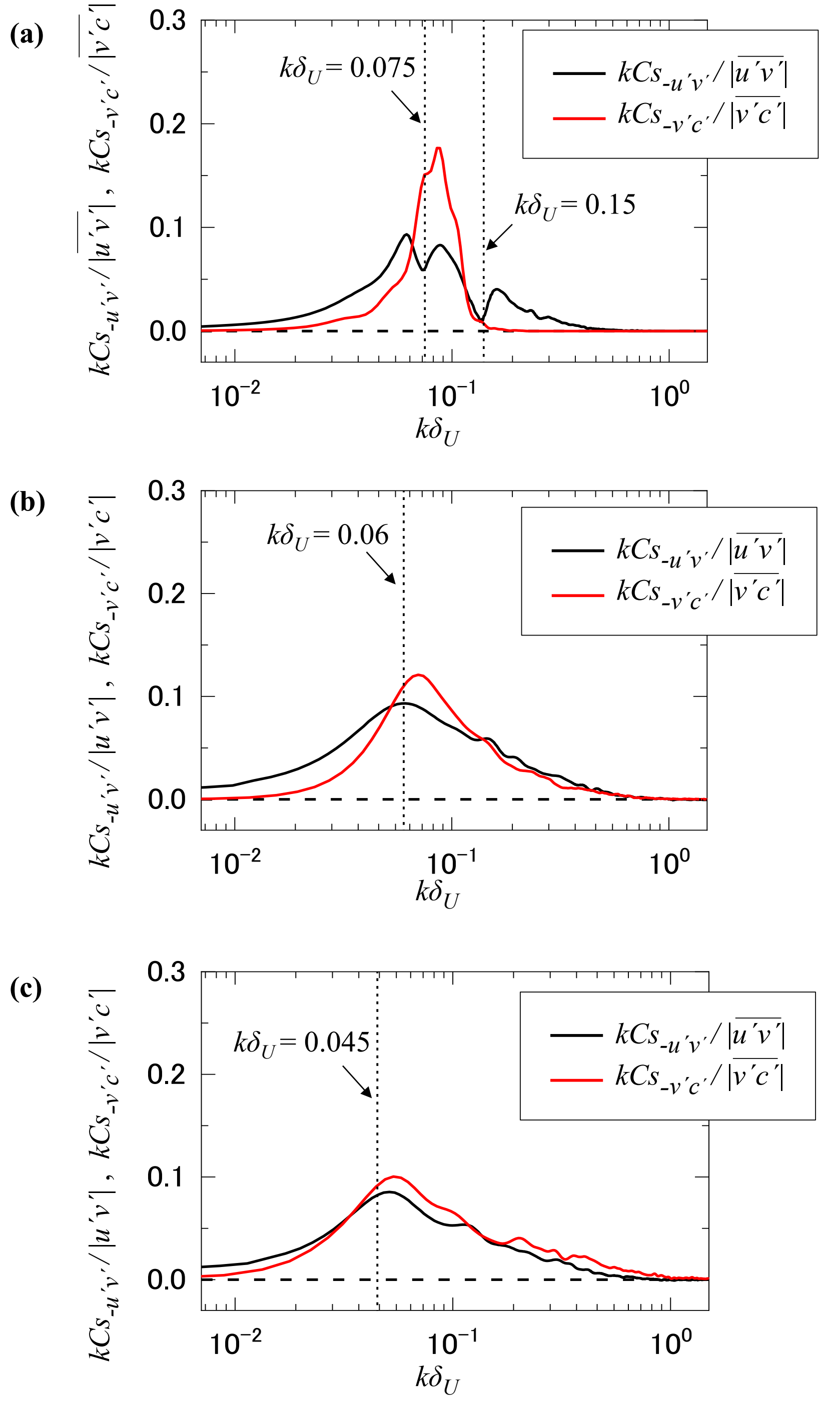

Figure 4.9: Co-spectra for the Reynolds shear stress (u' and v') and scalar flux (v' and c') at (a) $x/L = 0.78$ ($x/\delta_{U0} = 160$), (b) $x/L = 1.38$ ($x/\delta_{U0} = 283$), and (c) $x/L = 1.95$ ($x/\delta_{U0} = 400$).

spectral peak is very high compared to that of the co-spectrum for u' and v'. This similar tendency of the co-spectra is also observed in the turbulent mixing layer with the dynamical motion of the large-scale structure by Chambers et al [44]. They measured Pr_T and obtained the value of Pr_T of about $Pr_T = 0.4$, which is somewhat smaller than the result of the present study ($Pr_T = 0.55$) at $x/L = 0.78$. However, in the present study, it should also be noted that the value of Pr_T in upstream region changes toward the downstream direction, and smaller Pr_T is seen in the further upstream side of $x/L = 0.78$. It is also revealed that the disagreement between the momentum and scalar transfer is occurred by the scale corresponding to the large-scale structure because the spectral peak of the co-spectra corresponds to the average frequency of appearance of the large-scale structure [44, ?]. As the flow goes toward downstream, the width of the sharp spectral peak of the cospectra for c' and v' becomes broader. In the most downstream region ($x/L = 1.95$), co-spectra for u' and v' and co-spectra for c' and v' are almost collapse.

Table 4.1: Terms of momentum transfer equation and scalar transfer equation.

Term	Momentum transport equation	Scalar transport equation
Convection term	$\overline{\mathcal{C}}_{u'v'} = \overline{U_k}\frac{\partial}{\partial x_k}\overline{u'v'}$	$\overline{\mathcal{C}}_{v'c'} = \overline{U_k}\frac{\partial}{\partial x_k}\overline{v'c'}$
Production term	$\overline{\mathcal{P}}_{u'v'} = \left\{\overline{v'u'_k}\frac{\partial \overline{U}}{\partial x_k} + \overline{u'u'_k}\frac{\partial \overline{V}}{\partial x_k}\right\}$	$\overline{\mathcal{P}}_{v'c'} = \left\{\overline{u'_k c'}\frac{\partial \overline{V}}{\partial x_k} + \overline{v'u'_k}\frac{\partial \overline{C}}{\partial x_k}\right\}$
Dissipation term	$\overline{\epsilon}_{u'v'} = \frac{2}{Re}\left\{\overline{\left(\frac{\partial u'}{\partial x_k}\right)\left(\frac{\partial v'}{\partial x_k}\right)}\right\}$	$\overline{\epsilon}_{v'c'} = \left(\frac{1}{Re} + \frac{1}{ReSc}\right)\left\{\overline{\left(\frac{\partial v'}{\partial x_k}\right)\left(\frac{\partial c'}{\partial x_k}\right)}\right\}$
Pressure-strain correlation term	$\overline{\Pi}_{u'v'} = -\overline{p'\left(\frac{\partial u'}{\partial y} + \frac{\partial v'}{\partial x}\right)}$	
Pressure-scalar gradient correlation term		$\overline{\Pi}_{v'c'} = -\overline{p'\left(\frac{\partial c'}{\partial y}\right)}$
Turbulent diffusion term	$\overline{\mathcal{D}^{\mathcal{T}}}_{u'v'} = \frac{\partial}{\partial x_k}\overline{u'v'u'_k}$	$\overline{\mathcal{D}^{\mathcal{T}}}_{v'c'} = \frac{\partial}{\partial x_k}\overline{v'u'_k c'}$
Viscous diffusion term	$\overline{\mathcal{D}^{\nu}}_{u'v'} = -\frac{1}{Re}\frac{\partial}{\partial x_k}\left(\frac{\partial \overline{u'v'}}{\partial x_k}\right)$	$\overline{\mathcal{D}^{\nu}}_{v'c'} = -\frac{\partial}{\partial x_k}\left\{\frac{1}{Re}\overline{\left(c'\frac{\partial v'}{\partial x_k}\right)} + \frac{1}{ReSc}\overline{\left(v'\frac{\partial c'}{\partial x_k}\right)}\right\}$
Pressure diffusion term	$\overline{\mathcal{D}^{\mathcal{P}}}_{u'v'} = \left\{\frac{\partial(\overline{p'u'})}{\partial y} + \frac{\partial(\overline{p'v'})}{\partial x}\right\}$	$\overline{\mathcal{D}^{\mathcal{P}}}_{v'c'} = \frac{\partial(\overline{p'c'})}{\partial y}$

To investigate the driving term of the dissimilarity between the momentum and scalar transfer, the budget equations for the momentum and scalar transfer are examined. These equations are written as follows:

$$
\begin{aligned}
-\frac{\partial \overline{u'v'}}{\partial t} &= \overline{\mathcal{C}}_{u'v'} + \overline{\mathcal{P}}_{u'v'} + \overline{\epsilon}_{u'v'} + \overline{\mathit{\Pi}}_{u'v'} \\
&+ \overline{\mathcal{D}^{\mathcal{T}}}_{u'v'} + \overline{\mathcal{D}^{\nu}}_{u'v'} + \overline{\mathcal{D}^{\mathcal{P}}}_{u'v'}, \qquad (4.2) \\
-\frac{\partial \overline{v'c'}}{\partial t} &= \overline{\mathcal{C}}_{v'c'} + \overline{\mathcal{P}}_{v'c'} + \overline{\epsilon}_{v'c'} + \overline{\mathit{\Pi}}_{v'c'} \\
&+ \overline{\mathcal{D}^{\mathcal{T}}}_{v'c'} + \overline{\mathcal{D}^{\nu}}_{v'c'} + \overline{\mathcal{D}^{\mathcal{P}}}_{v'c'}. \qquad (4.3)
\end{aligned}
$$

The right-hand terms in Eqs. (4.2) and (4.3) are called convection term, $\overline{\mathcal{C}}_{u'v'}$ and $\overline{\mathcal{C}}_{v'c'}$, production term, $\overline{\mathcal{P}}_{u'v'}$ and $\overline{\mathcal{P}}_{v'c'}$, dissipation term, $\overline{\epsilon}_{u'v'}$ and $\overline{\epsilon}_{v'c'}$, pressure-strain correlation term, $\overline{\mathit{\Pi}}_{u'v'}$, and pressure-scalr gradient correlation term, $\overline{\mathit{\Pi}}_{v'c'}$, turbulent diffusion term, $\overline{\mathcal{D}^{\mathcal{T}}}_{u'v'}$ and $\overline{\mathcal{D}^{\mathcal{T}}}_{v'c'}$, viscous diffusion term, $\overline{\mathcal{D}^{\nu}}_{u'v'}$ and $\overline{\mathcal{D}^{\nu}}_{v'c'}$, and pressure diffusion term, $\overline{\mathcal{D}^{\mathcal{P}}}_{u'v'}$ and $\overline{\mathcal{D}^{\mathcal{P}}}_{v'c'}$, respectively. Table 4.1 summarizes some representative terms in the equations which are evaluated in the present study. Figures 4.10(a) and 4.10(b) show the streamwise distributions of the budget for the momentum and scalar transfer. It should be note that the magnitude of the residual error is sufficiently smaller than dominant terms (i.e., production term, pressure-strain correlation term, pressure-scalar gradient correlation term, and pressure diffusion terms). In the upstream region, there is a greatly difference in the pressure-strain correlation term, pressure-scalar gradient correlation term, and pressure diffusion terms. Since there are no particular differences in the other terms of two budget equations, it is inferred that the differences seen in the instantaneous contour map (Figs. 4.7(a) and 4.7(b)) and the JPDF (Figs. 4.5(a) and 4.6(a)) are caused by terms related to pressure. As it goes downstream, the difference between the momentum and scalar transfer budget becomes smaller.

Finally, in order to investigate the influence of the scalar of $C = 0.0$ and 1.0 on Pr_T, we take conditional statistics based on the instantaneous concentration. The conditional turbulent Prandtl number $Pr_{Tcs}(= \upsilon_{Tcs}/\alpha_{Tcs}$, where α_{Tcs} and υ_{Tcs} are the conditional turbulent scalar diffusivity and conditional eddy diffusivity, respectively) is calculated by the reconstructed time-series data excluding the duration of the scalar of $C = 0.0$ and 1.0 in the time-series data of the instantaneous concentration. The result is shown

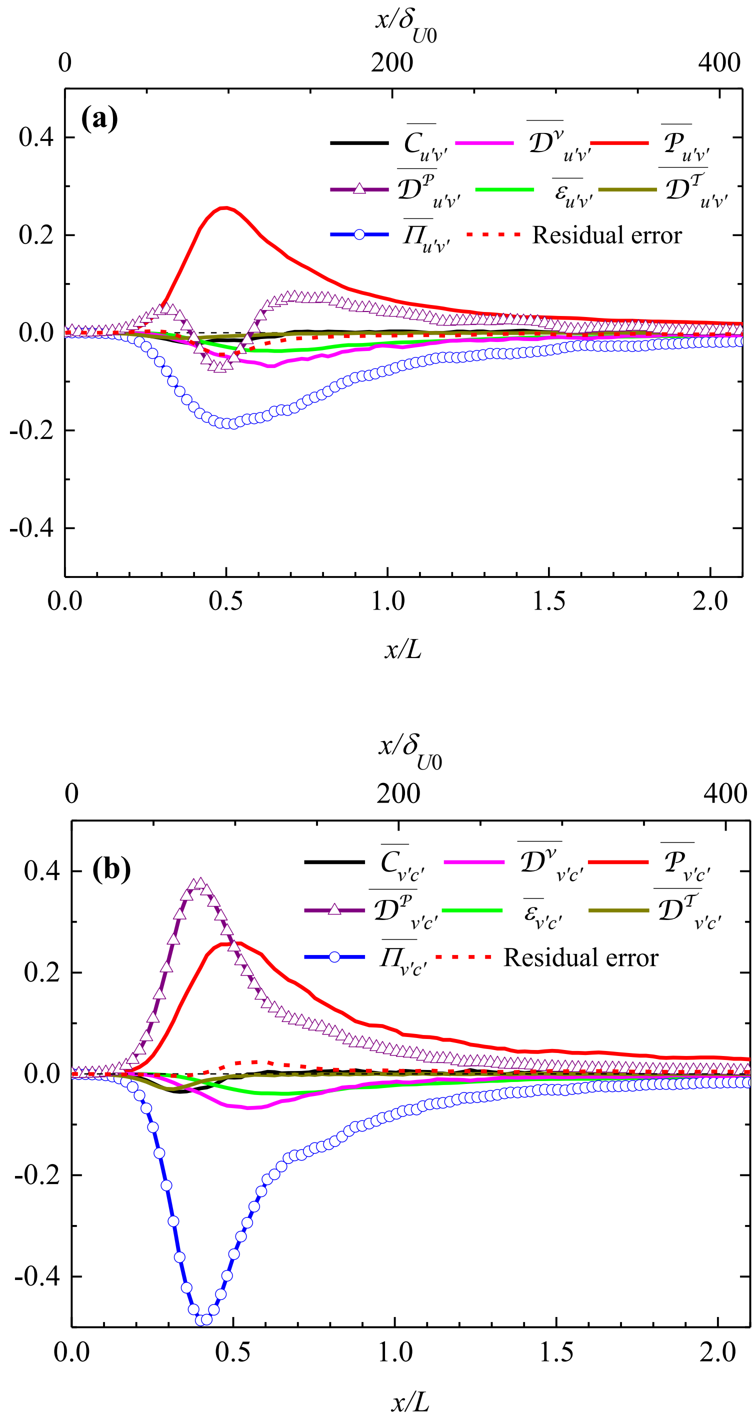

Figure 4.10: Streamwise distributions of the budget for the (a) momentum transfer and (b) scalar transfer.

in Fig. 4.11. Pr_{Tcs} takes a constant value of $Pr_{Tcs} = 0.78$ approximately at $x/L > 0.6$ and collapses to Pr_T approximately at $x/L > 1.4$. It can be seen that the existence of the duration of the scalar of $C = 0.0$ and 1.0 causes Pr_T to change, and the Prandtl number becomes a constant by removing this duration. When comparing the details of Pr_T and Pr_{Tcs}, there is no significant difference between v_T and v_{Tcs}, but α_{Tcs} is smaller than α_T on the upstream region.

In summary, when Pr_T is changing toward the downstream direction, both $(d\overline{U}/dy)/(d\overline{C}/dy)$ and $\overline{u'v'}/\overline{v'c'}$ also change. At this time, both JPDF of u' and v' and JPDF of c' and v' take a negative correlation, but there are big differences in their distributions because of existences of duration of scalar of $C = 0.0$ and $C = 1.0$. As it proceeds toward the downstream direction, both JPDF of u' and v' and JPDF of c' and v' are more similar and those co-spectra almost collapse.

4.3 Conclusions

We performed a DNS of a spatially developing shear mixing layer and investigate the influence of the large-scale structure on dissimilarity between the momentum and scalar transfer. As the main conclusions of this chapter, when Pr_T is changing as the flow goes downstream, both $(d\overline{U}/dy)/(d\overline{C}/dy)$ and $\overline{u'v'}/\overline{v'c'}$ also change, but in the region where Pr_T is constant, both of them are also constant. In both regions, JPDF of u' and v' and JPDF of c' and v' take a negative correlation. But, in the upstream region, JPDF of c' and v' is very different from JPDF of u' and v' because of the existence of the duration of the scalar of $C = 0.0$ and 1.0. The budget analysis for momentum and scalar transfer revealed that the differences between the momentum and scalar transfer are caused by terms related to pressure. In the most downstream region, both JPDF of u' and v' and JPDF of c' and v' are similar, and the co-spectrum for u' and v' and for c' and v' almost collapse.

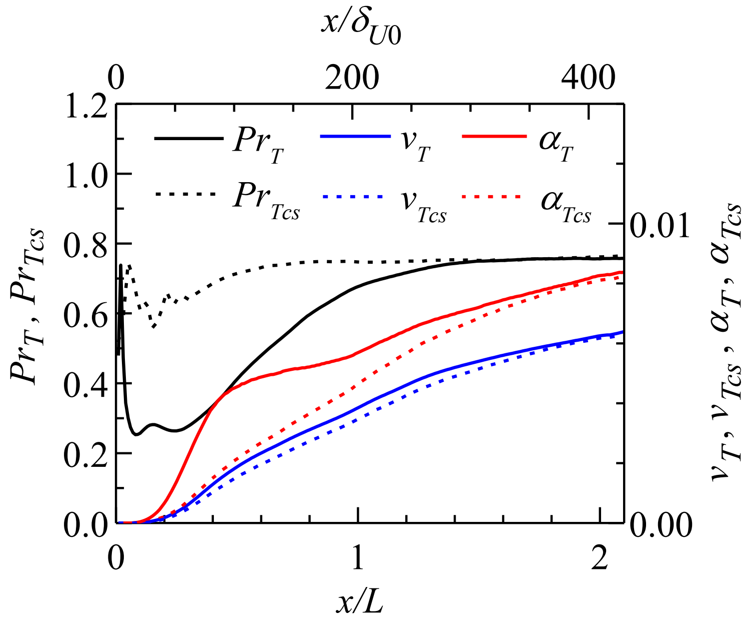

Figure 4.11: Streamwise distributions of the Pr_T, Pr_{Tcs}, v_T, v_{Tcs}, α_T, and α_{Tcs} at the center $y = 0$.

Chapter 5

Turbulent dissipation in shear mixing layer

5.1 Introduction

Theoretical analysis and modeling of turbulent flows usually require an assumption about the dissipation coefficient of the turbulent kinetic energy C_ϵ. In particular, because the turbulence model is used in various engineering situations, formulation of the dissipation coefficient is very important.

The formulation of turbulence models requires the use of pertinent scales for the velocity and size with the largest energy contribution, and it is expressed by [45]

$$C_\epsilon = \frac{\epsilon L}{(2K/3)^{\frac{3}{2}}} \sim \frac{L/\lambda}{Re_\lambda}, \tag{5.1}$$

where ϵ is the dissipation rate of the turbulent kinetic energy, L_u is the integral length scale, K is the local average of turbulent kinetic energy, and $Re_\lambda (= (2K/3)^{\frac{1}{2}}\lambda/\nu)$ is the turbulent Reynolds number based on Taylor's microscale, λ, and the kinematic viscosity, ν. Usually, the turbulence energy is transported from larger to smaller scales of motion [46], and C_ϵ takes a constant value if this downward cascade occurs without a time lag. It is a cornerstone assumption of turbulence theory [45, 46, 47, 48] and has been demonstrated in various flows [106, 107, 108, 109, 110], and it is also used in various turbulence models such as the $k - \epsilon$ model [111, 112, 113, 114].

On the other hand, turbulent flows in which C_ϵ is not constant have been found in different types of flows such as grid turbulence [115, 116, 117, 118, 119,120,121,122,123,124,125,126,127,128,129,130,131,132,133,134,135,136, 137, 138, 139, 140], uniformly sheared turbulence [141], turbulent boundary layers [142, 143], and axisymmetric turbulent wakes [144, 145, 146, 147]. In addition, direct numerical simulation (DNS) studies in box turbulence with unsteady energy input [34, 49, 50] show that, when C_ϵ is not constant, it follows the new scaling law of $C_\epsilon \sim Re_0/Re_L \sim \sqrt{Re_0}/Re_\lambda$, where $Re_0 = U_\infty L_b/\nu$, where U_∞ and L_b are respectively the initial velocity and bulk length, and $Re_L = \sqrt{K}L/\nu$ [50, 117]. This scaling holds in wakes with large-scale oscillations [144, 145, 146], constant-pressure turbulent boundary layer [142], and grid turbulence [45, 117, 119, 131], too.

Nedić and Tavoularis [141] found that C_ϵ varies toward the downstream direction in uniformly sheared turbulence. They also explained that C_ϵ is expressed as $C_\epsilon \sim Re_\lambda^\alpha$, and the changes in α are the consequences of structural changes in the turbulence. Goto and Vassilicos [34] suggested that the existence of a conspicuous peak in the power spectrum for the velocity fluctuation causes the scaling of $C_\epsilon \sim Re_\lambda^{-1}$. In this regard, the shear mixing layer is a suitable flow to investigate the relationship between C_ϵ and the coherent structure because large-scale coherent eddies induced by the Kelvin-Helmholtz (K-H) instability [9, 148] remain until far downstream [64]. In the remainder of this chapter we use the term "coherent structure" to mean the structure with temporal periodicity that has a conspicuous spectral peak in the low-wavenumber part of the power spectrum (in other words, it means the large-scale structure with a temporally periodic appearance). In fact, the mixing layer has rarely been the focus of past researches on C_ϵ. Therefore, we investigated the spatial variation of C_ϵ and the effect of the coherent structure in a spatially developing shear mixing layer on the scaling of C_ϵ by DNS.

5.2 Numerical setup

The domain is a rectangular box with a size of $L_x \times L_y \times L_z = 3.2L \times L \times L$ resolved by $N_x \times N_y \times N_z = 3,100 \times 1,460 \times 970$ grid points. The spacing in the three directions is constant and the value is $0.001L$ in the x and z directions and $0.0007L$ in the y direction. The spatial derivatives of the velocities and scalar are discretized by the fourth-order central difference

Table 5.1: Streamwise location of each station.

Station	A	B	C	D	E	F	G
x/L	0.3	0.7	1.1	1.5	1.9	2.3	2.7
x/δ_{U0}	61.4	143	225	307	389	471	553

scheme in the x, y and z directions. The spatial resolution is smaller than 2.6η. Here, η is the Kolmogorov length scale. The time step is set to $\Delta t = 5.6 \times 10^{-4}$ and the maximum Courant number is 0.3.

The computation has been performed for 600,000 time steps and $400,000$ $(= N_0)$ steps were used to obtain reliable statistical values. The length of the time series based on U_0 and L is estimated as $\Delta t N_0 U_0/L \sim 336$. The total CPU time of the present simulation was about 60,000 hours, which is sufficient time to take statistics. The condition of the inlet streamwise velocity and Reynolds number are the same as the one shown in Chapter 3.

5.3 Scaling of turbulent energy dissipation

Figure 5.1 (a) shows the streamwise distributions of the velocity fluctutations. All values are normalized by $(\Delta U)^2$ and all statistics take a constant value approximately from $x/L = 1.9$ (station E). The self-similarity for the velocity fluctuations are also investigated in Figs. 5.1 (b)-(d). All statistics collapse from $x/L = 1.9$ (station E). Thus, the present mixing layer is self-preserved downstream of $x/L = 1.9$ (station E).

Figure 5.2 shows the streamwise evolutions of the normalized momentum thickness. Here, the representative points of seven downstream locations are indicated by “A-G” (see Table 5.1 for the station locations), respectively. δ_{U0} is the initial momentum thickness obtained by extrapolating the line that indicates the mixing layer development in $1.1 \leq x/L \leq 3.0$ (linear growth set by self-similarity is observed from $x/L = 1.1$, which corresponds to station C) to $x/L = 0$ by the least squares method, and about $0.005L$. In the linearly increasing region of the momentum thickness, the growth rate is $d\delta_U/dx \approx 0.017$.

Figure 5.3 shows the power spectra for the streamwise velocity fluctuation at the center of the mixing layer at $x/L = 1.5$ (station D) and $x/L = 2.3$ (station F). The vertical and horizontal axes are normalized by the energy

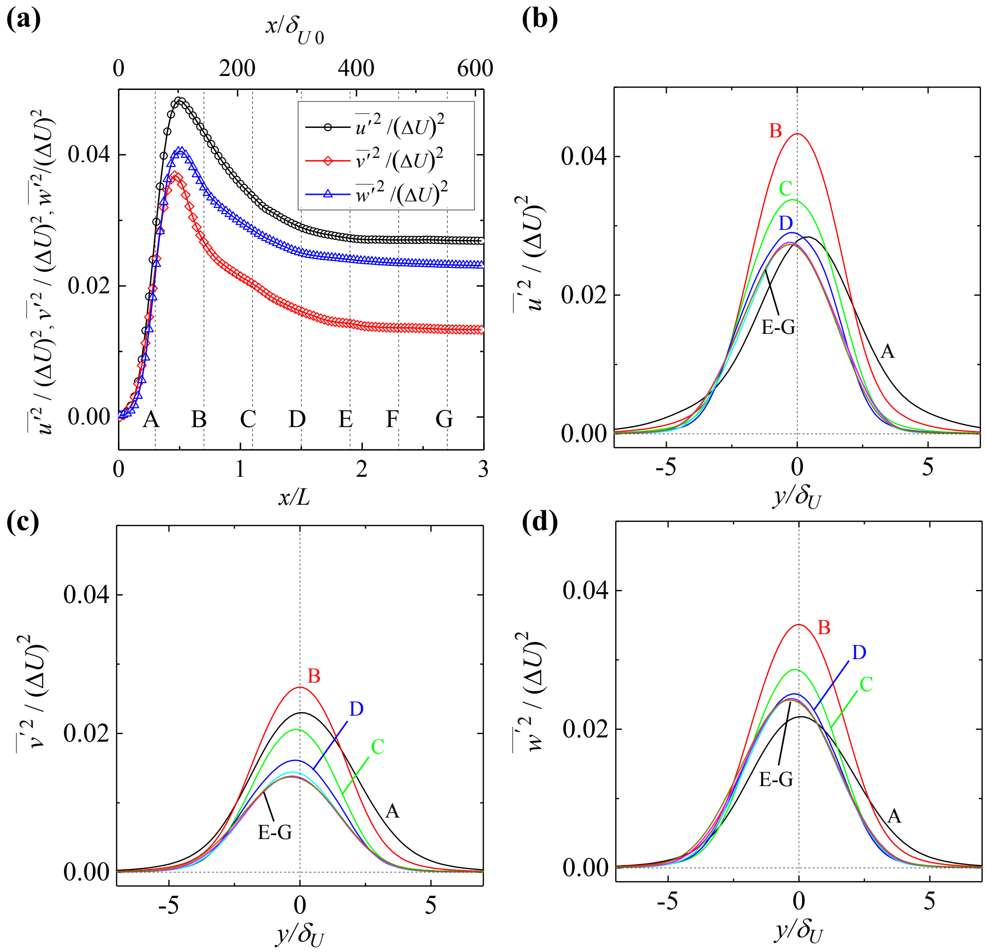

Figure 5.1: The mean-squared values of the velocity fluctuations. (a) Streamwise distributions, (b) vertical distribution of the streamwise fluctuation (c) vertical distribution of the vertical fluctuation (d) vertical distribution of the spanwise fluctuation.

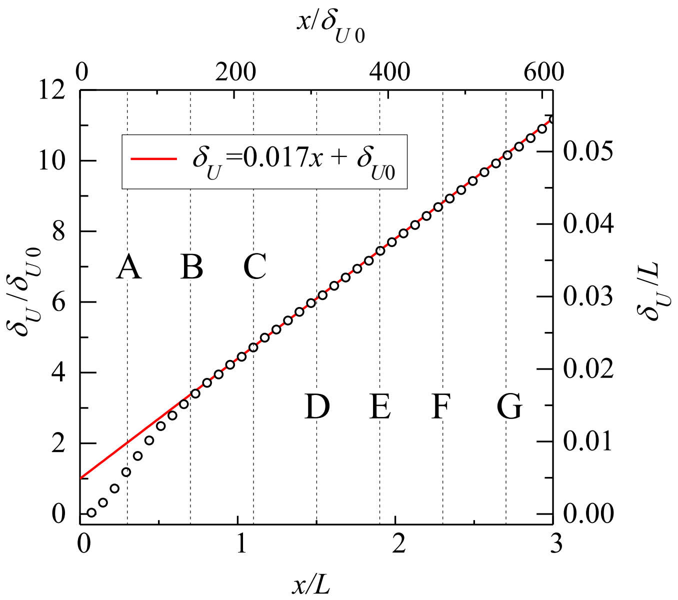

Figure 5.2: Streamwise evolution of the normalized momentum thickness. The red solid line is obtained with a least-squares fit in the range $1.1 \leq x/L \leq 3.0$; the slope of the line is 0.017.

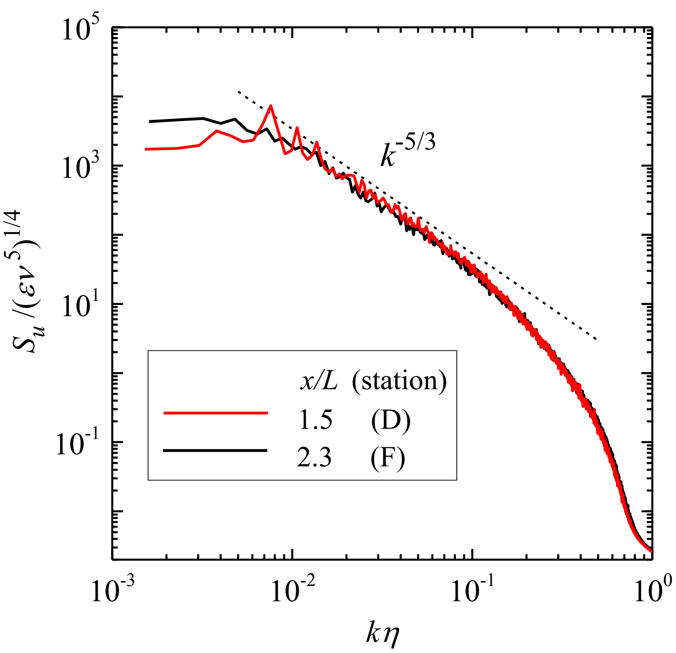

Figure 5.3: Power spectra for the streamwise velocity fluctuation at the center of the mixing layer at $x/L = 1.5$ (station D) and $x/L = 2.3$ (station F).

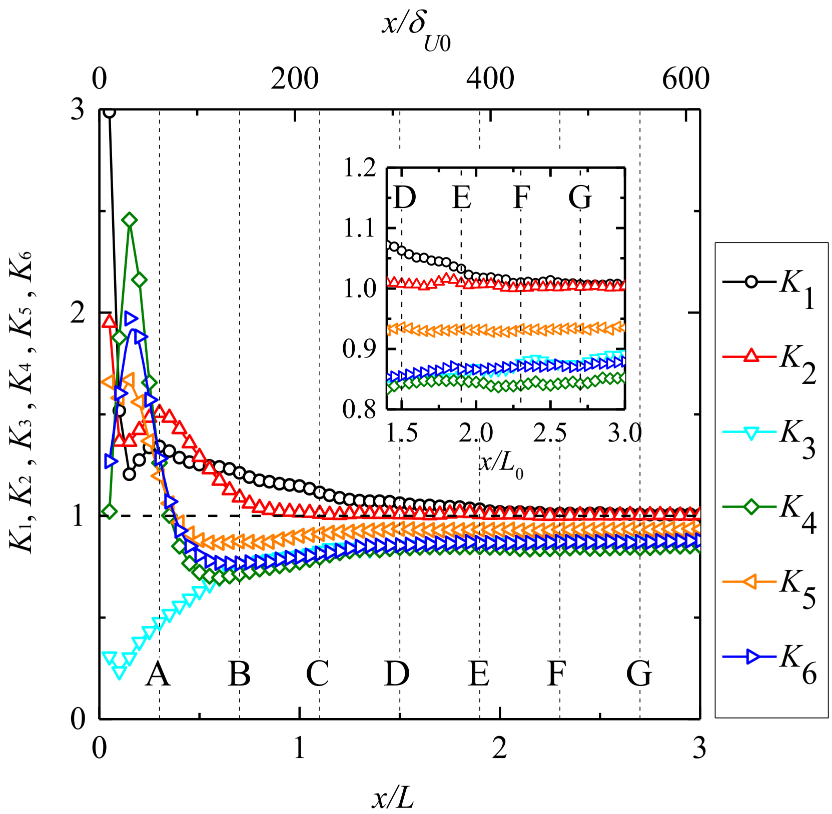

Figure 5.4: Streamwise distributions of the local isotropy at the center ($y = 0$). The inset shows the enlarged view in the downstream region (station D-G).

unit $(\epsilon\nu^5)^{1/4}$ and η, respectively. Here, the power spectra were obtained from the time-series data at fixed points. The frequency f was converted to the wavenumber k by $k = 2\pi f/\overline{U}$. At $x/L = 1.5$ (station D), spectral spikes are seen on the lower wavenumber side. However, these spikes are suppressed at $x/L = 2.3$ (station F). The inertial subrange with a $-5/3$ slope is clearly observed at both downstream locations.

Figure 5.4 shows the streamwise profiles of the ratio of the mean-squared velocity derivatives in the different directions, $K_1 - K_6$, which are commonly used as the indicators of local isotropy [112, 149, 150], and are defined as follows:

$$\begin{aligned} K_1 &= \frac{2\langle(\frac{\partial u'}{\partial x})^2\rangle}{\langle(\frac{\partial v'}{\partial x})^2\rangle}, \; K_2 &= \frac{2\langle(\frac{\partial u'}{\partial x})^2\rangle}{\langle(\frac{\partial w'}{\partial x})^2\rangle}, \; K_3 = \frac{2\langle(\frac{\partial u'}{\partial x})^2\rangle}{\langle(\frac{\partial u'}{\partial y})^2\rangle}, \\ K_4 &= \frac{2\langle(\frac{\partial u'}{\partial x})^2\rangle}{\langle(\frac{\partial u'}{\partial z})^2\rangle}, \; K_5 &= \frac{\langle(\frac{\partial u'}{\partial x})^2\rangle}{\langle(\frac{\partial v'}{\partial y})^2\rangle}, \; K_6 = \frac{\langle(\frac{\partial u'}{\partial x})^2\rangle}{\langle(\frac{\partial w'}{\partial z})^2\rangle}. \end{aligned} \tag{5.2}$$

The ratios in all pairs have constant values close to 1 ($0.85 < K_1 - K_6 < 1.1$) in the region of $x/L \geq 1.5$ (station D). Thus, it can be concluded that relatively good local isotropy holds in that region.

In high-Reynolds number self-preserving turbulence, K and L_u are expressed by $K \sim U_\infty^2(\frac{x-x_0}{L_b})^{-n}$ and $L_u \sim L_b(\frac{x-x_0}{L_b})^m$, where x_0 is a virtual origin originating from each turbulent field. Note that L_b and U_∞ can be chosen appropriately according to each turbulent field, and they are defined as "unit" in the present study. In the mixing layer, the exponents n and m are generally accepted to take values of 0 and 1, respectively [46, 121]. Figures 5.5(a) and (b) illustrate the downstream variations of K ($= \frac{1}{2}(u'^2+v'^2+w'^2)$, where u', v', and w' are the r.m.s. values of the streamwise, vertical, and spanwise velocity fluctuations, respectively, and the integral scale L_u ($= \overline{U}\int_0^{\tau_0} f(\tau)d\tau$, where $f(\tau)$ is the auto-correlation function of the streamwise velocity fluctuations and τ is the time lag, and $f(\tau)$ is integrated over the time lag from zero to τ_0 when the functions become less than 0.02). From these figures, we find that $K \propto x^0$ and $L_u \propto x^1$, respectively, from $x/L = 1.5$ (station D). By assuming the local isotropy of the turbulent kinetic energy dissipation rate, $\epsilon = 2\nu{<}e_{ij}e_{ij}{>} = 15\nu{<}(\partial u/\partial x)^2{>} \sim \nu K/\lambda^2$, where e_{ij} is $e_{ij} = (\partial u_i'/\partial x_j + \partial u_j'/\partial x_i)/2$, in which u_i denotes the fluctuation velocity component, with the cornerstone assumption $\epsilon \sim K^{3/2}/L_u$ [151, 152, 153, 154], Taylor's microscale λ for the mixing layer evolves as:

$$\lambda^2 \sim L_b^2 Re_0^{-1}\left(\frac{x-x_0}{L_b}\right). \tag{5.3}$$

That is, we obtain the relation $\lambda^2 \propto x^1$. Figure 5.6 shows the streamwise variations of Taylor's microscale λ^2 ($= (2K/3)/\langle(\partial u/\partial x)^2\rangle$). It shows that $\lambda^2 \propto x^1$ from $x/L = 1.5$ (station D).

In the same way that we derived Eq. (5.3), we obtain the evolutions of Re_λ and L_u/λ as follows:

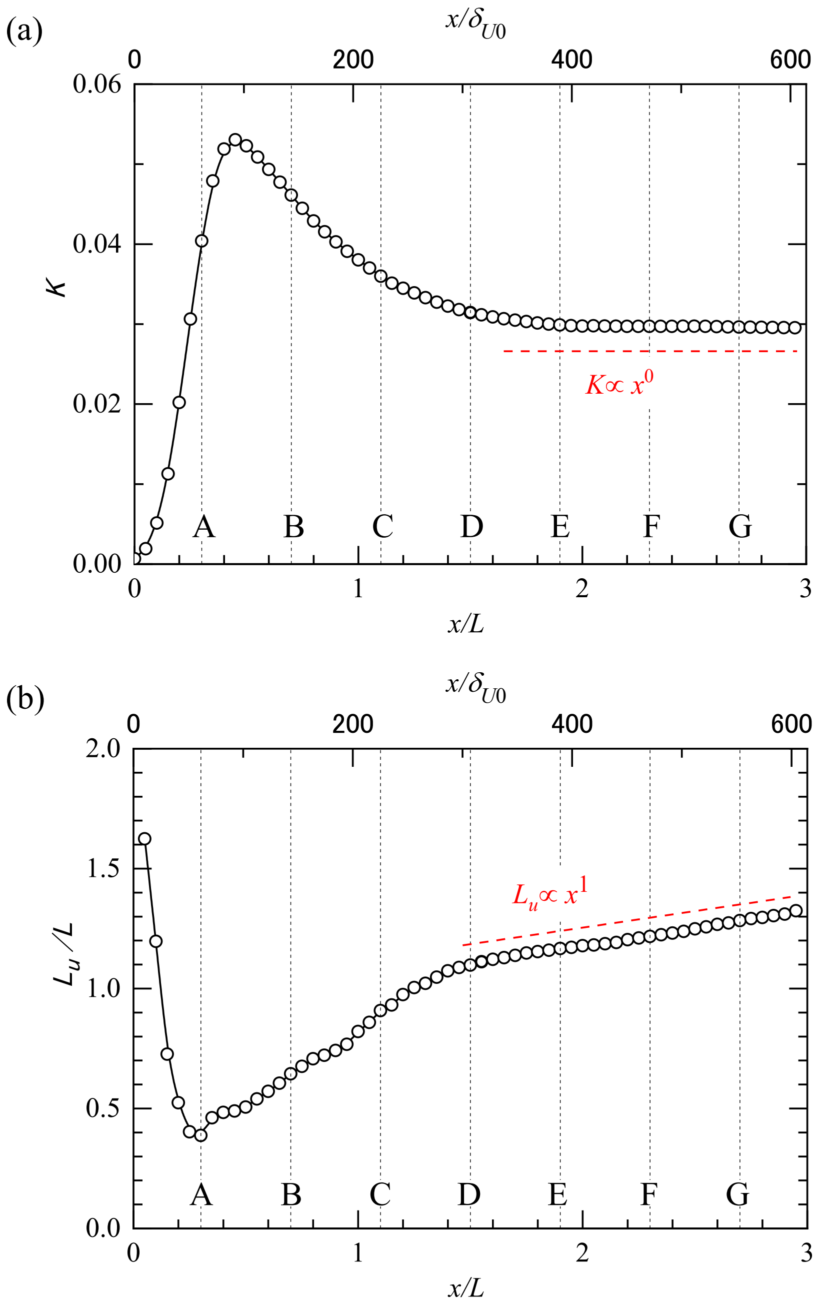

Figure 5.5: Streamwise distributions of (a) K and (b) L_u/L at the center ($y = 0$).

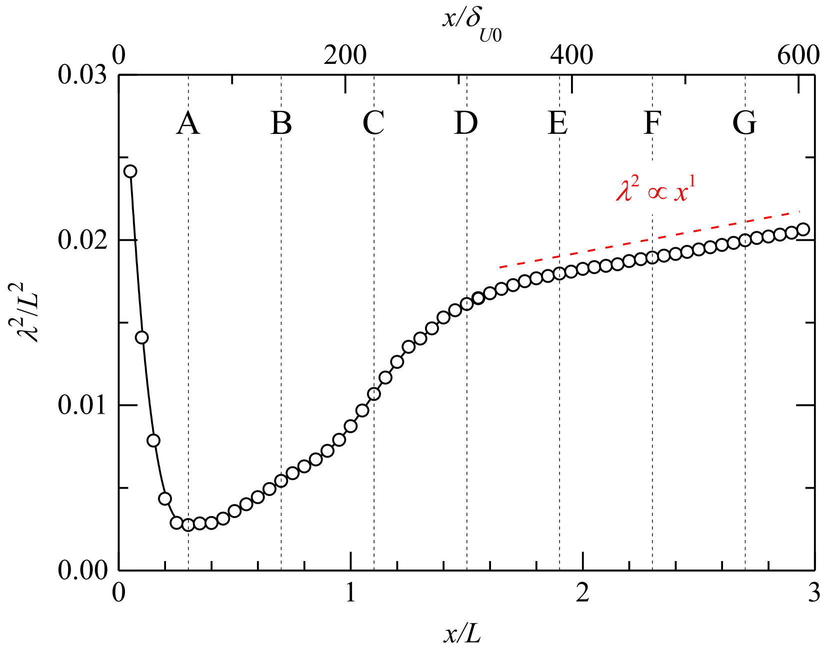

Figure 5.6: Streamwise distributions of λ^2/L^2 at the center ($y = 0$).

$$Re_\lambda = K^{\frac{1}{2}}\lambda/\nu \sim Re_0^{1/2}\left(\frac{x - x_0}{L_b}\right)^{\frac{1}{2}}, \tag{5.4}$$

$$L_u/\lambda \sim Re_0^{1/2}\left(\frac{x - x_0}{L_b}\right)^{\frac{1}{2}}. \tag{5.5}$$

That is, we obtain the relations $(Re_\lambda)^2 \propto x^1$ and $(L_u/\lambda)^2 \propto x^1$, respectively. It is worth noting that Eqs. (5.4) and (5.5) are consistent with $C_\epsilon = const.$ from the definition of C_ϵ, i.e., Eq. (5.1). Streamwise variations of $(Re_\lambda)^2$ and $(L_u/\lambda)^2$ are shown in Figs. 5.7(a) and (b), respectively. $(Re_\lambda)^2$ also shows the tendency of a linear increase in $x/L \geq 1.5$ (station D) as in L_u (Fig. 5.5(b)) and λ^2 (Fig. 5.6), but $(L_u/\lambda)^2$ (Fig. 5.7(b)) is almost constant up to $x/L = 1.9$ (station E) and increases linearly in $x/L \geq 2.3$ (station F). Figure 5.8 shows the streamwise variation of C_ϵ. It rapidly decreases toward the downstream direction, and approaches a constant value of $C_\epsilon = 0.6$ in $x/L \geq 1.5$ (station D).

Equations (5.4) and (5.5) also show the relation $L_u/\lambda \sim Re_\lambda$. The relationship between L_u/λ and Re_λ in the present study is shown in Fig. 5.9(a). It is found that L_u/λ is almost constant in $x/L \leq 1.9$ (up to station

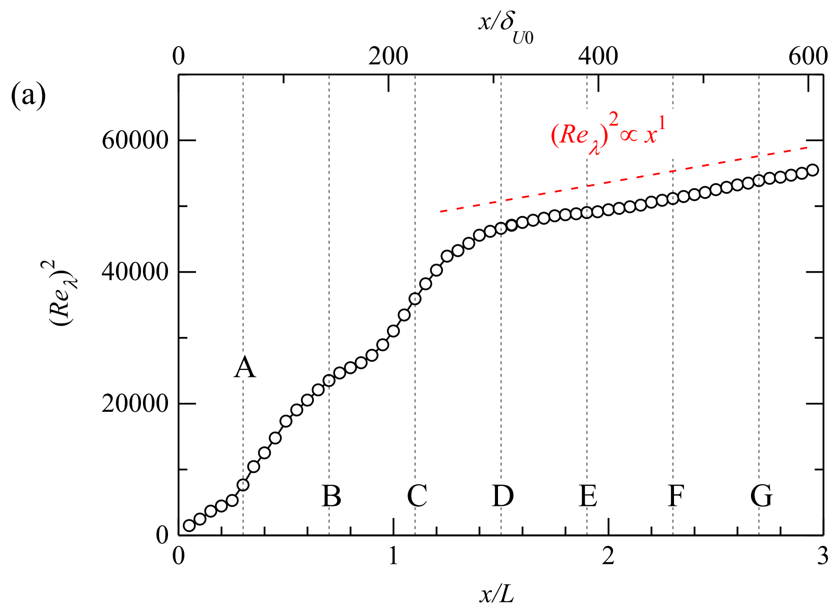

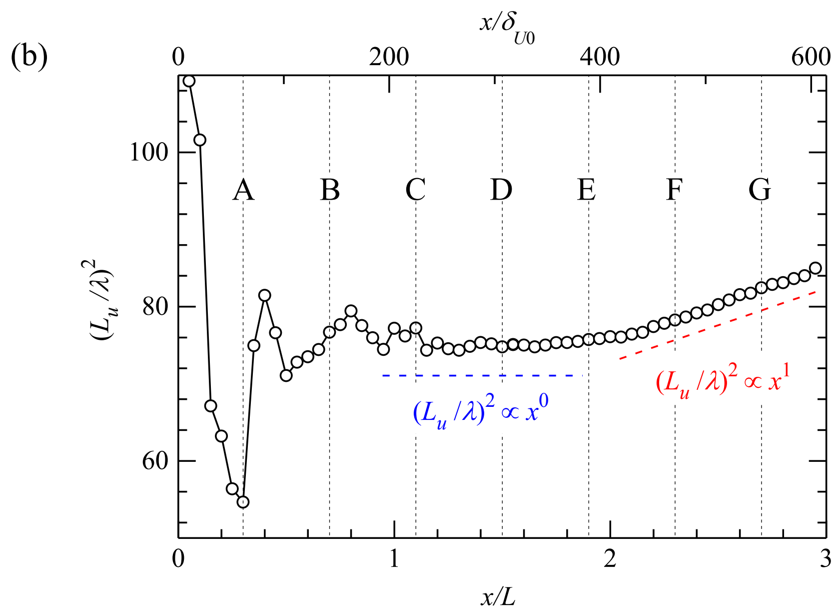

Figure 5.7: Streamwise distributions of (a) $(Re_\lambda)^2$ and (b) $(L_u/\lambda)^2$ at the center ($y = 0$).

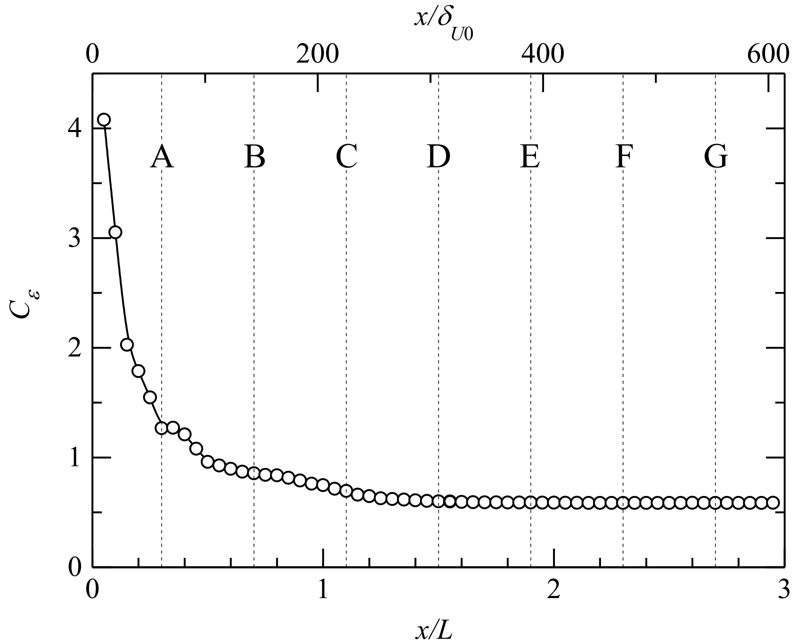

Figure 5.8: Streamwise distributions of C_ϵ at the center ($y = 0$).

E). This is the same characteristic seen in several types of grid turbulence [118, 117, 134]. In $x/L \geq 2.3$ (in the downstream region from station F), L_u/λ almost follows the slope of $C_\epsilon = 0.6$. We also show the relationship between C_ϵ and Re_λ in Fig. 5.9(b). It shows that the slope follows Re_λ^{-1} over a wide area (from station A to station E). In other words, the scaling law proposed by Goto and Vassilicos [34] also holds in the present flow.

5.4 Self-similarity of energy-containing structure

Goto and Vassilicos [34] suggested that the dissipation law changes from $C_\epsilon \sim Re_\lambda^{-1}$ to $C_\epsilon \sim Re_\lambda^{0}$ (i.e., C_ϵ takes a constant value) in accordance with the disappearance of the spectral spikes in the power spectrum for the velocity fluctuation. The scaling law based on the Taylor-Kolmogorov theory is a statistically stationary cascade in which the large-scale energy flux balances dissipation. Then, if some peaks remain on the lower wavenumber side of the spectrum, as shown in Fig. 5.3, it is thought that the dissipation rates of the small and large scales do not evolve together. This

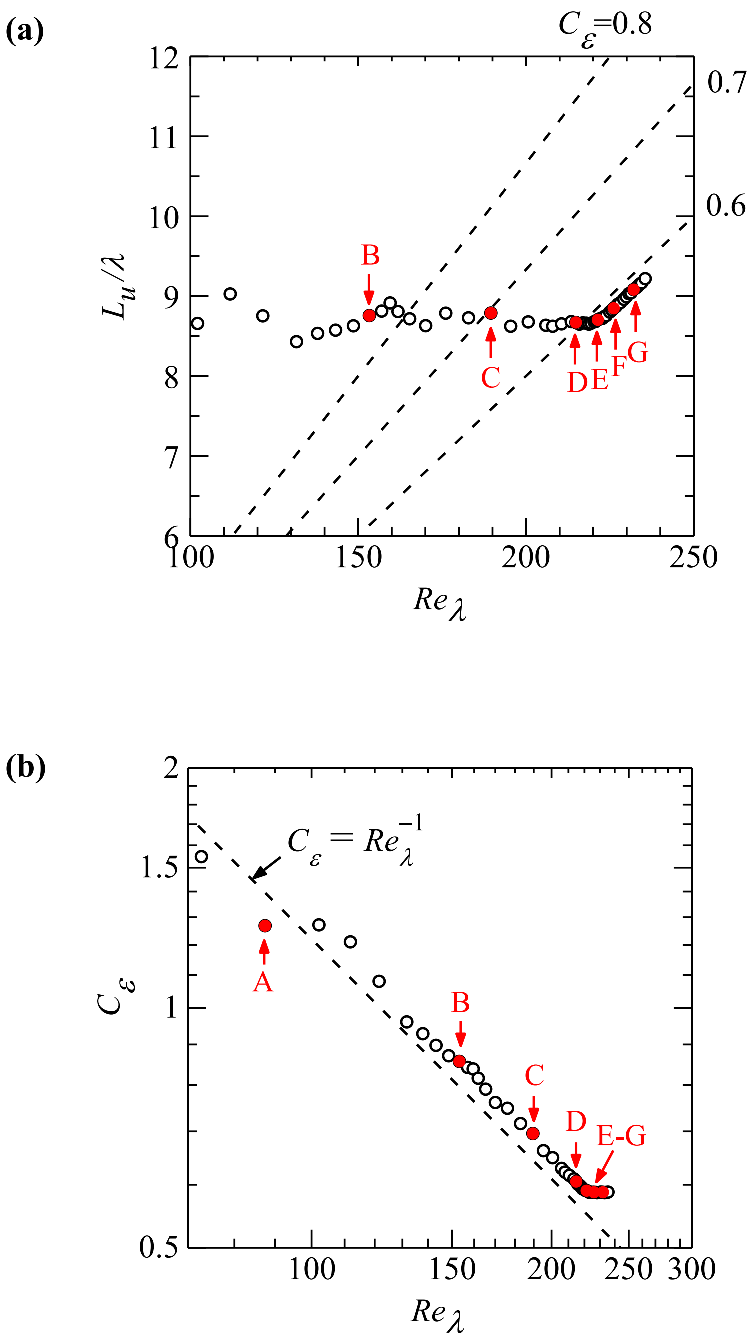

Figure 5.9: Relationships (a) between L_u/λ and Re_λ and (b) between C_ϵ and Re_λ.

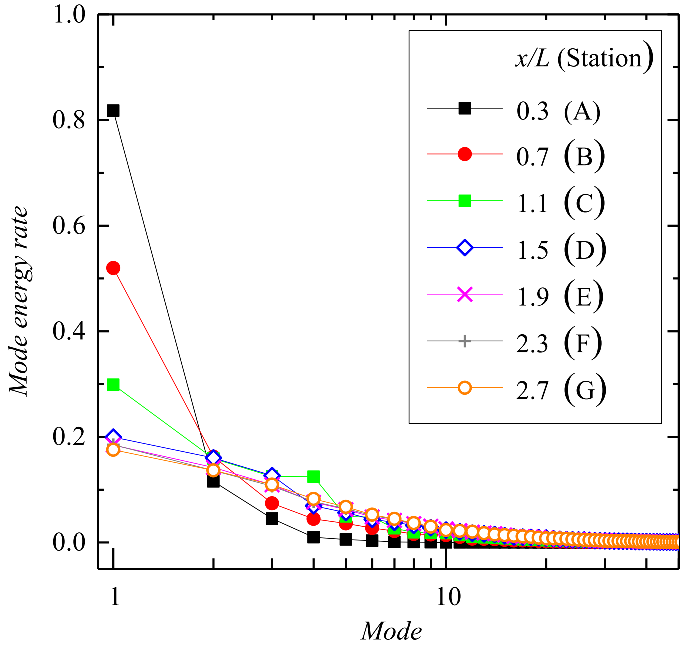

Figure 5.10: Contributions of each POD mode of the streamwise velocity fluctuation.

opinion is also supported by the work of Goto and Vassilicos [49, 34]; the instantaneous values of energy flux and dissipation are never equal in the case of an unsteady turbulence (with a peak on the low-wavenumber side of the spectrum). It is believed that this is caused by the cascade time-lag occurring between energy flux and dissipation. In the present case, $C_\epsilon \sim Re_\lambda^{-1}$ holds up to $x/L = 1.9$ (up to station E), and in the further downstream region, C_ϵ becomes $C_\epsilon \sim Re_\lambda^0$. Furthermore, in Fig. 5.3, the spectral spikes in the low-wavenumber part of the power spectra appear at $x/L = 1.5$ (station D), but they disappear at $x/L = 2.3$ (station F). The spikes in the spectrum at $x/L = 1.5$ (station D) are caused by the coherent structure induced by the K-H instability. In order to confirm the details of the large-scale energy-containing structure, we performed proper orthogonal decomposition (POD) analysis [155, 156] for the streamwise velocity fluctuation at several streamwise locations using time-series data. The contributions of each POD mode are shown in Fig. 5.10. It confirms that the first mode is dominant in the upstream region and the turbulence energy is distributed to the higher modes as the flow goes downstream. Considering that the first mode corresponds to the coherent structure in the upstream

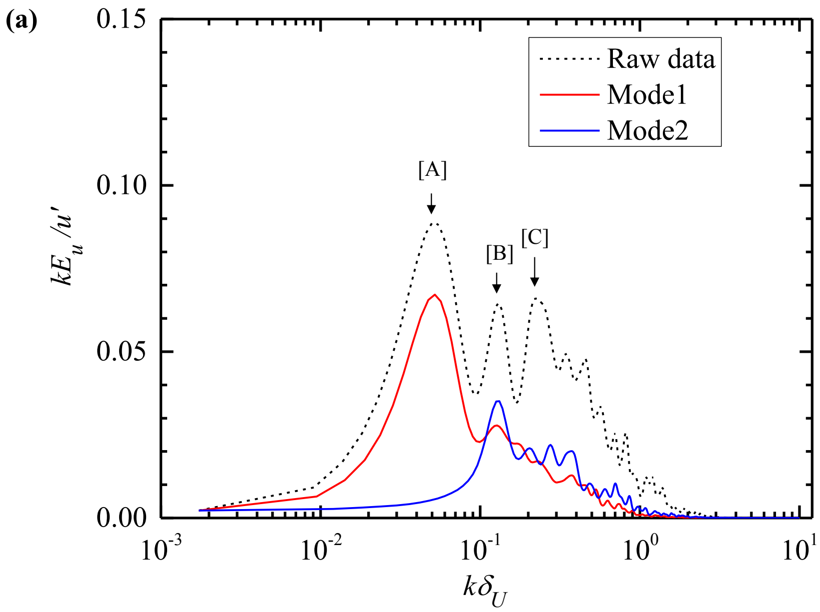

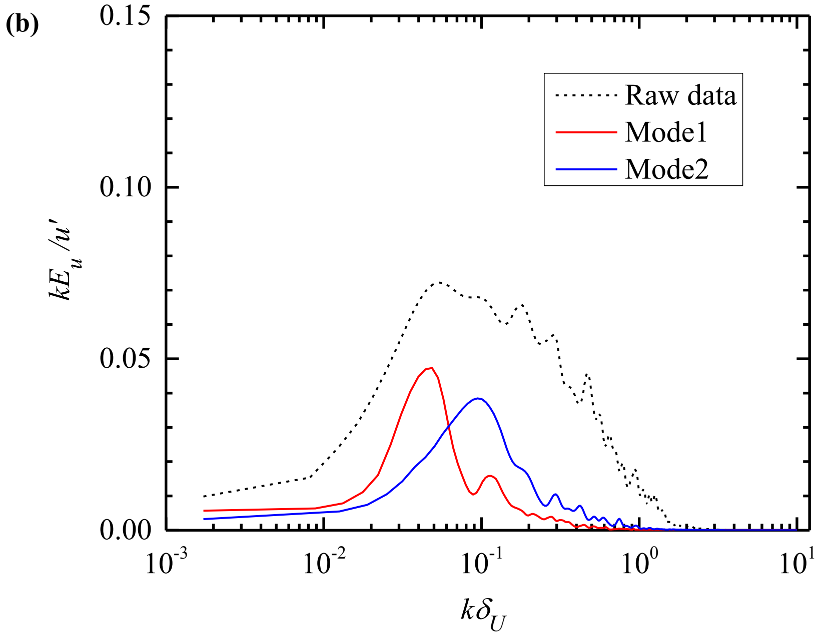

Figure 5.11: Power spectra for the first and second POD modes of the streamwise velocity fluctuation at the center ($y = 0$). (a) $x/L = 1.5$ (station D), (b) $x/L = 2.3$ (station F).

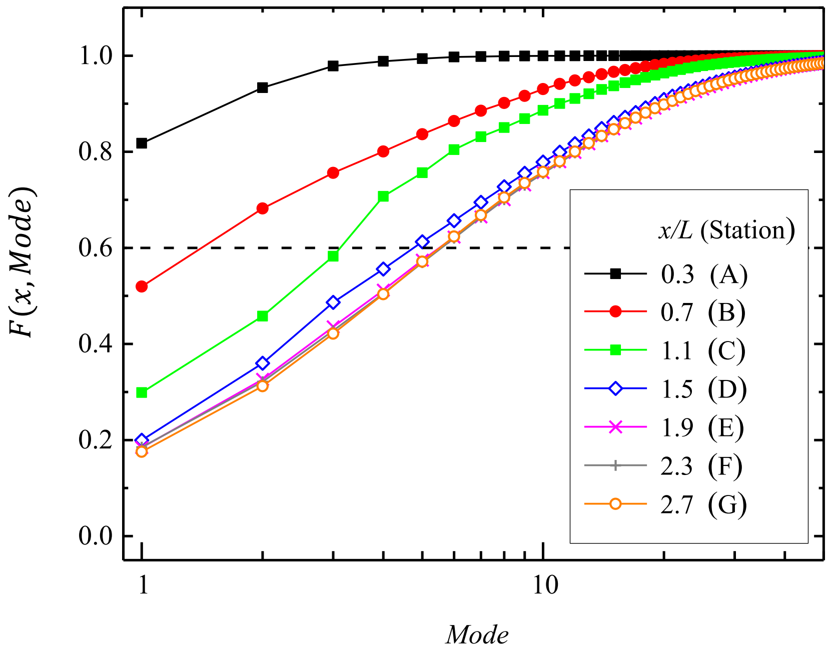

Figure 5.12: Cumulative distribution function of the mode energy rate shown in Fig. 5.10.

region [157, 158], this fact indicates that the energy of the coherent structure is dispersed into various modes with increasing streamwise distance. It should also be noted that the change in the energy distribution becomes smaller in the downstream region.

Figures 5.11(a) and (b) show the power spectra multiplied by the wavenumber for the first and second POD modes at $x/L = 1.5$ (station D), where C_ϵ follows $C_\epsilon \sim Re_\lambda^{-1}$, and $x/L = 2.3$ (station F), where $C_\epsilon \sim Re_\lambda^0$, respectively. In these figures, the power spectra for the measured raw data are also shown. At $x/L = 1.5$ (station D), the power spectrum of the raw data consists of several strong and discrete peaks. The most energetic one (indicated by A in Fig. 5.11(a)) corresponds to the coherent structure due to the K-H instability, and the second and third ones (indicated by B and C, respectively) are their harmonic components. On the other hand, at $x/L = 2.3$ (station F), Fig. 5.11(b) shows that the spectrum of the raw data has a broader distribution, and the spectrum peak of the first POD mode is smaller than that at $x/L = 1.5$ (station D).

The frequency of appearance of the large-scale energy-containing structure of the mixing layer changes as the flow goes downstream. This is

Table 5.2: Information for reconstructing time-series data.

Station	A	B	C	D	E	F	G
x/L	0.3	0.7	1.1	1.5	1.9	2.3	2.7
$Mode$	1	2	4	5	6	6	6
F_{th}	0.82	0.68	0.71	0.61	0.62	0.62	0.62

because these structures are merged, strained, and collapsed, and excited to different frequencies. The harmonics components shown in [B] and [C] in Fig. 5.11(a) are the result of energy excitation. Therefore, we think these harmonics components are parts of a large-scale energy-containing structure. Looking at the spectrum of the first mode in Fig. 5.11(a), if only peak [A] is captured, it is insufficient for the extraction of the energy containing structure. Hence, we will try to reconstructed data including more of these energy-containing structures. The cumulative distribution function $F(x, Mode)$ of the mode energy rate (as shown in Fig. 5.10) is shown in Fig. 5.12, and it is expressed by the following equation:

$$F(x, Mode) = \sum_{n=1}^{Mode} (Mode\ energy\ rate). \tag{5.6}$$

Figure 5.12 is used to construct the time-series data expressing the structure governing the mixing layer. The time-series data is created by summing the modes until the cumulative energy rate exceeds 60 %, and this cumulative energy rate is defined as F_{th} (see Table 5.2 for information on reconstructing time-series data). The spectra of the POD reconstructed signals are shown in Fig. 5.13 with spectra of raw signals. Since the power spectrum for the reconstructed data includes peaks [A], [B], and [C] at $x/L = 1.5$ (Fig. 5.13 (a)), it is sufficient for extracting the dominant energy-containing structure. At $x/L = 2.3$ (Fig. 5.13 (b)), it is found that the reconstructed spectrum covers a wide area of the low-wavenumber region. To phenomenologically visualize the large-scale energy-containing structure, reconstructed isopleth maps of the streamwise velocity fluctuation at $x/L = 2.3$ is presented in Fig. 5.14. By reconstructing the data, it illustrates that fine disturbances seen in raw data (Fig. 5.14 (a)) is eliminated and a large-scale energy-containing structure can be extracted (Fig. 5.14 (b)).

Figure 5.15 shows time-series data of the streamwise velocity fluctuation

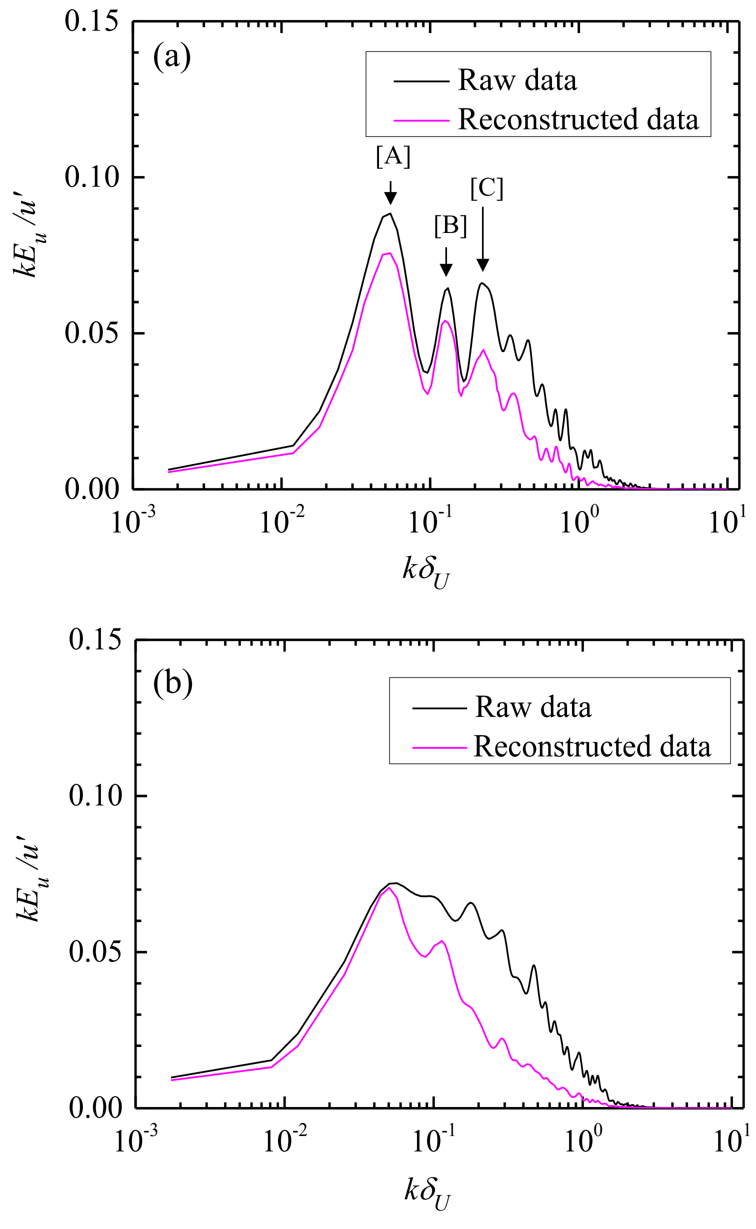

Figure 5.13: Power spectra for raw data and POD reconstructed data according to the condition of Table 2 of the streamwise velocity fluctuation at the center ($y = 0$). (a) $x/L = 1.5$ (station D), (b) $x/L = 2.3$ (station F).

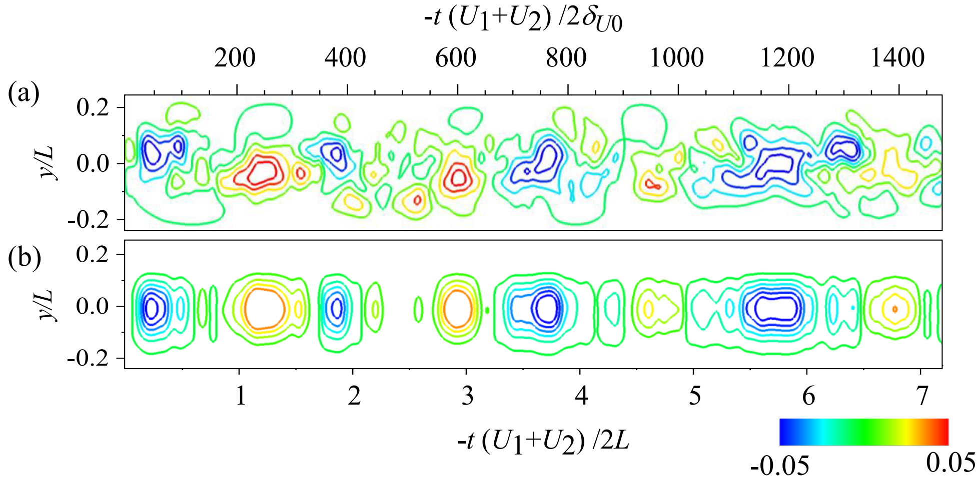

Figure 5.14: Reconstructed isopleth maps of the streamwise velocity fluctuation at $x/L = 2.3$ (station F). (a) Raw data, (b) POD reconstructed data accoridng to the condition of Table 2.

at the center reconstructed from the data composed by the sum of the modes until the cumulative energy rate exceeds 60 %. Note that the broken line in Figure 5.15 shows $u' = 0$. We also measured the streamwise length, L_{cycle}, which is the length estimated from the cycle of the zero-crossing point of the time-series data created as described above. Here, L_{cycle} is expected to be the length corresponding to the large-scale energy-containing structure in the mixing layer. Figure 5.16 shows the probability density function of L_{cycle} normalized by L_u. A peak appears at all locations, but it is sharp in the upstream region whereas the distribution becomes broader and less peaked as the flow goes downstream. Further, these distributions almost collapse for $x/L \geq 2.3$ (station F). In other words, the streamwise length corresponding to the large-scale energy-containing structure varies in the broader range, and its distribution becomes the same in the downstream region ($x/L \geq 2.3$), where C_ϵ follows $C_\epsilon \sim Re_\lambda^0$, whereas it is relatively confined in the narrower range in the upstream region ($x/L \leq 1.9$), where C_ϵ follows $C_\epsilon \sim Re_\lambda^{-1}$. Therefore, Fig. 5.16 reveals that C_ϵ becomes a constant when the distributions of L_{cycle} reach a self-similar state. This proposal is also supported by Fig. 5.12. When the energy distributions from large to small scale reaches a self-similar state, the cumulative distribution function should collapse because it means that the energy holding ratio for each wavenumber in the power spectrum is the same regardless of the

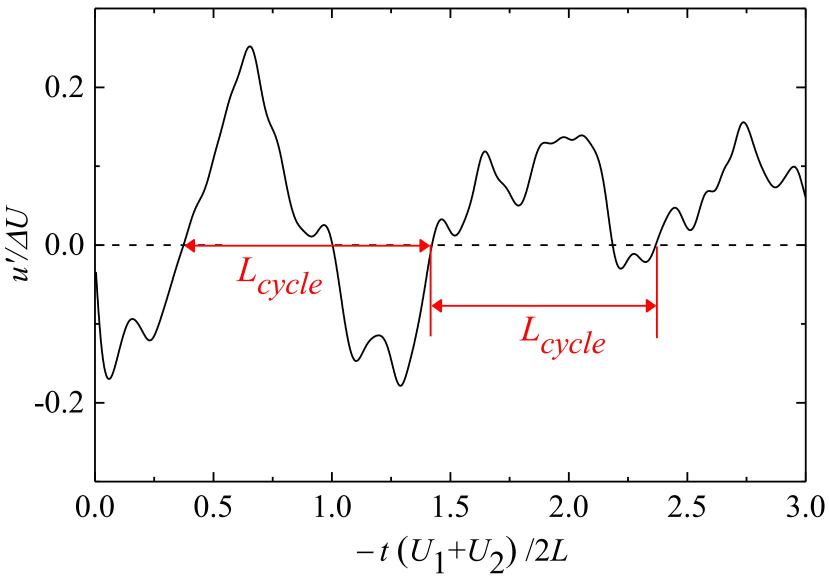

Figure 5.15: Image of normalized time-series data of the streamwise velocity fluctuation at the center. L_{cycle} is the streamwise length estimated from the cycle of the zero-crossing point of the velocity fluctuation.

downstream location. In fact, Fig. 5.12 collapses in $x/L \geq 2.3$ (station F).

It can be seen from Figs. 5.10 and 5.12 that the graphs do not collapse in the lower order mode on the upstream side. This indicates dissimilarity of energy distribution in lower order modes. Figure 5.16 clearly shows that the dissimilarity in the lower order mode is related to the dissimilarity of the distribution of large-scale energy-containing structures.

To deduce the relationship between L_{cycle} and the large-scale energy-containing structure, the ratio, between the integral scale of the streamwise direction and the averaged value of the zero-crossing length of the POD reconstructed signal, i.e., $\overline{L}_{cycle}/L_u$, is presented in Fig. 5.17. In the region where L_u linearly increases ($x/L \geq 1.5$) in Fig. 5.5(b), $\overline{L}_{cycle}/L_u$ is distributed between 1 and 1.15. We also took a maximum value, L^{max}_{cycle}, of the distribution of L_{cycle} in Fig. 5.17. L^{max}_{cycle}/L_u is distributed between 1 and 1.2. Hence, it is clear that L_{cycle} corresponds to a large-scale.

In summary, when the distribution of L_{cycle} does not reach the self-similar state, C_ϵ follows $C_\epsilon \sim Re_\lambda^{-1}$, and when it reaches the self-similar state, C_ϵ follows $C_\epsilon \sim Re_\lambda^{0}$ (i.e., C_ϵ takes a constant value). This study suggests that it is necessary to satisfy the self-similarity of the distribution of the length of the large-scale energy-containing structure in order to apply

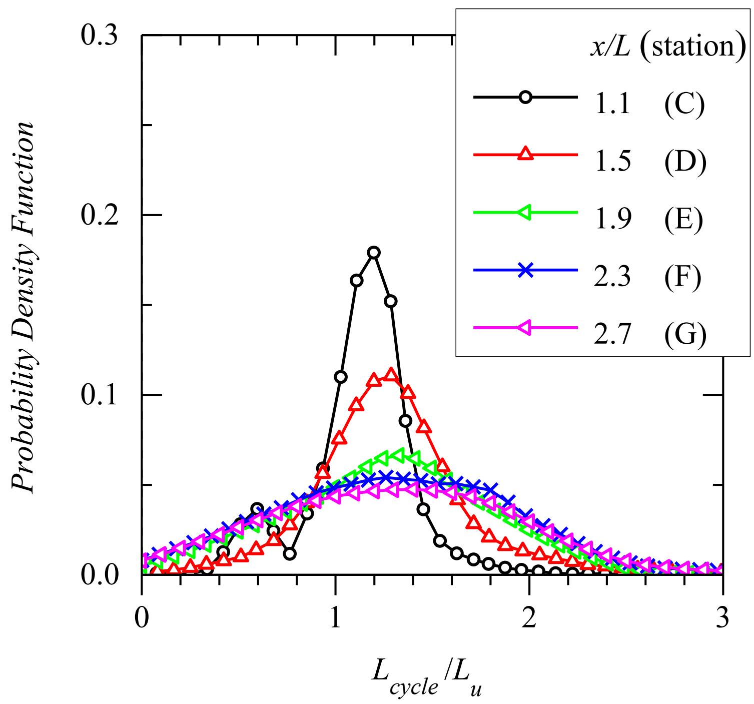

Figure 5.16: Probability density function of L_{cycle} for each downstream location at the center. The time-series data is created by the sum of the modes until the cumulative energy rate exceeds 60 %.

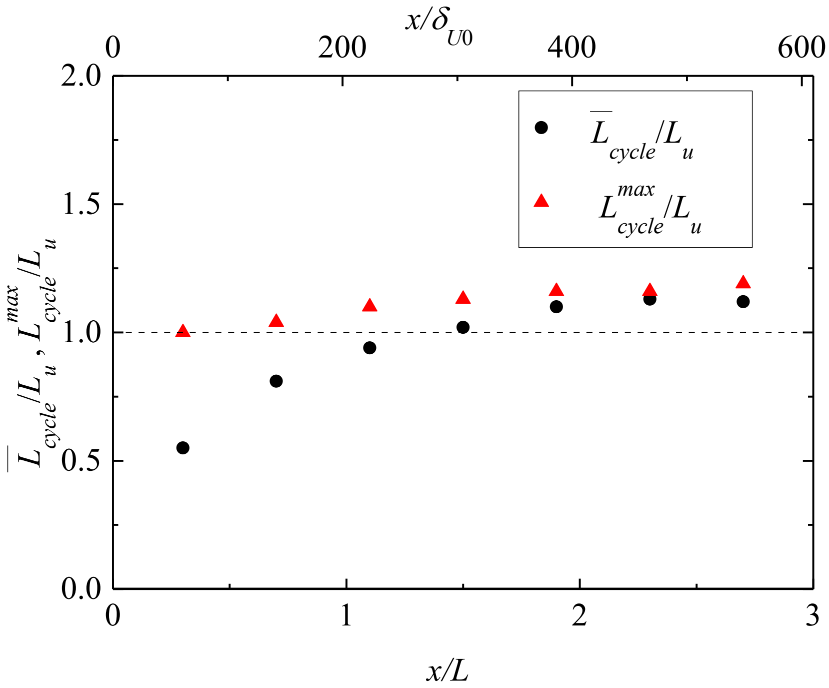

Figure 5.17: Streamwise distribution of $\overline{L}_{cycle}/L_u$ and L^{max}_{cycle}/L_u.

the condition where C_ϵ is a constant. The results in this study would help formulate new theories and improve various turbulence models based on the hypothesis $\epsilon \sim K^{3/2}/L_u$ such as the $k-\epsilon$ model.

5.5 Conclusions

In this chapter, the spatial change in C_ϵ in the mixing layer is investigated in association with the self-similarity of the large-scale energy-containing structure by DNS. It is found that the scaling law $C_\epsilon \sim Re_\lambda^{-1}$ holds over a wide area in the upstream region, and C_ϵ takes a constant value on the further downstream side. Although the streamwise length of the large-scale energy-containing structure in the mixing layer exists in both regions, its distribution is concentrated on a certain scale in the former region whereas it varies over a broader range in the latter region. It is also revealed that C_ϵ becomes a constant when its distributions reach a self-similar state. Furthermore, this study suggests that it is necessary to satisfy the self-similarity of the distribution of the length of the large-scale energy-containing structure in order to apply the condition that C_ϵ is a constant.

Chapter 6

Conclusion

We perform simulations of turbulence generated by the free-shear mixing layer. The result of this thesis is divided into three parts (Chapters 3, 4, and 5). Here the conclusions for each chapter are summarize.

Characteristics of the momentum transport process of the turbulent field coexisting with the large-scale structure were investigated in Chapter 3. The aim of this study is to clarify the driving mechanism and the vortical structure of the partial counter-gradient momentum transport (CGMT) appearing in the quasi self-similar region. In the present DNS, the self-similarity is confirmed in $x/L \geq 0.67$ ($x/\delta_{U0} \geq 137$), where L and δ_{U0} are the vertical length of the computational domain and the initial momentum thickness, respectively. However, the trend of CGMT is observed at around $k\delta_U = 0.075$ and 0.15, where k is the wavenumber, δ_U is the normalized momentum thickness at $x/L = 0.78$ ($x/\delta_{U0} = 160$), and $k\delta_U = 0.075$ corresponds to the distance between the vortical/stretching regions of the coherent structure. The budget analysis for the Reynolds shear stress reveals that CGMT is caused by the pressure diffusion term at the off-central region and by $-\overline{p(\partial u/\partial y)}$ in the pressure-strain correlation term at the central region. As the flow moves toward the downstream direction, the appearance of those terms becomes random and the trend of CGMT at the specific wavenumber bands disappears. Furthermore, we investigated the relationship between the CGMT and vorticity distribution in the vortex region of the mixing layer, in association with the spatial development. In the upstream location, the high-vorticity region appears in the boundary between the areas of gradient momentum transport (GMT) and CGMT. The area generating the loss of the Reynolds shear stress gradually spreads by flowing toward the downstream direction, and subsequently, the fluid mass with high-vorticity is transported from the forehead stretching region toward the counter-gradient direction. In this location, the velocity fluctuation in the high-vorticity region is large. In view of this, the trend generating the loss of the Reynolds shear stress appears in the flow where the turbulence production and non-turbulent regions mix. Then, the non-turbulent region and CGMT almost simultaneously disappear in the fully-developed region.

In Chapter 4, we aim to clarify the influence of the large-scale structure on the turbulent Prandtl number Pr_T. As a main conclusion, Pr_T takes a small value ($Pr_T \sim 0.5$) in the dominant region of the large-scale structure. The budget analyses for the Reynolds stress equation and the scalar flux equation revealed that the differences between the momentum and scalar transfer are caused by terms related to pressure (i.e., pressure-strain correlation term, pressure-scalar gradient correlation term, and pressure diffusion terms). Phenomenally, the momentum in the field where a large-scale vortex coexists tends to be transported toward the counter-gradient direction under the influence of pressure, but the scalar is transported toward the gradient direction. As a result, it is thought that the difference in the driving force between the momentum and scalar transport causes the decrease of the Pr_T.

In Chapter 5, we investigate the spatial transition of the dissipation coefficient of the turbulent kinetic energy, C_ϵ. The scaling law suggested by Goto and Vassilicos [Phys. Rev. E **94**, 053108 (2016)], $C_\epsilon \sim Re_\lambda^{-1}$, holds over a wide area in the upstream region ($0.3 \leq x/L_0 \leq 1.9$, where x is the streamwise direction and L_0 is the height of the computational domain), and C_ϵ takes a constant value in the further downstream region, where Re_λ is the turbulent Reynolds number based on Taylor's microscale. Proper orthogonal decomposition (POD) analysis is performed to investigate the distributions of the streamwise length of the large-scale energy-containing structure, which is estimated from the cycle of the zero-crossing point of the time-series data composed of the sum of the POD modes until the cumulative energy rate exceeds 60 %. It is shown that C_ϵ becomes a constant when the distributions of the length of the large-scale structure reach a self-similar state. This result suggests that it is necessary to satisfy the self-similarity of the distribution of the length of the large-scale energy-containing structure in order to apply the condition that C_ϵ is a constant.

Acknowkedgements

Thank you for my supervisor, Professor Yasuhiko Sakai. The completion of this thesis is impossible for me without his support and encouragement. I owe my deepest gratitude to Associate Professor Yasumasa Ito for his helpful suggestions through my time in Nagoya University. I really learned a lot from the invaluable discussions with him. I would also like to thank Assistant Professor Koji Iwano whose meticulous comments were an enormous help to me. I am grateful to Professor Yohei Morinishi (Nagoya Institute of Technology) and Professor Koji Nagata (Nagoya University) for reviewing this thesis and for their valuable comments. I also would like to thank all group members at Statistical Fluid Engineering Lab. I am also extremely grateful to Assistant Professor Takuya Kitamura (Nagasaki University). I got a lot of opinions from him.

Bibliography

[1] S. Corrsin, "Investigation of flow in an axially symmetric heated jet in air," NACA ACR 3L23 and Wartime Report **W94** (1943).

[2] A. A. Townsend, "Measurements in the turbulent wake of a cylinder," Proc. R. Soc. London Ser. **190**, 551 (1947).

[3] L. S. G. Kovasznay, "The turbulent boundary layer," Annu. Rev. Fluid Mech. **2**, 95 (1970).

[4] A. S. Monin and A. M. Yaglom, Statistical Fluid Mechanics: Mechanics of Turbulence, volume I (MIT, Cambridge, MA, 1971).

[5] A. S. Monin and A. M. Yaglom, Statistical Fluid Mechanics: Mechanics of Turbulence, volume II (MIT, Cambridge, MA, 1975).

[6] J. L. Lumley, "Computational modeling of turbulent flows," Adv. Appl. Mech. **18**, 123 (1978).

[7] J. L. Lumley, Coherent structures in turbulence, in Transit edited by R. E. Meyer (Academic Press, 1981).

[8] C.-M. Ho and P. Huerre, "Perturbed free shear layers," Annu. Rev. Fluid Mech. **16**, 365 (1984).

[9] G. L. Brown and A. Roshko, "On density effects and large structure in turbulent mixing layers," J. Fluid Mech. **64**, 775 (1974).

[10] G. M. Corcos and F. S. Sherman, "The mixing layer: deterministic models of a turbulent flow. Part 1. Introduction and the two-dimensional flow," J. Fluid Mech. **139**, 29 (1984).

[11] G. M. Corcos and S. J. Lin, "The mixing layer: deterministic models of a turbulent flow. Part 2. The origin of the three-dimensional motion," J. Fluid Mech. **139**, 67 (1984).

[12] S. J. Lin and G. M. Corcos, "The mixing layer: Deterministic models of a turbulent flow. Part 3. The effect of plane strain on the dynamics of streamwise vortices," J. Fluid Mech. **141**, 139 (1984).

[13] J. C. Lasheras, J. S. Cho, and T. Maxworthy, "On the origin and evolution of streamwise vortical structures in a plane, free shear layer," J. Fluid Mech. **172**, 231 (1986).

[14] J. C. Lasheras and J. S. Cho, "Three-dimensional instability of a plane free shear layer: an experimental study of the formation and evolution of streamwise vortices ," J. Fluid Mech. **189**, 53 (1988).

[15] C. D. Winant and F. K. Browand, "Vortex pairing, the mechanism of turbulent mixing layer growth at moderate Reynolds number," J. Fluid Mech. **63**, 237 (1974).

[16] F. K. Browand and T. R. Troutt, "The turbulent mixing layer: geometry of large vortices," J. Fluid Mech. **158**, 489 (1985).

[17] R. D. Moser and M. M. Rogers, "The three-dimensional evolution of a plane mixing layer: pairing and transition to turbulence," J. Fluid Mech. **247**, 275 (1993).

[18] D. Oster, I. Wygnanski, and H. E. Fiedler, Some preliminary observations on the effect of initial conditions on the structure of the two-dimensional turbulent mixing layer. In Turbulence in Internal Flows (ed. Murthy, S. N. B.) **67**. Hemisphere (1977).

[19] F. K. Browand and B. O. Latigo, "Growth of the two-dimensional mixing layer from a turbulent and nonturbulent boundary layer," Phys. Fluids **22** 1011 (1979).

[20] M. G. Mungal and P. E. Dimotakis, "Mixing and combustion with low heat release in a turbulent mixing layer," J. Fluid Mech. **148** 349 (1984).

[21] M. G. Mungal, J. C. Hermanson, and P. E. Dimotakis, "Reynolds number effects on mixing and combustion in a reacting shear layer," AIAA J. **23** 1418 (1985).

[22] J. H. Bell and R. D. Mehta, "Development of a two-stream mixing layer from tripped and untripped boundary layers," AIAA J. **28** 2034 (1990).

[23] P. S. Karasso and M. G. Mungal, "Scalar mixing and reaction in plane liquid shear layers," J. Fluid Mech. **323** 23 (1996).

[24] M. D. Slessor, C. L. Bond, and P. E. Dimotakis, "Turbulent shear-layer mixing at high Reynolds numbers: effects of inflow conditions," J. Fluid Mech. **376** 115 (1998).

[25] S. Suryanarayanan and R. Narasimha, "Insights into the growth rate of spatially evolving plane turbulent free-shear layers from 2D vortex-gas simulations," Phys. Fluids **29**, 020708 (2017).

[26] A. D'Ovidio and C. M. Coats, "Organized large structure in the post-transition mixing layer. Part 1. Experimental evidence," J. Fluid Mech. **737**, 466 (2013).

[27] W. A. McMullan, S. Gao, and C. M. Coats, "Organized large structure in the post-transition mixing layer. Part 2. Large-eddy simulation," J. Fluid Mech. **762**, 302 (2015).

[28] M. M. Rogers and R. D. Moser, "Direct simulation of a self-similar turbulent mixing layer," Phys. Fluids **6**, 903 (1994).

[29] E. Balaras, U. Piomelli, and J. M. Wallace, "Self-similar states in turbulent mixing layers," J. Fluid Mech. **446**, 1 (2001).

[30] A. Attili and F. Bisetti, "Statistics and scaling of turbulence in a spatially developing mixing layer at $\mathrm{Re}_\lambda = 250$," Phys. Fluids **240**, 035109 (2012).

[31] D. Fiscaletti, A. Attili, F. Bisetti, and G. E. Elsinga, "Scale interactions in a mixing layer - the role of the large-scale gradients," J. Fluid Mech. **791**, 154 (2016).

[32] C. Meneveau and J. Katz, "Scale-Invariance and Turbulence Models for Large-Eddy Simulation," Annu. Rev. **32** 1 (2000).

[33] Y. Ito, K. Nagata, Y. Sakai, and O. Terashima, "Momentum and mass transfer in developing liquid shear mixing layers," Exp. Therm. and Fluid Sci. **51**, 28 (2013).

[34] S. Goto and J. C. Vassilicos, "Unsteady turbulence cascades," Phys. Rev. E **94**, 053108 (2016).

[35] S. Laizet, S. Lardeau, and E. Lamballais, "Direct numerical simulation of a mixing layer downstream a thick splitter plate," Phys. Fluids **22**, 015104 (2010).

[36] L. M. Pickett and J. B. Ghandhi, "Passive scalar mixing in a planar shear layer with laminar and turbulent inlet conditions," Phys. Fluids **14** 985 (2002).

[37] L.-S. Huang and C.-M. Ho, "Small-scale transition in a plane mixing layer," J. Fluid Mech. **210**, 475 (1990).

[38] A. K. M. F. Hussain and K. B. M. Q. Zaman, "An experimental study of organized motions in the turbulent plane mixing layer," J. Fluid Mech. **159**, 85 (1985).

[39] A. K. M. F. Hussain, "Coherent structures and turbulence," J. Fluid Mech. **173**, 303 (1986).

[40] K. Kato, T. Wakimoto, and N. Nishioka, " The influence of pressure gradient-wall normal velocity correlation on turbulent Prandtl number," Trans. Japan Soc. Mech. Engng. B **78** 1784 (2012) (in Japanese).

[41] K. Kato, A. Sakai, R. Fujii, T. Wakimoto, and G. Kawahara, " Influence of spanwise vorticity on dissimilarity between turbulent momentum and heat transfer," Trans. Japan Soc. Mech. Engng. B **79** 2019 (2013) (in Japanese).

[42] D. Divoky and E. Mayer, "Correlation of intermittency with preferential transport of heat and chemical species in turbulent shear flows," AIAA Journal **4**, 1995 (1966).

[43] L. Fulachier, R. Antonia, Heat and mass transport. In Turbulence, Springer, 231 (1975).

[44] A. Chambers, R. Antonia, and L. Fulachier, "Turbulent prandtl number and spectral characteristics of a turbulent mixing layer," Int. J. Heat Mass Transf. **28**, 1461 (1985).

[45] J. C. Vassilicos, "Dissipation in turbulent flows," Annu. Rev. Fluid Mech. **47**, 95 (2015).

[46] H. Tennekes and J. L. Lumley, A First Course in Turbulence (MIT, Cambridge, MA, 1972).

[47] J. Mathieu, J. Scott, An introduction to turbulent flow, Cambridge University Press (2000).

[48] P. Sagaut, C. Cambon, Homogeneous turbulence dynamics, vol. 10, Springer (2000).

[49] S. Goto and J. C. Vassilicos, "Energy dissipation and flux laws for unsteady turbulence," Phys. Lett. A **379**, 1144 (2015).

[50] S. Goto and J. C. Vassilicos, "Local equilibrium hypothesis and taylors dissipation law," Fluid Dyn. Res. **48**, 021402 (2016).

[51] J. Kim and P. Moin, "Application of a fractional-step method to incompressible Navier-Stokes equations," J. Comput. Phys. **59**, 308 (1985).

[52] H. Suzuki, K. Nagata, Y. Sakai, T. Hayase, Y. Hasegawa, and T. Ushijima, "An attempt to improve accuracy of higher-order statistics and spectra in direct numerical simulation of incompressible wall turbulence by using the compact schemes for viscous terms," Int. J. Numer. Methods Fluids **73**, 509 (2013).

[53] T. Watanabe, Y. Sakai, K. Nagata, Y. Ito, and T. Hayase, "Turbulent mixing of passive scalar near turbulent and non-turbulent interface in mixing layers," Phys. Fluids **27**, 085109 (2015).

[54] P. R. Spalart, R. D. Moser, and M. M. Rogers, "Spectral methods for the Navier-Stokes equations with one infinite and two periodic directions," J. Comput. Phys. **96**, 297 (1991).

[55] T. Kajishima, K. Taira, Computational fluid dynamics: Incompressible turbulent flows, in Springer (2017).

[56] Y. Kametani, M. Kawagoe, and K. Fukagata, "Direct numerical simulation of a turbulent mixing layer with a transversely oscillated inflow," J. Fluid Sci. and Tech. **10**, 14–00292 (2015).

[57] H. Le and P. Moin, "An improvement of fractional step methods for the incompressible Navier-Stokes equations," J. Comp. Phys. **92** 369 (1991).

[58] Y. Zhou, "Direct numerical simulations on grid-generated turbulence," PhD thesis, Nagoya University (2015).

[59] H. A. Van Der Vorst, "Bi-CGSTAB: A fast and smoothly converging variant of Bi-CG for the solution of nonsymmetric linear systems," SIAM J. Sci. and Stat. Comput. **13(2)** 631 (1992).

[60] L. P. Bernal and A. Roshko, "Streamwise vortex structure in plane mixing layers," J. Fluid Mech. **170**, 499–525 (1986).

[61] M. M. Koochesfahani and P. E. Dimotakis, "Mixing and chemical reactions in a turbulent liquid mixing layer," J. Fluid Mech. **170**, 83 (1986).

[62] R. D. Moser and M. M. Rogers, "Mixing transition and the cascade to small scales in a plane mixing layer," Phys. Fluids **3**, 1128 (1991).

[63] S. M. de Bruyn Kops and M. Mortensen, "Conditional mixing statistics in a self-similar scalar mixing layer," Phys. Fluids **17**, 095107 (2005).

[64] W. A. Mcmullan and J. S. Garrett, "Initial condition effects on large scale structure in numerical simulations of plane mixing layers," Phys. Fluids **28**, 015111 (2016).

[65] A. Attili and F. Bisetti, "Structure function scaling in a $Re_\lambda = 250$ turbulent mixing layer," J. Phys.: Conf. Ser. **318**, 042001 (2011).

[66] A. Attili and F. Bisetti, "Fluctuations of a passive scalar in a turbulent mixing layer," Phys. Rev. E **88**, 033013 (2013).

[67] A. Attili and F. Bisetti, "Statistics of the turbulent/non-turbulent interface in a spatially developing mixing layer," J. Turb. **15**, 555 (2014).

[68] D. Fiscaletti, G. E. Elsinga, A. Attili, F. Bisetti, and O. R. H. Buxton, "Scale dependence of the alignment between strain rate and rotation in turbulent shear flow," Phys. Rev. Fluids **1**, 064405 (2016).

[69] Y. Morinishi, T. S. Lund, O. V. Vasilyev, and P. Moin, "Fully conservative higher order finite difference schemes for incompressible flow," J. Comput. Phys. **143**, 90 (1998).

[70] L. Biancofire, "Crossover between two- and three-dimensional turbulence in spatial mixing layers," J. Fluid Mech. **745**, 164 (2014).

[71] H. Liepmann and J. Laufer, "Investigations of free turbulent mixing," National Advisory Committee for Aeronautics Technical Note No. 1257, (1947).

[72] J. B. Miles and J.-S. Shih, "Similarity parameter for two-stream turbulent jet-mixing region," AIAA J. **6**, 1429 (1968).

[73] R. D. Mills, "Numerical and experimental investigations of the shear layer between two parallel streams," J. Fluid Mech. **33**, 591 (1968).

[74] N. K. Pui, "The plane mixing region between parallel stream," MSc thesis. University of British Columbia (1969).

[75] B. Spencer and B. Jones, Statistical investigation of pressure and velocity fields in the turbulent two-stream mixing layer (American Institute of Aeronautics and Astronautics, 1971).

[76] M. Sunyach, "Contribution a 1' étude des frontirés d'écoulements turbulents libres," Ph.D. thesis, L'Université Claude Bernard de Lyon (1971).

[77] A. J. Yule, Two-dimensional self-preserving turbulent mixing layers at different free stream velocity ratios (HM Stationery Office, 1972).

[78] N. Li, E. Balaras, and J. M. Wallace, "Passive scalar transport in a turbulent mixing layer," Flow, Turbul. Combust. **85**, 1 (2010).

[79] R. B. Loucks and J. M. Wallace, "Velocity and velocity gradient based properties of a turbulent plane mixing layer," J. Fluid Mech. **699**, 280 (2012).

[80] S. Komori and K. Nagata, "Effects of molecular diffusivities on countergradient scalar and momentum transfer in strongly stable stratification," J. Fluid Mech. **326**, 205 (1996).

[81] I. Daubechies, Ten Lectures on Wavelets (Society for Industrial and Applied Mathematics, 1992).

[82] C. B. da Silva, J. C. R. Hunt, I. Eames, and J. Westerweel, "Interfacial layers between regions of different turbulence intensity," Annu. Rev. Fluid Mech. **46**, 567 (2014).

[83] R. R. Taveira, J. S. Diogo, D. C. Lopes, and C. B. da Silva, "Lagrangian statistics across the turbulent-nonturbulent interface in a turbulent plane jet," Phys. Rev. E **88**, 043001 (2013).

[84] T. Watanabe, Y. Sakai, K. Nagata, Y. Ito, and T. Hayase, "Enstrophy and passive scalar transport near the turbulent/non-turbulent interface in a turbulent planar jet flow," Phys. Fluids **26**, 105103 (2014).

[85] R. R. Taveira and C. B. da Silva, "Characteristics of the viscous superlayer in shear free turbulence and in planar turbulent jets," Phys. Fluids **26**, 021702 (2014).

[86] J. Westerweel, C. Fukushima, J. M. Pedersen, and J. C. R. Hunt, "Momentum and scalar transport at the turbulent/non-turbulent interface of a jet," J. Fluid Mech. **631**, 199 (2009).

[87] M. M. Rogers, N. N. Mansour, and W. C. Reynolds, "An algebraic model for the turbulent flux of a passive scalar," J. Fluid Mech. **203**, 77 (1989).

[88] K. Abe and K. Suga, "Towards the development of a reynolds-averaged algebraic turbulent scalar-flux model," Int. J Heat. Fluid Flow **22**, 19 (2001).

[89] B. J. Daly and F. H. Harlow, "Transport equations in turbulence," The Phys Fluids **13**, 2634 (1970).

[90] J. Kim and P. Moin, "Transport of passive scalars in a turbulent channel flow. In: Proceedings of the 6th international symposium on turbulent shear flows, Toulouse," France, 7–9 September 1987. Springer, Berlin (1987).

[91] B. Launder, "Heat and mass transport. in Turbulence," Springer, 231 (1975).

[92] L. Fulachier and R. Antonia, "Spectral analogy between temperature and velocity fluctuations in several turbulent flows," Int. J. Heat Mass Transf. **27**, 987 (1984).

[93] Y. Ito, K Miura, Y. Sakai, and K. Iwano, "Enhancement and suppression of mixing and diffusion in an axisymmetric jet by half delta-wing tabs," Int. J. Heat Mass Transf. **118**, 1218 (2018).

[94] S. A. Elaskar, E. A. Pilotta and G. A. Torres, "Velocity and temperature natural dissimilarity in a turbulent channel flow," Mecanica Computacional **26**, 3644 (2007).

[95] H. Pasinato "Velocity and temperature dissimilarity in fully developed turbulent channel and plane couette flows," Int. J. Heat Fluid Flow **32**,11 (2011).

[96] Y. Hasegawa and N. Kasagi, "Dissimilar control of momentum and heat transfer in a fully developed turbulent channel flow," J. Fluid Mech. **683**, 57 (2011).

[97] K. Matsubara, T. Miura, H. Ohta, "Transport dissimilarity in turbulent channel flow disturbed by rib protrusion with aspect ratio up to 64," Int. J. Heat Mass Transf. **86**, 113 (2015).

[98] L. Fulachier and R. Dumas, "Spectral analogy between temperature and velocity fluctuations in a turbulent boundary layer," J. Fluid Mech. **77**, 257 (1976).

[99] R. Antonia, L. Krishnamoorthy and L. Fulachier, "Correlation between the longitudinal velocity fluctuation and temperature fluctuation in the near-wall region of a turbulent boundary layer," Int. J. Heat Mass Transf. **31**, 723 (1988).

[100] K. Inaoka, J. Yamamoto and K. Suzuki, "Dissimilarity between heat transfer and momentum transfer in a disturbed turbulent boundary layer with insertion of a rod-modeling and numerical simulation," Int. J. Heat Fluid Flow **20**, 290 (1999).

[101] H. Kong, H. Choi and J. S. Lee, "Dissimilarity between the velocity and temperature fields in a perturbed turbulent thermal boundary layer," Phys. Fluids **13**, 1466 (2001).

[102] H. Pasinato, "Dissimilarity of turbulent fluxes of momentum and heat in perturbed turbulent flows," J Heat Transf **135**, 051701 (2013).

[103] H. Gu, M. Yao, P. Zhao, X. Li and M. Liu, "Numerical simulation of manipulated flow and heat transfer over surfacemounted rib," Int. J. Therm. Sci. **129**, 124 (2018).

[104] H. F. Fiedler, "Transport of heat across a plane turbulent mixing layer," Adv. Geophysics. **18**, 93 (1975).

[105] H. F. Fiedler, "On turbulence structure and mixing mechanism in free turbulent shear flows. In: Turbulent Mixing in Nonreactive and Reactive Flows." (Springer, 1975) 381 (1975).

[106] K. R. Sreenivasan, "On the scaling of the turbulence energy dissipation rate," Phys. Fluids **27**, 1048 (1984).

[107] K. R. Sreenivasan, "On the universality of the Kolmogorov constant," Phys. Fluids **7**, 2778 (1995).

[108] K. R. Sreenivasan, "An update on the energy dissipation rate in isotropic turbulence," Phys. Fluids **10**, 528 (1998).

[109] B. Pearson, P.-. Krogstad,W. Van De Water, "Measurements of the turbulent energy dissipation rate", Phys. Fluids **14** 1288 (2002).

[110] P. Burattini, P. Lavoie, and R. A. Antonia, "On the normalized turbulent energy dissipation rate," Phys. Fluids **17**, 098103 (2005).

[111] T.-H. Shih, W. W. Liou, A. Shabbir, Z. Yang, and J. Zhu, "A new $k-\epsilon$ eddy viscosity model for high reynolds number turbulent flows," Computers and Fluids **24** 227 (1995).

[112] S. B. Pope, Turbulent flows, Cambridge University Press (2001).

[113] H. K. Versteeg, W. Malalasekera, An Introduction to Computational Fluid Dynamics: The Finite Volume Method, Pearson Education, 2007.

[114] M. Langhi, T. Hosoda, and S. Dey, "Analytical solution of $k-\epsilon$ model for nonuniform flows," J. Hydraulic Engineering **144** 044018033 (2018).

[115] D. Hurst and J. C. Vassilicos, "Scalings and decay of fractal-generated turbulence," Phys. Fluids 19, 035103 (2007).

[116] R. E. Seoud and J. C. Vassilicos, "Dissipation and decay of fractal-generated turbulence," Phys. Fluids **19**, 105108 (2007).

[117] P. C. Valente and J. C. Vassilicos, "Universal dissipation scaling for non-equilibrium turbulence," Phys. Rev. Lett. **108**, 214503 (2012).

[118] J. C. Isaza, R. Salazar, and Z. Warhaft, "On grid-generated turbulence in the near- and far field regions," J. Fluid Mech. **753**, 402 (2014).

[119] P. C. Valente and J. C. Vassilicos, "The non-equilibrium region of grid-generated decaying turbulence," J. Fluid Mech. **744**, 537 (2014).

[120] N. Mazellier and J. C. Vassilicos, "Turbulence without Richardson-Kolmogorov cascade," Phys. Fluids **22**, 075101 (2010).

[121] P. C. Valente and J. C. Vassilicos, "The decay of turbulence generated by a class of multiscale grids," J. Fluid Mech. **687**, 300 (2011).

[122] R. Gomes-Fernandes, B. Ganapathisubramani, and J. C. Vassilicos, "Particle image velocimetry study of fractal-generated turbulence," J. Fluid Mech. **711**, 306 (2012).

[123] R. Gomes-Fernandes, B. Ganapathisubramani, and J. C. Vassilicos, "The energy cascade in near-field non-homogeneous non-isotropic turbulence," J. Fluid Mech. **771**, 676 (2015).

[124] K. Nagata, H. Suzuki, Y. Sakai, T. Hayase, and T. Kubo, "Direct numerical simulation of turbulence characteristics generated by fractal grids," Int. Rev. Phys. **2**(6), 400 (2008).

[125] P. C. Valente and J. C. Vassilicos, "Dependence of decaying homogeneous isotropic turbulence on inflow conditions," Phys. Lett. A **376**, 510 (2012).

[126] G. Melina, P. J. K. Bruce, and J. C. Vassilicos, "Vortex shedding effects in grid-generated turbulence," Phys. Rev. Fluids **1**, 044402 (2016).

[127] S. Discetti, I. B. Ziskin, T. Astarita, R. J. Adrian, and K. P. Prestridge, "PIV measurements of anisotropy and inhomogeneity in decaying fractal generated turbulence," Fluid Dyn. Res. **45**, 061401 (2013).

[128] P. C. Valente and J. C. Vassilicos, "The energy cascade in gridgenerated non-equilibrium decaying turbulence," Phys. Fluids **27**, 045103 (2015).

[129] R. J. Hearst and P. Lavoie, "Scale-by-scale energy budget in fractal element grid-generated turbulence," J. Turbul. **15**, 540 (2014).

[130] R. J. Hearst and P. Lavoie, "Decay of turbulence generated by a squarefractal-element grid," J. Fluid Mech. **741**, 567 (2014).

[131] R. J. Hearst and P. Lavoie, "Velocity derivative skewness in fractal-generated, non-equilibrium grid turbulence," Phys. Fluids **27**, 071701 (2015).

[132] K. Nagata, Y. Sakai, T. Inaba, H. Suzuki, O. Terashima, and H. Suzuki, "Turbulence structure and turbulence kinetic energy transport in multiscale/fractal-generated turbulence," Phys. Fluids **25**, 065102 (2013).

[133] R. J. Hearst and P. Lavoie, "Effects of multi-scale and regular grid geometries on decaying turbulence," J. Fluid Mech. **803**, 528 (2016).

[134] K. Nagata, T. Saiki, Y. Sakai, Y. Ito, and K. Iwano, "Effects of grid geometry on non-equilibrium dissipation in grid turbulence," Phys. Fluids **29**, 015102 (2017).

[135] S. Laizet and J. C. Vassilicos, "Multiscale generation of turbulence," J. Multiscale Modell. **1**, 177 (2009).

[136] H. Suzuki, K. Nagata, Y. Sakai, and T. Hayase, "Direct numerical simulation of turbulent mixing in regular and fractal grid turbulence," Phys. Scr. **T142**, 014065 (2010).

[137] S. Laizet, E. Lamballais, and J. C. Vassilicos, "A numerical strategy to combine high-order schemes, complex geometry and parallel computing for high resolution DNS of fractal generated turbulence," Comput. Fluids **39**, 471 (2010).

[138] S. Laizet and J. C. Vassilicos, "DNS of fractal-generated turbulence," Flow, Turbul. Combust. **87**, 673 (2011).

[139] S. Laizet, J. C. Vassilicos, and C. Cambon, Interscale energy transfer in decaying turbulence and vorticity-strain-rate dynamics in grid-generated turbulence," Fluid Dyn. Res. **45**, 061408 (2013).

[140] Y. Zhou, K. Nagata, Y. Sakai, H. Suzuki, Y. Ito, O. Terashima, and T. Hayase, "Relevance of turbulence behind the single square grid to turbulence generated by regular- and multiscale-grids," Phys. Fluids **26**, 075105 (2014).

[141] J. Nedić, and S. Tavoularis, "Energy dissipation scaling in uniformly sheared turbulence," Phys. Rev. E **93**, 033115 (2016).

[142] J. Nedić, S. Tavoularis, and I. Marusic, "Dissipation scaling in constant-pressure turbulent boundary layers," Phys. Rev. Fluids **2**, 032601 (2017).

[143] Md. Kamruzzaman, L. Djenidi, and R. A. Antonia, "Behaviour of the energy dissipation coefficient in a rough wall turbulent boundary layer," Exp. Fluids **59**, 9pages (2018).

[144] J. Nedić, J. C. Vassilicos, and B. Ganapathisubramani, "Axisymmetric Turbulent Wakes with New Non-equilibrium Similarity Scalings," Phys. Rev. Lett. **111**, 144503 (2013).

[145] T. Dairay, M. Obligado, and J. C. Vassilicos, "Non-equilibrium scaling laws in axisymmetric turbulent wakes, J. Fluid Mech. **781**, 166 (2015).

[146] M. Obligado, T. Dairay, and J. C. Vassilicos, "Nonequilibrium scalings of turbulent wakes," Phys. Rev. Fluids **1**, 044409 (2016).

[147] T. Dairay and J. C. Vassilicos, "Direct numerical simulation of a turbulent wake: the non-equilibrium dissipation law," Intl J. Heat Fluid Flow **62**, 68 (2016).

[148] P. O. A. L. Davies and A. J. Yule, "Coherent structures in turbulence," J. Fluid Mech. **69**, 513 (1975).

[149] W. K. George and H. J. Hussein, "Locally axisymmetric turbulence," J. Fluid Mech. **233** 1 (1991).

[150] S. Laizet, J. Nedic, J. C. Vassilicos, The spatial origin of -5/3 spectra in grid-generated turbulence, Phys. Fluids **27** 065115 (2015).

[151] A. A. Townsend, The Structure of Turbulent Shear Flow, Cambridge University Press, (1980).

[152] G. K. Batchelor, The Theory of Homogeneous Turbulence, Cambridge University Press (1953).

[153] U. Frisch, Turbulence: The Legacy of A.N. Kolmogorov, Cambridge University Press, (1995).

[154] M. Lesieur, Turbulence in Fluids: Stochastic and Numerical Modelling, Nijhoff Boston, MA (1987).

[155] J. Delville, "Characterization of the organization in shear layers via the proper orthogonal decomposition," Appl. Sci. Res. **53**, 263 (1994).

[156] J. Delville, L. Ukeiley, L. Cordier, J. P. Bonnet, and M. Glauser, "Examination of large-scale structures in a turbulent plane mixing layer. Part 1. Proper orthogonal decomposition," J. Fluid Mech. **391**, 91 (1999).

[157] J. Lewalle, J. Delville, and J.-P. Bonnet, "Decomposition of mixing layer turbulence into coherent structures and background fluctuations, Flow," Turbul. Combust. **64**, 301 (2000).

[158] P Druault, J Delville and JP Bonnet, "Proper Orthogonal Decomposition of the mixing layer flow into coherent structures and turbulent Gaussian fluctuations," Comptes Rendus Mecanique **333**, 824 (2005).